EXPERIMENTAL PERFORMANCE OF AN OPEN ENDS SQUEEZE FILM DAMPER AND A SEALED ENDS SQUEEZE FILM DAMPER

A Dissertation

by

SUNG HWA JEUNG

Submitted to the Office of Graduate Professional Studies of
Texas A&M University
in partial fulfillment of the requirements for the degree of

DOCTOR OF PHILOSOPHY

Chair of Committee,	Luis San Andrés
Committee Members,	Won-Jong Kim
	Hamn-Ching Chen
	Yong-Joe Kim
Head of Department,	Andreas Polycarpou

May 2017

Major Subject: Mechanical Engineering

Copyright 2017 Sung Hwa Jeung

ABSTRACT

High performance turbomachinery often experiences severe dynamic loads that produce large amplitude rotor motions. Well-engineered squeeze film dampers (SFDs) provide adequate damping to ameliorate rotor vibrations and to ensure system reliability. Open ends SFDs are prone to air ingestion during large amplitude rotor whirl motions and high excitation frequencies, all the while demanding of a significant flowrate, an undesirable operating feature. Piston ring (PR) end seals are commonly installed in SFDs in aircraft engines to amplify the available damping while reducing the demand of oil flowrate and also to avoid air ingestion.

This dissertation investigates experimentally the dynamic forced performance of a SFD with a short land length (L/D=0.2), nominal clearance 0.254 mm and lubricant supplied via three orifice feed holes (ϕ=2.5 mm). There are two configurations, one has its ends open to ambient while the other has sealed ends with PRs. The dynamic load tests are of three types (single frequency, sine-sweep frequency dynamic loads and impact loads).

Single frequency dynamic load tests reveal that the piston ring end seals effectively reduce leakage through the ends of the film land; thus the sealed SFD provides 11-13 times more damping coefficient and eleven times more added mass coefficients than those provided by an open ends SFD configuration. Further tests of two PR sealed ends SFDs (one with a seal flow conductance C_{ave-S1} = 0.56 LPM/bar, and the other with C_{ave-S2} = 0.89 LPM/bar) operated at a supply pressure $P_{in\text{-}1}$~0.69 barg, show that small

differences on their damping and added mass coefficients are within the measurement uncertainty range. The second pair of piston rings ($C_{ave-S2} > C_{ave-S1}$) has a larger slit gap than the first pair, hence providing a lesser flow resistance. The effect of lubricant supply pressure on the sealed ends SFD force coefficients is also quantified experimentally by increasing the lubricant supply pressure by a factor of four ($P_{in\text{-}1}$~0.69 barg→$P_{in\text{-}2}$~2.76 barg). For the sealed ends SFD with C_{ave-S1} and $P_{in\text{-}2}$~2.76 barg, both the damping and added mass coefficients show a ~20% increase compared to those coefficients from the damper supplied with a low oil feed pressure ($P_{in\text{-}1}$~0.69 barg).

Further experiments with the sine-sweep frequency dynamic load tests aim to validate the SFD force coefficients identified from a single-frequency dynamic load. The estimated SFD damping and inertia force coefficients from a sine-sweep frequency load tests with a low time rate of change in sine-sweep excitation frequency α=6.5 Hz/s agree with the coefficients obtained from a single-frequency dynamic load over the same test conditions while substantially reducing the time of data collection.

Furthermore, single impact load tests are performed to quantify their effect on the response of an elastically supported open ends SFD and sealed ends SFD. Test system transient responses due to a single impact show the peak amplitude of motion (Z_{MAX}) is proportional to the magnitude of applied load (F_{MAX}). The identified system damping ratio (ζ) is proportional to the peak dynamic displacement as a linear system shows.

The dissertation discloses the full detail of the test dampers geometry and the experimental results which will provide a design reference to the practitioners.

DEDICATION

To my family and friends; they make my life plentiful.

ACKNOWLEDGEMENTS

I extend my deepest thanks to Dr. Luis San Andrés for his guidance and support. I have not only gained knowledge from him, but also an attitude of diligence and hard work toward ones professional career that I will carry throughout my career.

Thanks to Dr. Yong-Joe Kim, Dr. Hamn-Ching Chen, Dr. Won-Jong Kim and Dr. Seok-Chang Ryu members of my advisory committee, for their time and interest.

My sincere thanks to Sean Den, Yong Zheng, Bonjin Koo and Wonbae Jung for their deep friendship, inspiration, and for proofreading my technical reports throughout my graduate studies. Without them, I could not have gone this far.

I also acknowledge the friendship and support of my lab mates, Xueliang Lu, Tingcheng Wu, Qing Liu, Michael Rohmer, Jonathan Baptista, Jerry Haripin, Scott Tran, Feng Yu, Youfeng Zhang, Yingkun Li, Lili Gu, Ziam Ghaznavi, Mathew Hilton, Scott Wilkinson, Leo Wood, and many others.

Special thanks to Turbomachinery Research Consortium (TRC) and Pratt & Whitney UTC for their interest and financial support.

CONTRIBUTORS AND FUNDING SOURCES

Contributors

Part 1, Faculty committee recognition

This work was supervised by a dissertation committee consisting of Dr. Luis San Andrés, Dr. Yong-Joe Kim and Dr. Won-Jong Kim of the Department of Mechanical Engineering and Dr. Hamn-Ching Chen of the Department of Civil Engineering.

Part 2, student/collaborator contributions

Mr. Sean Den proofread all the Chapters in the dissertation. Mr. Bonjin Koo proofread the Appendices in the dissertation.

All other work conducted for the dissertation was completed by the student independently.

Funding Sources

This material is based upon work supported by the Turbomachinery Research Consortium and Pratt & Whitney, UTC.

TABLE OF CONTENTS

Page

LIST OF FIGURES

Page

LIST OF TABLES

Page

NOMENCLATURE

$a_{\alpha(t),\ (\alpha=X,Y)}$	Acceleration of bearing cartridge [m/s^2]
c	Nominal radial clearance [μm]
$C_{ave\text{-}s}$	End seal conductance [m^3/(s.Pa)]
C_o	Flow conductance of one orifice, $1/R_o$ [m^3/(s.Pa)]
$C_{\alpha\beta,\ (\alpha,\beta=X,Y)}$	SFD damping coefficients [N·s/m]
C_S	Dry structure damping coefficient [N·s/m]
$\overline{C}_{Seal}$	End seal conductance per unit circumference length $\frac{C_{ave-S1}}{\pi D}$ [m^2/(s.Pa)]
D	Journal diameter [m]
e_s	Static eccentricity (along 45^o) [m]
F_i	Fluid inertia force [N]
F_X, F_Y	Components of applied dynamic load [N]
F_r	Reaction fluid film force, $F_r = F_i + F_v$ [N]
F_v	Fluid viscous force [N]
F_s	Static load [N]
f	Excitation frequency [Hz]
f_n	Test system natural frequency [Hz]
f_{start} , f_{end}	Start and end frequencies for sine-sweep frequency range [Hz]
$H_{\alpha\beta,\ (\alpha,\beta=X,Y)}$	Measured system complex stiffness [N/m]

h	Lubricant film thickness [m]
i	$\sqrt{-1}$. Imaginary unit
$K_{\alpha\beta,\ (\alpha,\beta=X,Y)}$	SFD stiffness coefficients [N/m]
K_S	Structure support stiffness [N/m]
L	Film land length [m]
$M_{\alpha\beta,\ (\alpha,\beta=X,Y)}$	SFD added mass coefficients [kg]
M_S	Dry structure added remnant mass coefficient [kg]
M_{BC}	Bearing cartridge mass [kg]
n	Number of impacts [-]
P	Dynamic pressure in film land [Pa]
P_{in}	Static oil pressure at oil supply line (upstream of feedholes) [Pa]
P_o	Pressure at feedhole [Pa]
Q_{in}	Lubricant flow rate [m^3/s]
Q_T, Q_B	Lubricant flow rate of top and bottom film lands [m^3/s]
Q_{th}	Theoretical flow rate across film land [m^3/s]
r	Orbit amplitude [m]
R	Journal radius, R= ½ D [m]
R_o	Orifice flow resistance, $1/C_o$ [$Pa.s/m^3$]
R_{TL}, R_{BL}	Flow resistance of top and bottom film lands [$Pa.s/m^3$]
R_{TS}, R_{BS}	Flow resistance of top and bottom piston rings [$Pa.s/m^3$]
t	Time [s]
t_{IMP}	Typical duration of impact [s]

T_r	Force transmissibility ratio [-]
T^*	Elapsed time of sine-sweep frequency dynamic load excitation [s]
$\Delta f/\Delta t$	Sweep frequency ramp rate, $(f_{end}-f_{start})/T^*$ [Hz/s]
$X,Y, \bar{X},\bar{Y}$	Coordinate systems
$x_{(t)}, y_{(t)}$	Relative displacement of BC respect to the journal along X and Y direction [m]
Z_s	$e_s \cos(\ ¼\pi\ )$. Static displacement along X,Y [m]
$Z_{X,Y}$	Bearing cartridge displacements along X and Y [m]
Z^{dyn}	$(Z-Z_s)$. Dynamic displacement of BC along impact load direction, [m]
β	Slope of peak dynamic displacement vs. peak load, $\left[\bar{Z}^{dyn}_{MAX}/c\right]/\left[\bar{F}_{MAX}/(L\,D)\right]$ [1/Pa]
δ	Logarithmic decrement, $2\pi\xi/\sqrt{1-\xi^2}$ [-]
$\rho,\ \mu$	Oil density [kg/m^3] and viscosity [Pa·s]
Θ	Circumferential angular coordinate [rad]
ω	Excitation frequency (ω=2πf) [rad/s]
ξ	Damping ratio [-]

Vectors and matrices

$\bar{\mathbf{a}}_{(\omega)}$	Vector of accelerations $\{a_{X(\omega)}, a_{Y(\omega)}\}^T$ in the frequency domain [m/s^2]

$\mathbf{C}$	Matrix of damping coefficients [N·s/m]
$\mathbf{K}$	Matrix of stiffness coefficients [N/m]
$\overline{\mathbf{F}}_{(\omega)}$	Vector of dynamic loads $\{F_{X(\omega)}, F_{Y(\omega)}\}^{T}$ in the frequency domain [N]
$\overline{\mathbf{H}}_{(\omega)}$	$\mathbf{K} - \omega^2\mathbf{M} + i\omega\mathbf{C}$ Matrix of dynamic stiffness coefficients in the frequency domain [N/m]
$\mathbf{M}$	Matrix of added mass coefficients [kg]
$\bar{\mathbf{z}}_{(\omega)}$	Vector of relative displacements $\{x_{(\omega)}, y_{(\omega)}\}^{T}$ in the frequency domain [m]

Subscripts

BC	Bearing cartridge
CCW	Counter-clockwise
CW	Clockwise
L	Lubricated system
S	Structure
s	Static

Acronyms

DAQ	Data acquisition
DFT	Discrete Fourier Transform
FRF	Frequency Response Function

SFD	Squeeze Film Damper

1. INTRODUCTION

With higher power density and improved efficiency, modern rotating machinery operate at increasingly higher rotational speeds. As a result, bearing supports experience large dynamic loads and must withstand significant large amplitude motions. A Squeeze Film Damper (SFD) aids to reduce rotor synchronous vibration response as the system crosses its critical speeds. Thus, aircraft engines and high-speed compressors implement SFDs to dissipate mechanical energy produced by rotor motion; and along with a flexible support, lead to lower transmitted forces [1,2].

Figure 1 depicts schematic views of an open ends SFD and a sealed ends SFD, both in series with a ball bearing supported rotor. The annular gap between the two cylinders (housing and outer race of ball bearing) contains the film of lubricant that is squeezed during operation. An anti-rotation pin or a squirrel cage prevents the outer race of ball bearing from rotating. Unlike a journal bearing, SFDs do not rotate, but whirl (or precess) in response to rotor vibrations and squeeze the film land to generate a hydrodynamic pressure [1].

Figure 2 depicts the schematic of the generation of viscous hydrodynamic pressure in (a) a journal bearing whose center is displaced to static eccentricity e_s and spinning with speed Ω, and (b) a SFD with its journal performing circular centered orbits of radius r and whirl frequency ω [3]. In a journal bearing, the film peak pressure locates upstream of the minimum film thickness, whereas in a SFD the film peak dynamic pressure occurs 90^o away from the minimum film thickness. Note that the view of viscous hydrodynamic

pressure for SFD in Figure 2(b) does not include the effect of fluid inertia. A SFD with its journal whirling with frequency ω and amplitude r produces approximately twice as large reaction force as the force in a hydrodynamic journal bearing with its journal spinning with angular speed $\Omega = \omega$ at static eccentricity $e = r$ [3].

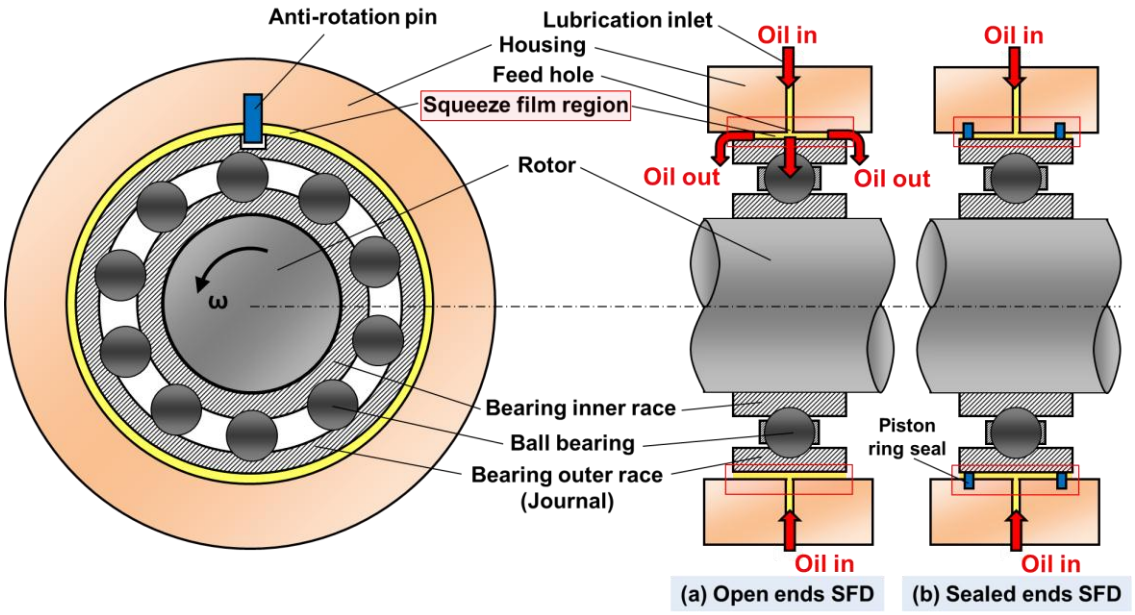

Figure 1. Schematic views of hole-fed SFDs with: (a) open ends and (b) sealed ends, adapted from [1].

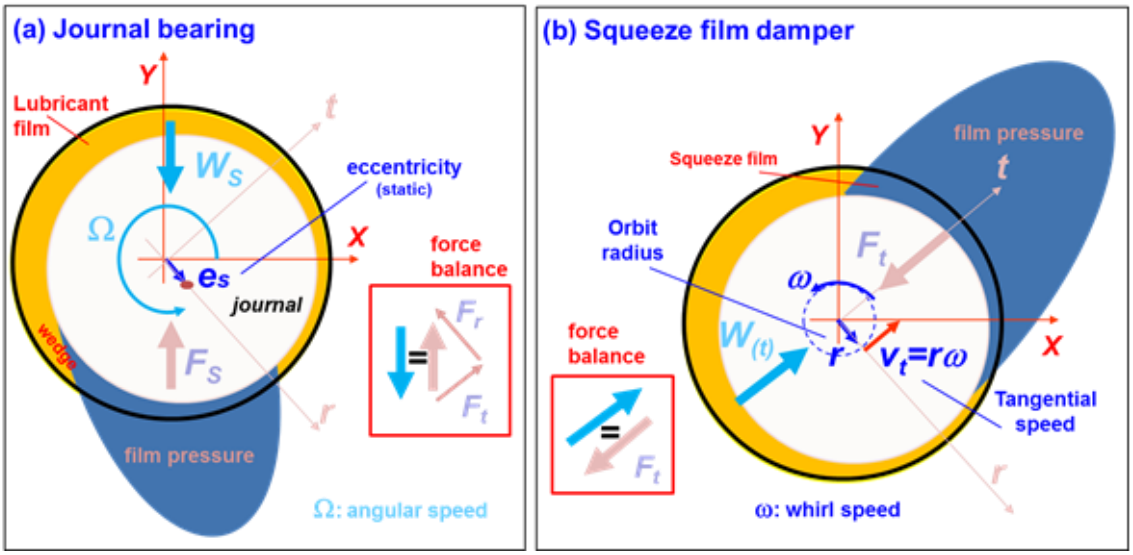

Figure 2. Schematic views of viscous hydrodynamic pressure fields in: (a) a journal bearing with static eccentricity e_s and spinning with speed Ω and (b) SFD with circular centered orbits of radius *r* and whirl frequency *ω*. Instantaneous balance of forces shown. Film or gap exaggerated [3].

The forced performance of SFDs depends largely upon the damper geometry, lubricant viscosity, supply and operating conditions, and sealing devices (piston ring and O-ring) among other factors. There are unlimited feasible geometric configurations of SFDs, thus researchers have poured countless efforts to determine the characteristic forced performance of various types of SFDs [4].

Presently the need of a simpler SFD design to save space and weight in aircraft engines has led to research in ultra-short length SFDs; that is, a damper with length to diameter ratio (*L/D*) 0.2 or less [3,5,6]. Compared to SFDs with a circumferential feeding groove arrangement, dampers with orifice feed holes impinging directly into the film land simplify SFD design and save space and weight.

Open ends SFDs are prone to air ingestion when undergoing large amplitude journal motions during dynamic operation [3]. Air entrainment, which reduces the generation of squeeze film pressure and thus degrades the damping force, can be substantially reduced by installing sealing devices such as piston ring seals or O-rings at the end of the film lands (see Figure 1(b)). Note that O-rings have a temperature limit of 130ºC and fatigue easily at high temperature. Installation of piston ring end seals amplifies the damping capability of SFD while lowering the required lubricant flow rate [4].

Jet engines inevitably experience arduous transient events due to maneuver loads and sudden shock loads such as during hard landings and takeoffs. During these transient events, the engine support structure is subject to large transmitted forces that could, over time, foster fatigue of the centralizing spring (squirrel cage). Adequate damping to ameliorate rotor vibrations is paramount to ensure system integrity and reliability. Certifying the reliable operation of turbomachinery calls for a detailed characterization of SFD forced performance under these stringent operating conditions.

The present work is a part of a multiple year research work on SFDs to advance the knowledge on SFD performance and operation and to integrate the knowledge (test data and analysis) into aircraft engine manufacturer engineering design practices. During this multi-year project (which is still ongoing), Dr. San Andrés, Principal Investigator, has overseen and guided the exhaustive experimental work and developed computational programs for prediction of SFD force response.

Figure 3 depicts the various damper configurations tested during the life of the project since its inception in 2008. The author become directly involved in the work of

dampers A-2, C, D, E and F by conducting dynamic load measurements for identification of force coefficients in a dedicated test rig. This research program also aimed to advance a SFD computational model for prediction of its dynamic load performance. The author's work with San Andrés is presented in Refs.[3,5,6,7,8,9,10,11]. In particular, a monumental paper [3] sums the experimental findings procured during the life of the project and provides answers to fundamental questions related to SFDs operation and performance.

The present work further extends prior research [3,5-10,11] on short length SFDs (L/D=0.2) configured with feed holes and present an experimental analysis of open and sealed ends SFDs, respectively. Comprehensive dynamic load tests on the SFD allow characterization of the forced performance of the SFD not only undergoing circular whirl motions, but also in response to various arduous transient event such as during hard landings and takeoffs. A full disclosure of the test dampers geometry and the experimental results will provide a design reference to the practitioners.

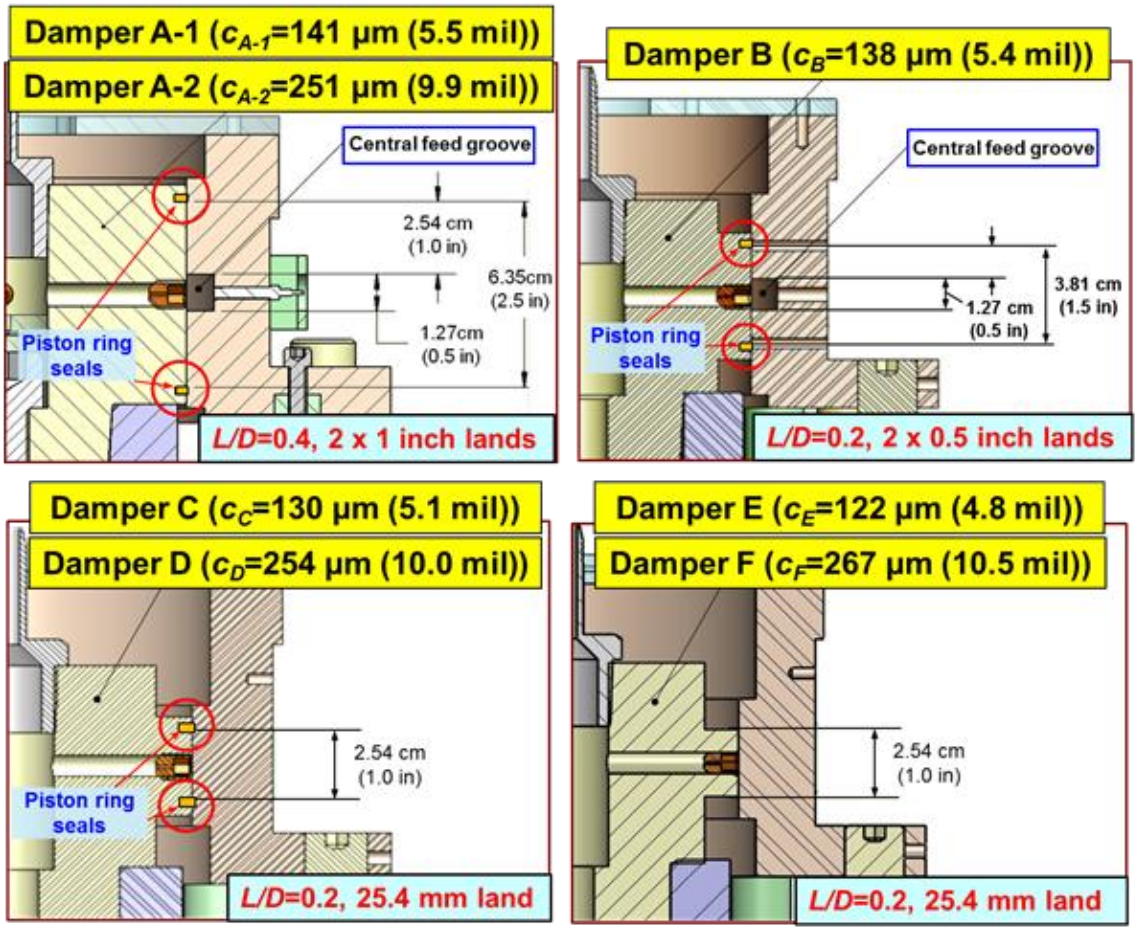

Figure 3. Cross-section views showing four test squeeze film damper configurations [3].
Top left: test damper A, L_A=25.4 mm, D=127 mm, c_{A-1}=141 µm and c_{A-2}=251 µm (nominal), 12.7 x 9.6 mm central feed groove and end grooves for piston rings (3.8 mm depth x 2.5 mm width).
Top right: test damper B, L_B=25.4 mm, D=127 mm, c_B=138 µm (nominal), 12.7 x 9.6 mm central feed groove and end grooves for piston rings (3.8 mm depth x 2.5 mm width).
Bottom left: test dampers C and D, L=25.4 mm, D=127 mm, c_C=130 µm and c_D=254 µm (nominal), film land end grooves, no central feed groove and end grooves for piston rings (3.8 mm depth x 2.5 mm width).
Bottom right: test dampers E and F, L=25.4 mm, D=127 mm, c_E=122 µm and c_F=267 µm, no central feed groove and no end grooves.
Note that feed holes are arranged 120° apart

2. LITERATURE REVIEW

The following literature review details the fluid inertia effect on SFDs, sealed end SFDs and SFDs undergoing transient dynamic loads. Afterwards, a discussion follows on bearing parameter identification methods and procedures.

2.1. Background

In 1889, Parsons introduced a prototypical SFD implemented into a steam turbine [12]. Much later in 1963, Cooper, an engineer at Rolls Royce, researched a bearing-support damping device (SFD) for an aircraft gas turbine to overcome rotordynamic instabilities [13]. By the 1970s, the use of SFDs in aero engines became a norm. Over the first five decades of SFD implementation after Cooper, SFDs are successfully incorporated into a wide range of applications such as in series with tilting pad bearings in compressors, semi-floating ring bearings in turbochargers, cutting tools and grinding machines, etc [1].

Zeidan et al. [4] detail the operation of SFDs for various damper designs in commercial turbomachinery. Care must be taken in selecting the proper amount of damping provided by a SFD; an overdamped support could lock the rotor-bearing system, whereas a too lightly damped support allows for too large amplitudes in rotor displacement.

In 2002, Refs. [14,15] review the characteristic of SFDs and relevant experimental data and physical model of SFDs over four decades.

More recently, San Andrés et al. [3] provide up-to-the-minute SFD experimental research conducted over seven years of continued work in his research laboratory. The vast amount of information gives definitive answers to fundamental questions on SFD performance, in particular about the fluid inertia effect from feed and discharge grooves, the effect of film clearance and land length on SFD forced performance, the effectiveness of sealed ends dampers, etc. Ref.[3] clearly distinguishes the SFD from a simple journal bearing whereas practitioners often overlook their operational differences.

2.2. Fluid Inertia Effects

During the early stages of SFD development, fluid inertia was largely ignored in conventional oil lubricated journal bearings due to the assumption of a slow fluid flow in the thin film. However, in 1964 Smith [16], and in 1975 Reinhart and Lund [17] numerically investigate the effect the fluid film inertial forces on the performance of a plain journal bearing by using a first-order perturbation solution with the modified Reynolds equation that includes a fluid inertia effect. The numerical results show that the influence of acceleration (inertia) coefficients can be significant on small, short length rotors. Disregarding the added mass coefficient may lead to a large discrepancy in the placement of critical speeds in a typical rotor bearing system.

Figure 4 depicts the generation of hydrodynamic pressure in a SFD undergoing (a) plunging motion and (b) circular whirl, respectively, including the generation of a pressure field (P_i) due to fluid inertia and resulting kinetics of a SFD [3]. Unlike plain journal bearings, SFDs have a relatively large nominal radial clearance (c) operating

with instantaneous large changes in speed. A large radial damper clearance leads to a large squeeze film Reynolds number, $\mathrm{Re}_S = \left(\rho\omega c^2\right)\Big/\mu \gg 1$ that induces a reaction force due to the fluid inertia effect (F_i) comparable to a purely viscous force (F_v) [3]. The reaction fluid film force F_r equals the sum of a fluid inertia component (F_i) to the viscous force (F_v).

San Andrés [18] extensively studied experimentally and analytically the influence of fluid inertia on the forced performance of single land SFDs. The findings reveal that operating with $\mathrm{Re}_S > 12$, the radial (inertia) force dominates over the tangential (damping) force.

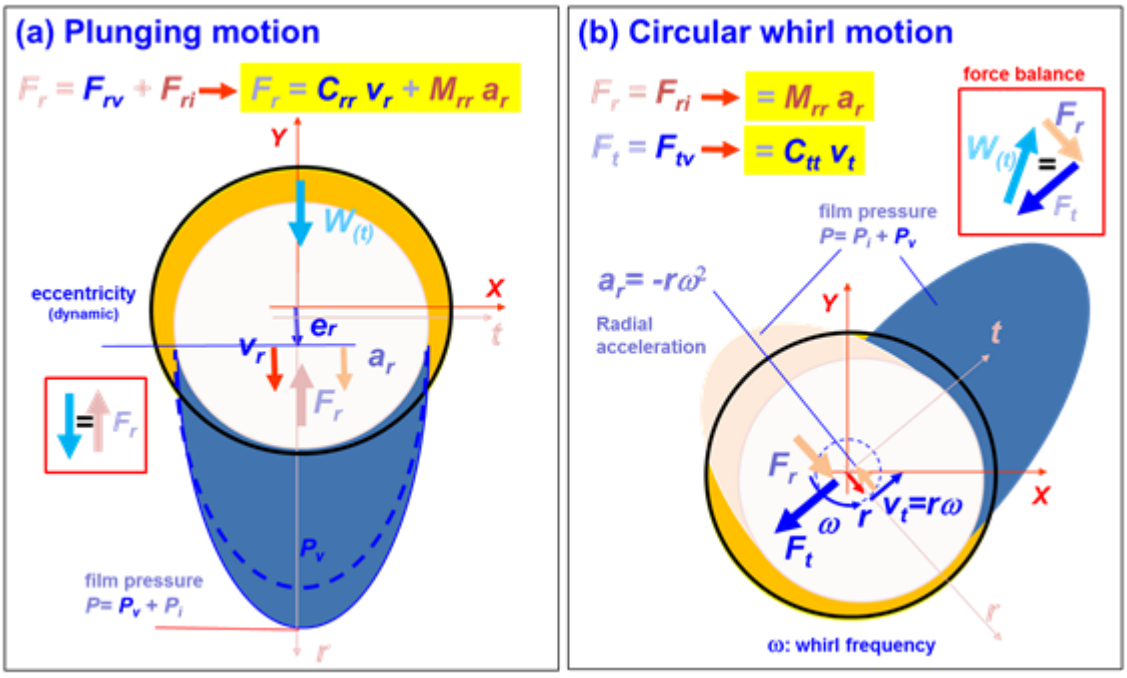

Figure 4. Schematic views of hydrodynamic pressure (viscous + inertia) in a simple SFD undergoing: (a) a plunging motion and (b) a circular whirl orbit motion. Film clearance or gap exaggerated [3].

For an open ends SFD, Refs. [17,18] present a simple correlation between the damping (C) and inertia (M) coefficients with respect to a damper land length (L), radial clearance (c), lubricant density (ρ) and viscosity (μ). These formulas are widely utilized in practice (full-film model and small amplitude ($r \rightarrow 0$) journal center motion);

$$C = C_{XX} = C_{YY} = 12\pi \frac{\mu R^3 L}{c^3}\left[1 - \frac{\tanh\left[L/D\right]}{\left[L/D\right]}\right],$$
$$M = M_{XX} = M_{YY} = \pi \frac{\rho R^3 L}{c}\left[1 - \frac{\tanh\left(L/D\right)}{\left(L/D\right)}\right] \quad (1)$$

Tichy [19-21] also studied the effect of fluid inertia on SFD forced performance. A large clearance (c) damper operating with a high whirl frequency (ω) produces a comparable magnitude of fluid inertia force to viscous force. Furthermore, the presence of fluid inertia tends to alter the shape of the dynamic pressure in a damper film land; in particular, a phase shift in the peak pressure and an increase in its amplitude. These variations of the dynamic pressure are more pronounced in an open ends SFD than in a sealed ends damper. A numerical case study in Ref.[20] shows that including the fluid inertia effect reduces the peak journal motion due to a larger dynamic pressure generation in the damper land compared to a case without fluid inertia.

In the past few decades, researchers [8,22,23] quantify fluid inertia contribution in terms of a radial force (F_R), an added mass (inertia) force coefficient (M), and dynamic pressure profiles. Ref. [8] reports that inertia force coefficients can be as large as the test system physical mass (~17 kg) even for an open ends SFD, thus affecting the overall

performance of a SFD and shifting the test system critical speeds. A vast amount of references stresses that the fluid inertia effect cannot be overlooked and should be properly characterized to predict accurately SFD forced performance.

2.3. Sealed Ends SFDs

Industry demands well-engineered SFDs with a low footprint to reduce cost, maintenance, weight, and space while pushing for higher operating shaft speeds to increase power output. While the open ends SFDs are prone to air ingestion under specific operating conditions, e.g., large amplitude whirl motion and high excitation frequency while demanding of a large through flowrate [24]. The end seals amplify the available damping while reducing the flowrate and reducing air ingestion.

Piston ring seals, end plates and O-rings are commonly used to seal the SFD which increases the damping capability of SFDs while using less lubricant supply. Levesley and Holmes [25] compare experimentally the performance of sealed ends SFDs with different sealing arrangements, in particular with a piston ring seal and an end plate seal. The authors reveal that the piston ring seals provide a larger damping than does the end plate seal. The performance of sealed ends SFD is largely dependent on the seal conductance, which is the inverse of the hydraulic resistance ($1/R$), and must be empirically determined. In general, the SFD direct and added mass coefficients increase with decrease in side leakage and clearance gap of a sealing device [26], yet, a too tightly sealed SFD may lock the rotor bearing system and rendering a SFD ineffective [4].

Miyachi et al. [27] present the experimental SFD damping coefficients for damper with various seal configurations, i.e., O-ring seal, piston ring seal, and simple side seal. With increasing lubricant supply pressure from 1 bar(g) to 4 bar(g), the damping coefficients increase twofold for the piston ring sealed SFD while those of O-ring sealed SFD do not show a significant difference. This difference may be due to the difference in flow resistant of each seal, however, the value is not specified in Ref. [27].

De Santiago and San Andrés [28] evaluate the damping coefficients of an end plate sealed integral SFD (ISFD) supporting an imbalanced rotor. The ISFD damping coefficients are determined from the synchronous rotor amplitude motion at the first critical speed with differing various imbalances. A tightly sealed ISFD with seal clearance of 0.076 mm offers a minimal increase in the damping coefficients compared to an ISFD with seal gap of 0.127 mm. This was explained by the fact that a larger restriction of the leakage results in an increasing lubricant temperature that lowers the oil viscosity.

Meng et al. [29] present the piston ring sealed SFD tangential (damping) force and radial (inertia) force versus lubricant supply pressure and versus lubricant temperature. Figure 6 depicts the serrated piston ring consists of a number of minute dent-like grooves (r_g=0.79 mm) spaced 5º apart along the circumference of a ring. These small grooves allow a sufficient amount of lubricant flow. With increasing supply pressure, tangential and radial forces increase. With oil temperature rise, tangential force increases somewhat. The authors' further note that the partially sealed SFD is more prone to oil

cavitation than an open ends SFD by trapping the air bubbles in the damper land, which leads to a smaller generation of tangential (damping) forces.

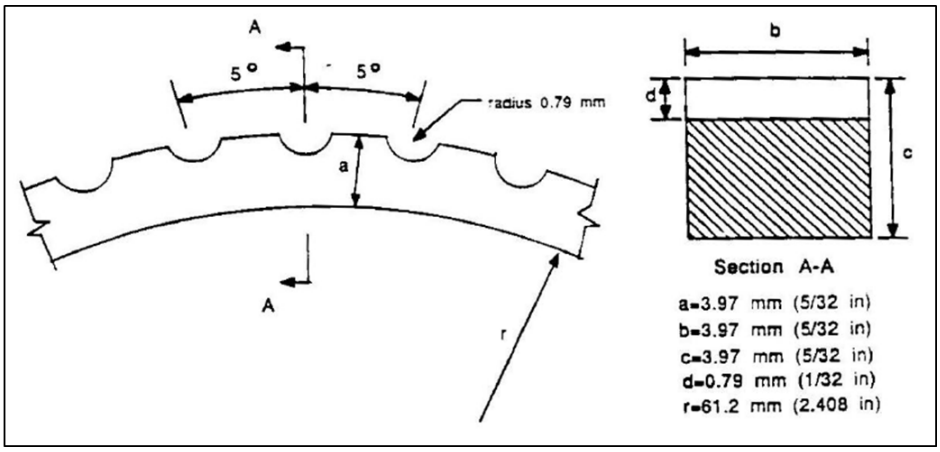

Figure 5. Geometry of a serrated piston ring, adapted from [29].

Arghir and Defaye [30] investigate the SFD radial and tangential forces for sealed ends damper with two types of piston ring seals, as shown in the Figure 5. The first pair of piston ring has one slit, while the second pair has six openings circumferentially. The second type of piston rings provides 3.1 times larger flow conductance (smaller flow resistance) than the first pair with only one slit. Note that the leakage flow evacuates heat generated by the squeeze film effect. The piston ring sealed damper with seven openings at each end reduces the jet effect caused by a localized leakage through the PR slit and thus decreases the tangential force by ~20% compared to the force obtained with the piston ring with one slit.

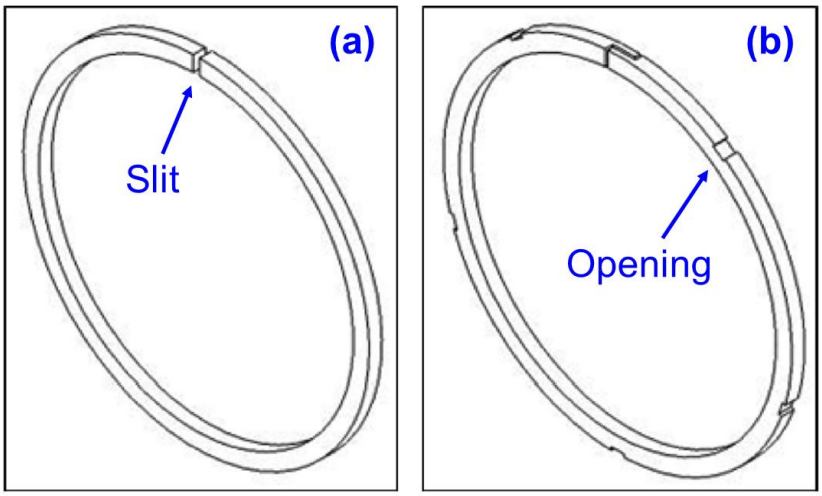

Figure 6. Two types of piston ring seals: (a) with one slit and (b) with six openings, adapted from [30].

Recently, San Andrés and Seshagiri [31] experimentally quantify the dynamic forced performance of piston ring sealed SFD with a central feed groove. The test results are thoroughly correlated with those of an identical damper with the open ends [32]. As expected, the piston ring seals effectively increase the generation of pressure in the film lands by restricting the oil leakage. Subsequently, the sealed end SFD produces more than twice the amount of SFD damping and inertia than those from the open ends SFD. The experimental identified SFD force coefficients are compared against the prediction [7] using an empirically determined seal end flow conductance. Experimental and predicted SFD coefficients match closely when also accounting for the effective groove depth as in Refs.[33,34].

2.4. SFDs Undergoing Transient Dynamic Loads

Researchers have studied the forced response of a SFD subjected to (sudden) transient events. In general, these studies can be categorized by the source of the excitation; that is, by a transient event due to the unbalance response of a rotor, in particular for a blade loss event [9,35-38]; or by the movements of bearing support bases, especially for a seismic excitation or impact loads [6,10,39-42].

Refs.[35-38] deliver relevant numerical studies that characterize the transient nonlinear response of an aero-engine experiencing a blade loss event. Only a few works [35,37], however, have further validated the studies against experimental data. These experimental studies show that an increasing unbalance force could lead to a large transmissibility ($T_r > 1$), rendering the SFD ineffective and leading to premature bearing failure. In Ref.[37], increasing the oil supply pressure to a sealed ends SFD from 3.4 bar to 5.5 bar reduces substantially the amplitude motion of the rotor.

San Andrés et al. [9] present measurements of an open ends SFD dynamic performance for a transient event with sine-sweep frequency at a constant angular acceleration. Identified SFD force coefficients from a sine-sweep frequency dynamic load with a low angular acceleration (α=6.5 Hz/s) show a good agreement with those from a single-frequency dynamic load over the same test conditions. The same cannot be said, however, for coefficients identified from a dynamic load with too fast angular acceleration. This is because a too-fast change in frequency prevents the system from achieving a quasi-steady-state response at a discrete or particular frequency, hence the

system does not displace as needed for the accurate calculation of complex stiffnesses in the frequency domain.

Hori and Kato [39] study the seismic response of a turbomachine in an effort to answer the major question of whether a rotor-bearing support can withstand an earthquake, another example of a transient load. Roberts et al. [40,41] utilize a linear model of the squeeze-film to determine the SFD force coefficients, damping and inertia, from a freely decaying transient response experimental data. The damping and inertial coefficients are validated against the predictions and found to be independent of a frequency of vibration.

Lee et al. [42] demonstrate both analytically and experimentally that a transient response of the rotor-bearing system is sensitive to the time duration of an external shock. These numerical analyses gauge the robustness of rotating machinery withstanding an external shock.

Most recently, San Andrés and Jeung [6,10] performed measurements of the transient response of a single-land open ends SFD due to large impact loads. The measurements show that a large change in speed ($a_r >> 0$) induces large fluid inertia force comparable to the purely viscous force with increasing impact loads (see Figure 4). A large increase in SFD inertia coefficients (M) leads to a moderate increase in the test system damping ratio since $\xi \sim C/M$. Interestingly enough, Ref.[10] shows experimentally that the presence of fluid inertia tends to reduce the peak system dynamic response.

2.5. Identification of Bearing Parameters

The bearing dynamic force coefficients such as stiffness, damping and inertia influence the dynamics of a rotor-bearing system. Accurate identification of bearing force coefficients is crucial to design and diagnose and to solve vibration issues in rotating machinery.

In 2004, Tiwari et al.[43] summarize the bearing parameter identification methods and categorize them in terms of bearing types, domain used for identification (time and frequency), and excitation type. The basic concept of bearing parameters (*K*,*C*,*M*) and governing equation is well explained and the assumptions for the bearing models are discussed.

In 1985, Fritzen [44] introduces the Instrumental Variable Filter (IVF) method that utilizes transfer functions to iterate the least square algorithm until it reaches a given convergence criteria. This method is powerful when noise presences in a measurement. The iteration process minimizes the approximation errors and thus leads to consistent estimation of bearing parameters (*K*, *C*, *M*).

In 1990, Rouch [45] evaluates the force coefficients of a central grooved SFD utilizing a frequency domain technique. The tests are performed based on the sweep sine excitation up to 500 Hz and with various lubricant supply temperatures. Separating the real and imaginary parts of the recorded transfer functions (output/input) allows an estimation of the effective SFD stiffness and damping coefficients, respectively. For low lubricant viscosity, the real part of the complex dynamic stiffness, which represents the SFD effective stiffness K_{eff}, shows a decrease at a high whirl frequency. This decreasing

trend is ascribed to fluid inertia effects, however, the author did not quantify the inertia coefficients. Note that the effective stiffness is defined as

$$K_{X-eff} = K_{XX} + C_{XY}\omega - M_{XX}\omega^2 \tag{2}$$

where the effect of the direct inertia force coefficient becomes substantial at a high whirl frequency.

Lund et al. [46] demonstrate experimentally and numerically the force coefficients of an O-ring sealed SFD with a central feed groove. As in Ref. [8], zero-order and first-order equivalent Reynolds equations are derived from the continuity equation and a first-order perturbation solution is carried out while the central groove is modeled with a bulk flow. The experimental SFD force coefficients are compared with those from predictions for various oil groove depths. The predictions correlate well with the damping coefficients, but over predict the inertia coefficients by up to ~60%. Furthermore, this discrepancy increases with increasing central groove depth. Later, Delgado and San Andrés [33,34] introduce a concept called "*effective groove depth*" to bridge the gap between the theory and experimental results. An effective groove depth differs from the physical groove depth as it represents the upper boundary of the squeeze film flow in the groove that contributes to the overall forced performance of SFD. This concept substantially reduced the discrepancy between predictions and experimental data.

Arghir et al. [23] present an improved bulk-flow model incorporating the fluid inertia advection effect to predict the forced performance of SFDs. The model addresses the effect of oil feed orifices and grooves where a strong unsteady flow and a large change

in mass flow is present. The predictive model correlates well with the experimental SFD force coefficients and pressure measurements reported in Ref. [29].

Hassini and Arghir [47,48] present a simple method to evaluate the nonlinear fluid film forces from a transfer function based on the Laplace transform. The inverse of the Laplace transform of the perturbed forces leads to obtain a set of ordinary differential equations. These equations are valid only for infinitesimal small amplitude motions, however, a large motion can be approximated by a combination of small displacement perturbations. This method results a good agreement with the nonlinear model solving transient Reynolds equation and reduces the computational time by half.

Most recently, San Andrés and Jeung [7] present an *orbit analysis* method to estimate the bearing force coefficients from numerical simulations. This model numerically replicates experimental procedures that specifies the journal motions ($\mathbf{z}_1$) of forward whirl orbit and predicts the fluid film reaction forces ($\mathbf{F}_1$). The dynamic reaction force is approximated by utilizing a Fourier series decomposition $\mathbf{F}_{\mathbf{dyn}} \approx \mathbf{F}_1 e^{i(\omega t+\phi)}$. The numerical simulation stipulates a backward whirl orbital path ($\mathbf{z}_2$) to estimate the reaction force ($\mathbf{F}_2$). The set of forward and backward whirl motions ($\mathbf{z}_1$,$\mathbf{z}_2$) ensure linear independence of two SFD forces ($\mathbf{F}_1$,$\mathbf{F}_2$). This enables the determination of a 2x2 complex dynamic stiffness (**H**) matrix over a certain whirl frequency ω_k. By curve fitting **H** over the range of frequency ($\omega_{k=1,2,\ldots N}$), the bearing force coefficients (K,C,M) are determined. The identified bearing force coefficients can be predicted for large amplitude periodic motions, journal off-centered conditions and a wide range of frequency. The orbit analysis leaps beyond (conventional) linearized force coefficients

which are derived from infinitesimally small amplitude motions about an equilibrium position. The model is benchmarked to the experimental results [3,5,6,8,11,31,32] proving excellent correlations that prove its fidelity.

2.6. Summary of Work in Seven Years of SFD Project at Texas A&M University

In 2008, a major aircraft gas turbine manufacturer funded a multiple year research work to build a dedicated test rig to investigate novel SFD configurations operating at typical conditions encountered in aircraft jet engines and to measure their dynamic forced performance. The design and construction of a high load SFD test rig consisting of a rigid journal and an elastically supported bearing cartridge (BC) took place in 2009.

2.6.1. Open Ends Squeeze Film Dampers with a Central Feed Groove

Figure 7 depicts the BC used to make dampers A and B with a central circumferential groove configuration. The damper A features an open ends SFD with two parallel film lands, L_A=25.4 mm, separated by the circumferential groove of length L_G=12.7 mm, while damper B features an open ends SFD with two film lands, L_B=12.7 mm, separated by the central circumferential groove L_G=12.7 mm. Both dampers have an outer diameter D=127 mm, a central groove with depth of 9.6 mm and 12.7 mm length, and radial clearances c_A=0.141 mm and c_B=0.138 mm. Three radial orifice feed holes (diameter = 2.5 mm) spaced 120° apart on the journal supply lubricant to the squeeze film lands.

Results from circular orbits (CO) tests performed on damper A confirmed larger damping and added mass coefficients for a lubricated system than for the *dry* system (without lubricant). As in Ref. [32], the experimental findings show that direct damping coefficients increase moderately with the static eccentricity, but are insensitive to the orbit amplitude. Direct inertia coefficients decrease as the orbit amplitude increases and remain nearly constant with static eccentricity. The cross-coupled damping and inertia coefficients are a small fraction of the direct coefficients. In addition, measured film pressures in the groove are similar in magnitude with the dynamic pressure in the film lands. The measurements demonstrate that a groove does not isolate the film lands from each other but interact with the film lands to generate large damping and inertia coefficients that affect the forced performance of the test SFDs.

Testing continued with dampers A and B with slight changes to the test conditions. The experiments aimed to determine the performance of long (A) and short (B) length dampers with open ends and sealed ends. The major findings from circular orbit tests show that the long length (2 x 25.4 mm lands) open ends damper A produces ~ 7 times more direct damping than the short length (2 x 12.7 mm lands) damper B and ~ twice times larger added mass coefficients. Both dampers generate large added mass coefficients because the central groove does not isolate its adjacent film lands. The groove generates large inertia reaction forces that contribute significantly to the forced performance of the test articles.

For damper A, elliptical orbit tests ($\Delta X/\Delta Y$=2:1 and 5:1 amplitude ratios) were conducted at centered (e_s=0) and two eccentric positions (e_s = 31.8 μm and 51.8 μm).

The force coefficients extracted from either rectilinear motions or circular orbits or elliptical orbits, with amplitude ratios as high as 5:1, are essentially identical. Interestingly enough, the SFD damping and inertia coefficients are similar for similar amplitudes of major axis motion (ΔX), demonstrating the coefficients are insensitive to the type of journal motion.

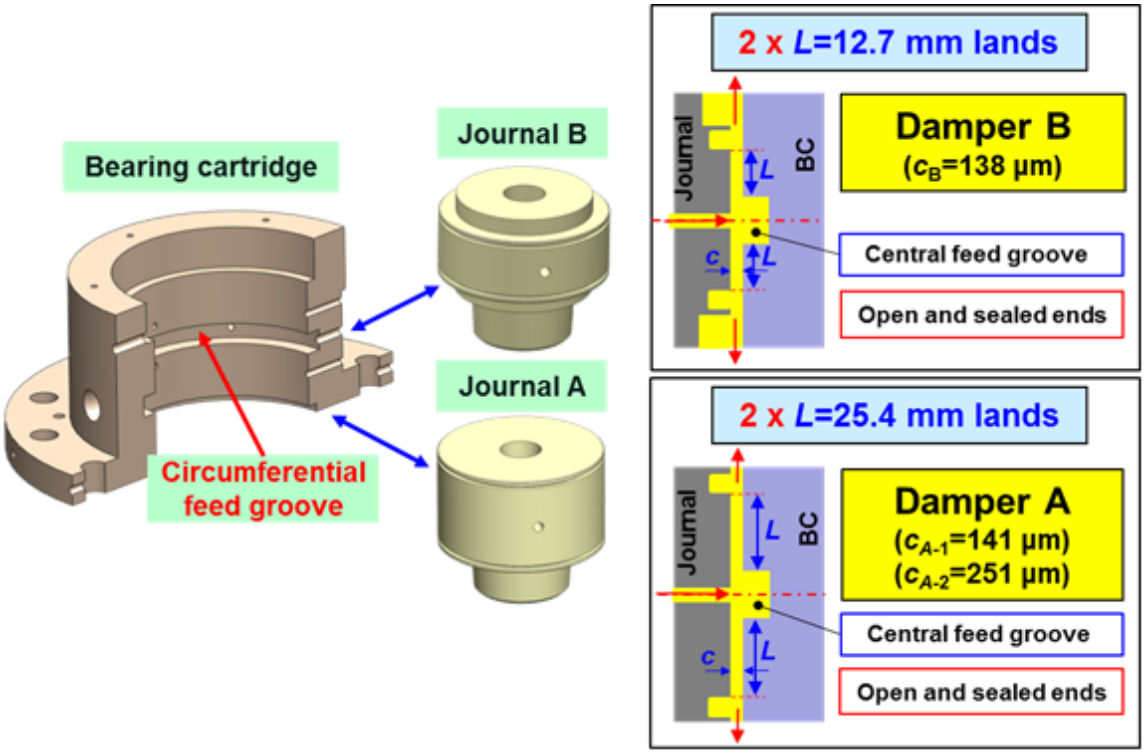

Figure 7. (a) Isometric and (b) cross-section views: bearing cartridge with circumferential feed groove (12.7 mm width and 9.5 mm depth) and test journals A and B to make dampers A and B [3].

2.6.2. Sealed Ends Squeeze Film Dampers with a Central Feed Groove

In 2011, more experiments continued prior work and aimed to identify force coefficients from circular orbits for short length damper B sealed with piston rings. Conditions included orbit amplitude equal to 5.5% of the bearing clearance and a static eccentricity as large as 37% of the radial clearance. The goal was to elucidate the effects of end seals on the dynamic forced performance of a short length SFD (B) and a long length SFD (A), both configured with a circumferential groove.

Experimental results show that the short length damper B with end seals provides two times more inertia and ~3.8 times more damping than when configured without end seals (i.e., open ends). The sealed ends long length damper A provides ~3.1 times more inertia and ~2.8 times more damping than the same configuration without end seals. Moreover, proper installation of the piston rings (orientation of slit face) is paramount in ensuring the lowest side leakage and an increase in damping force coefficients. The experimental results suggest a short length SFD is much more desirable since it generates less fluid inertia and more damping. Refer to Ref. [31] for details on the experimental findings.

2.6.3. Single Film Land Squeeze Film Dampers with End Grooves

In light of the prior findings, an overhaul of the test rig took place in 2012, which included the elimination of the circumferential (central) feed groove. Figure 8 depicts the BC configured without a central groove feed and the test journals C/D, E/F (small/large clearance). A new journal, C (c_C=130 μm), with end grooves (provisions for installation

of end seals) was fabricated to achieve a short land length, L/D=0.2. The end grooves are 2.5 mm length and 3.8 mm in depth. Three radial orifice feed holes (diameter = 2.5 mm) spaced 120° apart on the journal supply lubricant directly to the mid plane of the single film land. The modifications reflect damper configurations used by a major aero-engine manufacturer. The short damper configuration offer advantages such as reduced overall weight and space.

Experimental results show dampers C and E produce direct damping coefficients that are invariant with orbit amplitude, but increase with static eccentricity. On the other hand, the SFD direct inertia coefficients decrease linearly as the orbit amplitude increases and remain invariant with static eccentricity (e_s). Finally, the SFD cross-coupled damping and inertia force coefficients are generally small in magnitude when compared to the direct force coefficients.

Incidentally, dampers C and D have deep grooves at their ends for the installation of piston ring seals. Also, the end seals are not in place for experiments with open end conditions. Continued experimentation on open ends dampers C and D also demonstrates that the pressures in the end grooves are not nil, and at high whirl frequencies (ω >100 Hz), the end grooves pressure is as large as 20% of film pressure at the mid plane. This observation makes for the computation model to use an effective axial length, (L_{eff}), which includes effects from the end grooves, rather than the design film land (L). With the inclusion of L_{eff} in the computational model, the predicted damping coefficients are closer to the experimental ones. Thus, correct modeling of the end grooves is necessary for better predictions of SFD force coefficients. Reference [5]

gives further details on the film dynamic pressure measurement and the experimentally identified force coefficients.

Afterwards, comparisons of test results for test dampers B and C (with and without the central groove. L_G=12.7 mm) evidence both damper configurations offer similar damping coefficients. On the other hand, the grooved damper (B) shows 60% larger inertia force coefficients. Recall both dampers have similar physical dimensions; c_B=138 μm vs. c_C=130 μm and a total film land length of L=25.4 mm. Realize damper C (without a central groove) is 12.7 mm shorter axially, which is desirable for saving space and weight while providing comparable damping as that in damper B. However, damper B, the one with a circumferential feed groove, maintains a higher static pressure between feedholes, hence preventing unfavorable operating conditions such as lubricant vapor cavitation and air ingestion. Ref.[3] details the comparison of force coefficients between dampers B and C.

In 2013, the test program examined the effects of varying film clearance and varying the number of active feedholes on the dynamic forced performance of two short length, single land (L=25.4 mm) dampers. Damper D has a large radial clearance (c_D=0.254 mm) whereas damper C has c_D=130 μm. The small clearance damper C produces roughly four times more damping and two times more inertia than the large clearance damper D.

Piston ring sealed ends damper C operating with only one or two feedholes exhibits up to 30% larger damping coefficients and up to 50% larger inertia coefficients than those coefficients identified for the sealed ends damper C operating with three feedholes.

When operating with one or two feedholes, the force coefficients show anisotropy, e.g. $M_{XX} \neq M_{YY}$.

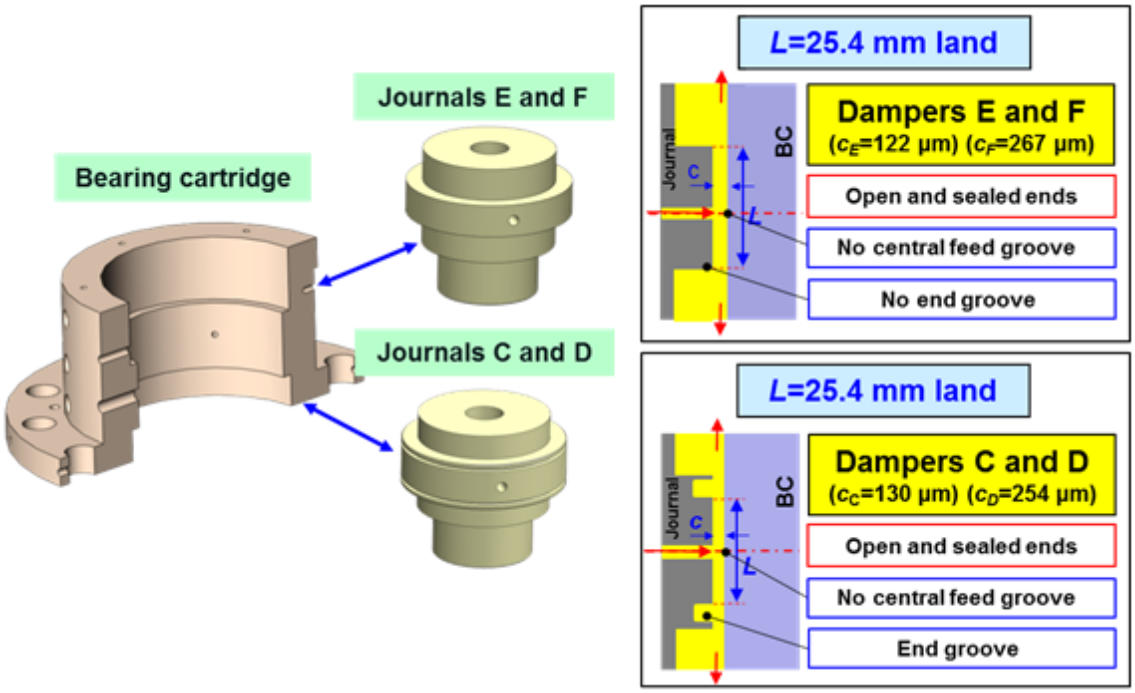

Figure 8. (a) Isometric and (b) cross-section views: bearing cartridge without circumferential feed groove and test journals C and D to make dampers C/D and E/F [3].

2.6.4. Single Film Land Squeeze Film Dampers without End Grooves

In light of the Ref.[1-5] and many others evidencing the generation of dynamic pressure at the grooves, further work proposes the simplification of the journal design by eliminating the end grooves. In 2014, a new journal, E, without end grooves was manufactured (see Figure 8). Ref. [49] presents the major findings from the proposed work with two short length, single land (L=25.4 mm) dampers E and F. The dampers E and F, L/D=0.2, differ in radial clearance, c_E=0.122 and c_F=0.267 mm, respectively.

Comparisons of experimental results between dampers D and F (similar radial clearance and differing total land lengths), and dampers E and F (differing radial clearances and identical land length) show that the force coefficients closely conform to theoretical relationships derived from classical lubrication theory. Damper D (c_D=0.254 mm, with end grooves) produces 1.75 times more damping and 2.12 times more added mass than damper F (c_F=0.267 mm, with no end grooves). Damper E (c_E=122 mm, with no end grooves) produces 8 times more damping and 1.9 times more added mass than damper F. The fluid film dynamic pressures are largest for damper E, roughly twice as large as the other configurations when considering orbit amplitude. On the other hand, the fluid film dynamic pressures in damper D are only slightly larger than the pressures measured in damper F.

Work in 2008-2014 [3,5,6,7,8] thoroughly documents the procedure for identification of SFD stiffness, damping, and added mass coefficients (K, C, M); experimentally demonstrate the effects of static eccentricity (e_s) and orbit amplitude (r) on the force coefficients; and characterize the fluid film dynamic pressure for SFDs whirling with circular orbits, centered and off-centered. Additionally, the work in the multi-year project also quantified effects on the damper forced performance of feed groove versus feedholes, land length (L), radial clearance (c), incorporating end seals, and plugging feedholes. The work led to the culmination of a comprehensive lecture in Ref.[3] that aims to provide industry practitioners with a working knowledge of SFDs. The monumental reference [3] also dispels common misconceptions of SFDs widely accepted in practice.

As such, the experimental work in 2015 evaluated the response of a test SFD rig to transient events. In particular, exploring the response of SFDs to operation at a large static eccentricity (bottomed journal) due to maneuver loads, and to startup/shutdown (or ramp/spool up and down) events. Reference [9] further details the experimental results for largely off-centered motions, and conditions causing a rotor to exhibit highly elliptical whirl orbits.

Reference [9] advanced the analysis of the SFD response to transient events by performing tests with a sine-sweep (increasing or varying) frequency dynamic load to simulate a startup event. Motions departing from a largely off-centered position ($e_s/c \rightarrow 1$) are smaller in amplitude than those from a centered condition ($e_s/c=0$) due to the larger damping produced by a very small film thickness. For the same reason, the lubricated system operating at $e_s/c \rightarrow 1$ exhibits resonance frequencies that are lower than those for the system operating at $e_s/c=0$. Moreover, for motions departing from a largely off-centered position, the whirl orbit becomes highly elliptical when traversing a system natural frequency. At a largely off-centered condition ($e_s/c=0.99$) and for a low excitation frequency (ω < 20 Hz), intermittent contact occurs between the damper journal and its housing as evidenced by recorded large magnitude dynamic pressures (on the order of MPa).

3. DESCRIPTION OF THE EXPERIMENTAL FACILITY AND TEST DAMPERS

This section details a description of the test facility and test squeeze film damper including flow rate measurements through the films.

3.1. Test Rig Description

Figure 9 shows a photograph and a top view schematic of the current SFD test rig assembly. The test rig consists of three main components: a test SFD bearing, two electromagnetic shakers and a hydraulic static loader. The two orthogonally placed shakers and the static loader, 45° away from each shaker, are firmly mounted on an iron table. The static loader enables displacement of the bearing cartridge (BC) to various static eccentricity conditions while the shakers, via slender stingers connecting to the BC, enable the BC dynamic displacement.

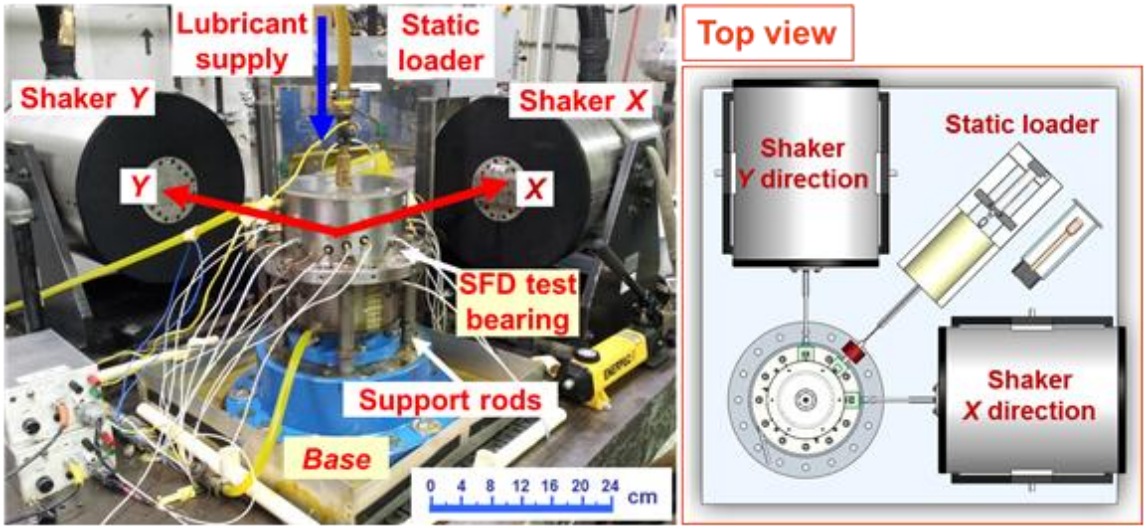

Figure 9. Picture and top view of SFD test rig with electromagnetic shakers and static loader.

Figure 10 shows the main components of the test SFD bearing. The SFD support structure consists of flexural rods attached to the BC on one end and attached to the rigid pedestal on the other. The number of rods can be changed to increase or decrease the structural stiffness, thus replicating a squirrel cage (elastic) support. The actual SFD consists of an interchangeable test journal bolted to the journal base, itself rigidly fastened to the pedestal. Meanwhile, the annular gap between the outer surface of the test journal and the inner circumference of the BC constitutes the film land. This configuration allows the test journal to be easily exchanged. Appendix A details the measurement of the SFD component dimensions (journal and bearing cartridge).

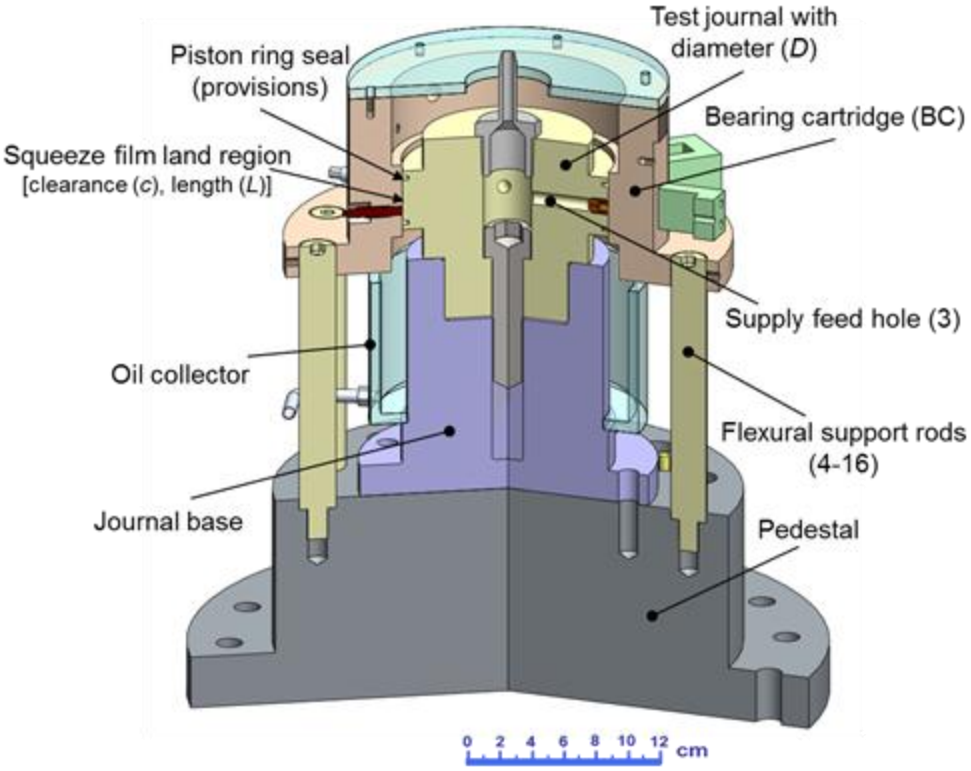

Figure 10. Cross-sectional view showing overview of SFD test bearing section (cut-section view) [5].

Figure 11 shows a cross-section view of the SFD test rig with a 127 mm outer diameter journal and also illustrates the path of lubricant flow through the system. Light lubricant, ISO VG2 is supplied into the SFD through a hole in the top of the stationary journal via an external oil pump gear. Oil is forced through three orifices (ϕ = 2.54 mm) spaced 120° apart in the journal and flows into the mid axial plane of the squeeze film land (z=0). The lubricant exits through the top and bottom ends of the bottom film lands to ambient pressure and discharges to oil collecting chambers. The return pump moves the oil in the collector to a reservoir tank for recirculation through the system. Appendix B presents the measurements of lubricant viscosity versus temperature. In brief, the measured lubricant (ISO VG2) viscosity is μ=2.65 ± 0.08 cP (0.384 micro-Reyns) and density is ρ=800 ± 24 kg/m^3 (50 lb/ft^3) at room temperature T=23.0 ± 0.5 °C (73°F).

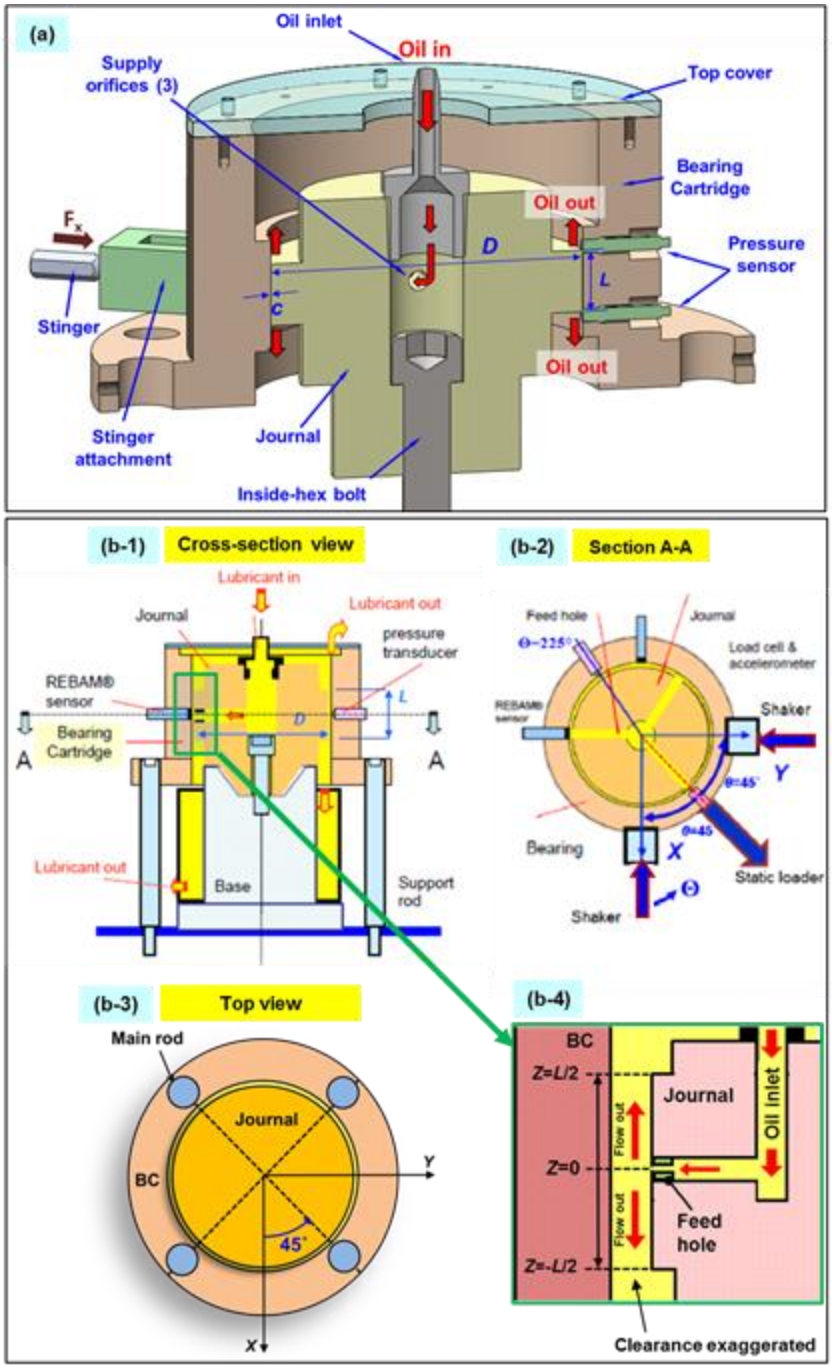

Figure 11. (a) Schematic view of SFD test section with physical dimensions (*L*=25.4 mm, *D*=127 mm, c_B=0.267 mm) and lubricant flow path. (b-1) Cross-section view of SFD test rig. (b-2) Cross-section view of section A-A showing position of shaker and static loader. (b-3) Top view showing position of flexural support rods. (b-4) Lateral view of SFD journal and BC showing the film land length (*L*). Exaggerated film clearance for illustrative purposes

Figure 12 depicts views of test dampers A and B for visual comparison, and Table 1 shows the dimensions of the two test dampers. Note that the nominal radial clearance for dampers A and B is c_A= 0.254 mm (10 mil) and c_B= 0.267 mm (10.5 mil), respectively. The two dampers have the same axial film length L = 25.4 mm (1 in). However, the journal in damper A includes, at the top and bottom sides of the film land, end grooves for installation of piston ring end seals. The end grooves have a width and depth equal to 2.5 mm and 3.8 mm (~15c_A), respectively. The end lips have a width equal to 3.3 mm (see inset) and chamfered edges make a small clearance ~1c_A to 4c_A with the BC inner diameter. The total oil wetted length for damper A ($L_{A\text{-}tot}$) equals 36.8 mm (1.45 in). Note that the effective film length[1] for open ends damper A, L_{eff}=29.7 mm, is larger than the designed film land length L=25.4mm, and shorter than the actual wetted length, $L_{tot}>L_{eff}>L$.

[1] A curve fitting of the measured dynamic pressure profile as a parabolic function of the axial coordinate (z) estimates the effective film land L_{eff}. See Ref.[5] for details.

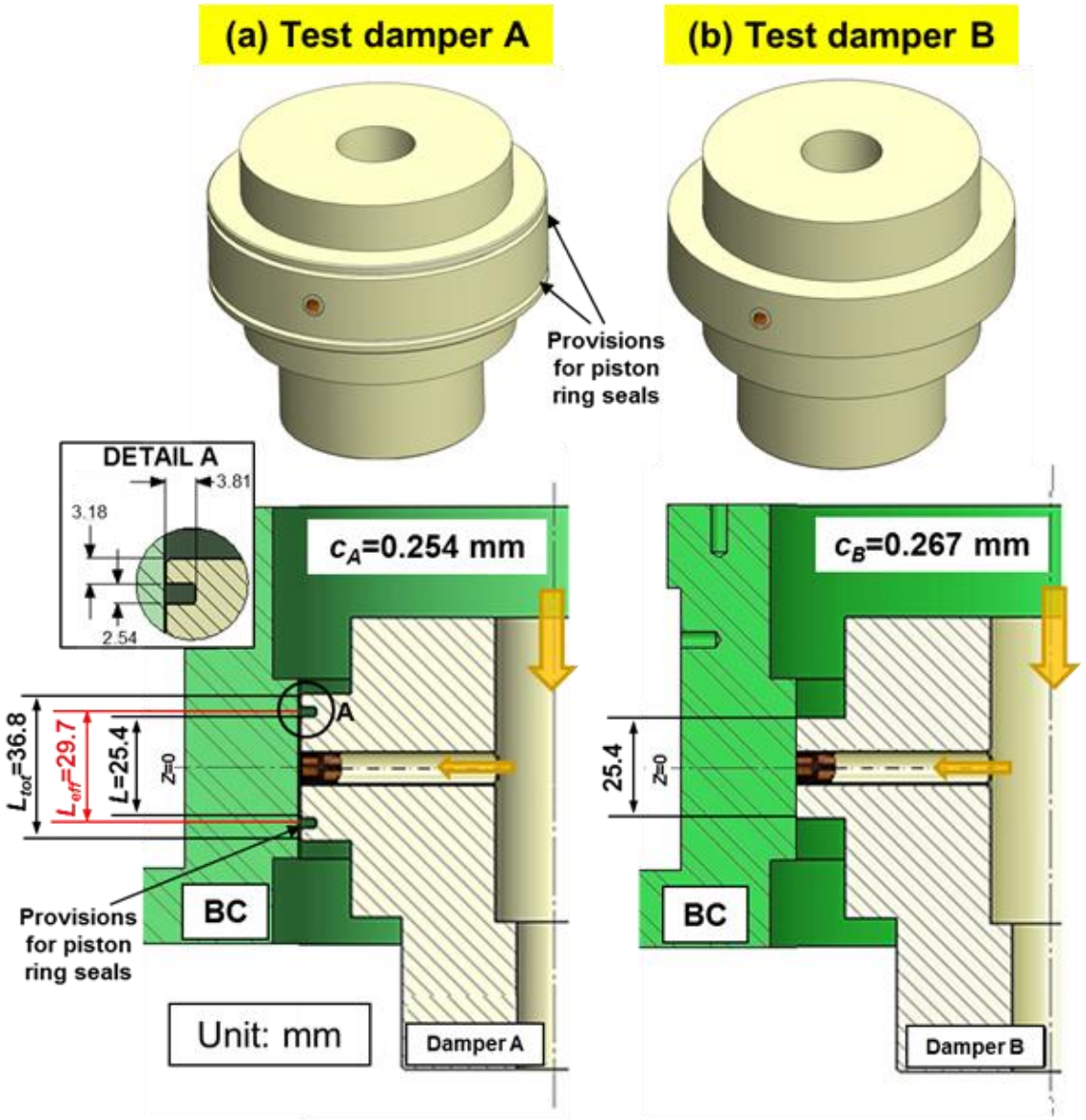

Figure 12. Test damper A (c_A=0.254 mm) with end grooves for installation of piston rings, and damper B (c_B=0.267 mm) with uniform film land. Film land length 25.4 mm (L/D=0.2).

Table 1. Important dimensions for test dampers A and B (*L*/*D*=0.2)

Damper Type	Film land length, L (mm)	Damper diameter, D (mm)	Radial clearance, c (mm)	Ends condition	End Grooves	Groove Width, L_G (mm)	Groove Depth, D_G (mm)
A	25.4	127	0.254	Open, Sealed	Yes	2.5	3.8
B			0.267	Open	No	-	-

Figure 13 shows (a) a piston ring (PR) and (b) the journal with the piston rings installed. The piston rings outer diameter, when closed, equals to the ID of the BC; that is 127.16 mm. Note that there exists a radial gap of 0.46 mm between the piston rings ID and the end groove OD in the journal. Figure 14 shows a schematic view of the installed piston rings and the angular location of the feedholes in the journal. When installed, a PR slit is located 60° away from adjacent feedholes to minimize lubricant leakage. Locating the PR slit near the feedhole will increase leakage. This is because the PR slit is the only route for the lubricant flow to evacuate the damper.

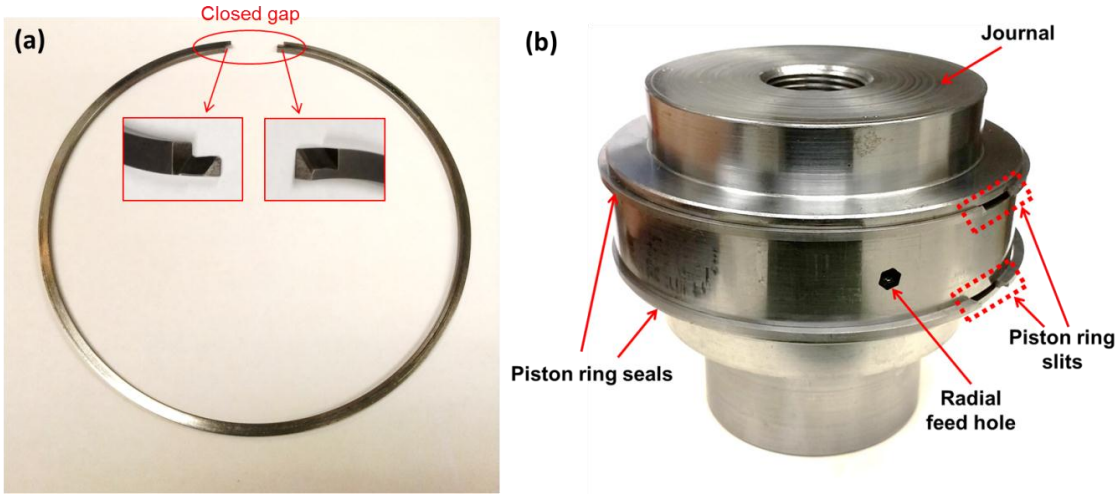

Figure 13. (a) Photograph of piston ring seal (dimensions are proprietary) and (b) piston ring seals installed in the end grooves of the journal.

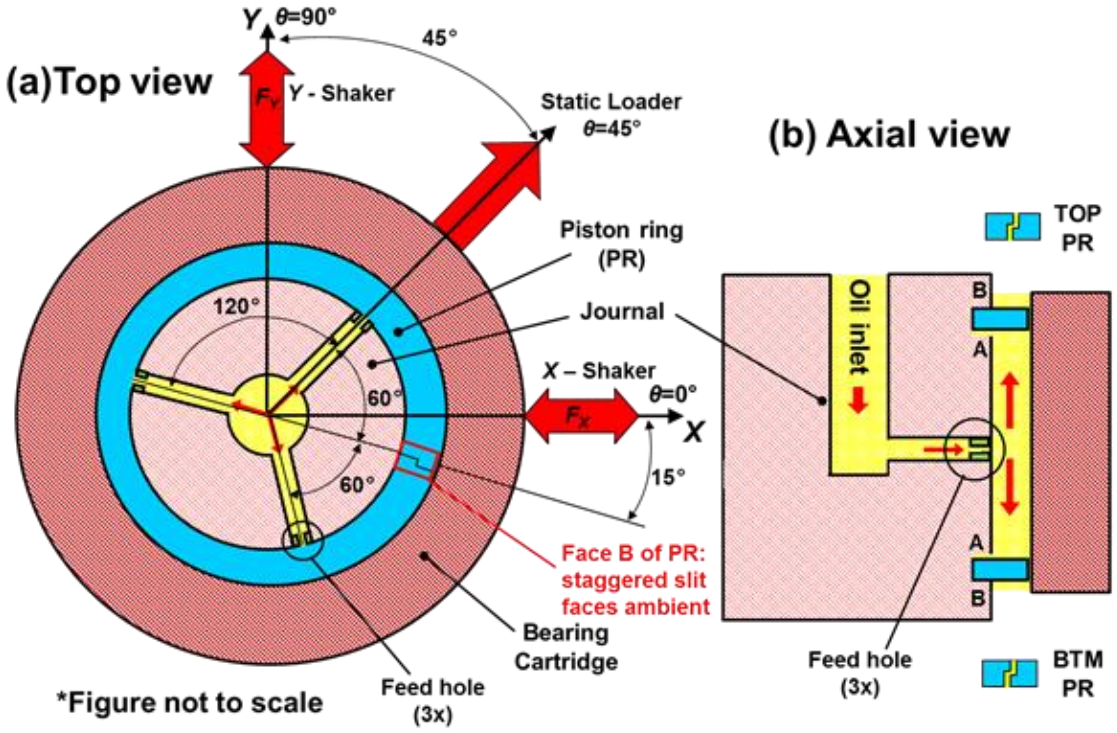

Figure 14. Piston ring installation orientation (a) circumferential and (b) axial.

3.2. Flow Rate Measurements Under a Static Condition

This section presents the characterization of the flow conductance (C) for the open ends SFD as well as the flow conductance for the piston rings (PR) in the sealed ends SFD. The sealed ends damper performance depends largely on its flow conductance (later, see Fig. 36).

Figure 15 depicts a hydraulic circuit representing the lubricant flow path and flow resistances (R). Lubricant flows into the damper film land through three uniformly spaced orifices with flow resistance (R_o). The oil then flows through the top and bottom land sections of the SFD. The journal with 12.7 mm (0.5 inch) film land, above and below the feedholes, has flow resistances, R_{TL} and R_{BL}, and the piston rings have flow

resistances R_{TS} and R_{BS}. Subindices T and B denote the top and bottom land sections of the damper.

A pressure gauge displays the inlet pressure (P_{in}) of the lubricant before it enters the SFD test rig. A flow meter records the inlet flow rate (Q_{in}) while the outlet flow rate through the top and bottom sections (Q_T and Q_B) are determined via the time required to fill a known volume in the oil collector beneath the BC. For a damper with a uniform clearance (BC and journal perfectly centered and aligned), the ratio of bottom land flow to inlet flow must equal 50%, Q_B/Q_{in}=0.50.

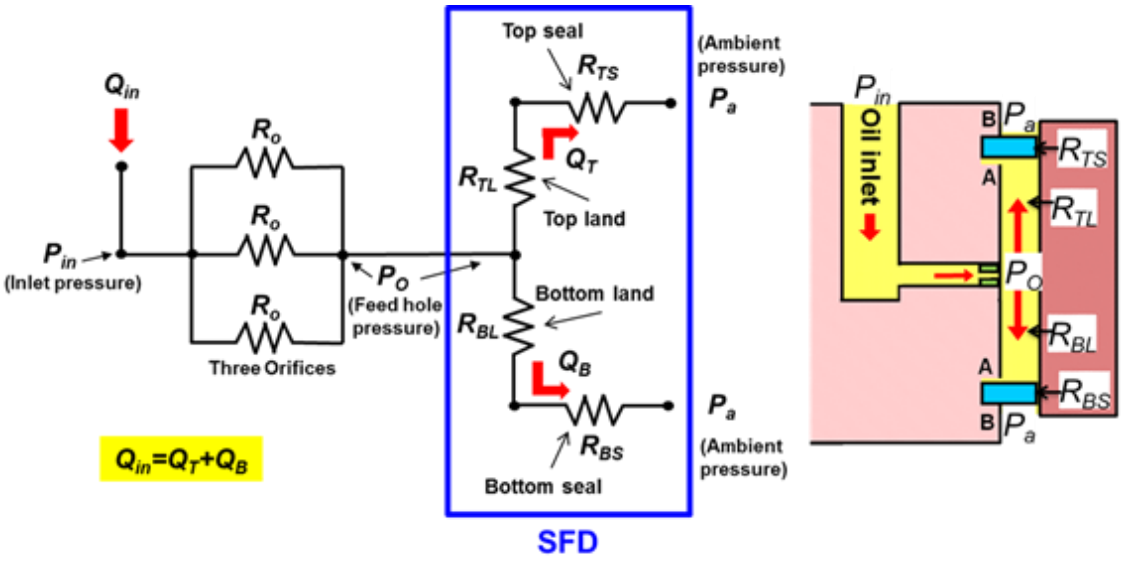

Figure 15. Flow diagram with hydraulic resistances for a sealed ends SFD.

For the top and bottom film land sections, the flow resistance and end seal fluidic resistances (R) are in series. Hence, a simple hydraulic analysis gives

$$Q_{in} = \frac{P_{in} - P_O}{(R_O/n)} = Q_T + Q_B$$

$$Q_T = \frac{P_O - P_a}{R_{TL} + R_{TS}} = \frac{P_O}{R_T} = C_T P_O;\; Q_B = \frac{P_O - P_a}{R_{BL} + R_{BS}} = \frac{P_O}{R_B} = C_B P_O \tag{3}$$

Above, C_T and C_B denote flow conductances ($1/C=R$) and P_a=0 is ambient pressure.

Table 2 lists the recorded inlet pressure (P_{in}), supply (Q_{in}), top (Q_T) and bottom (Q_B) flow rates, the ratio Q_B/Q_{in}, and the calculated bottom flow conductance (C_B). The measurements correspond to both open and sealed ends SFDs. Moreover, the recorded Q_{in} and P_{in} for estimation of the orifice conductance $C_o=1/R_o$ are also listed. Figure 16 depicts graphically the flow rate measured in both open and sealed ends SFD versus supply pressure (P_{in}). Note that pressure at the feedhole P_O is estimated from Eq.(3).

In an open ends damper at the centered position (e_s/c=0), The theoretical flow rate ($Q_{in\text{-}theory}$) through a thin film land (two parallel planes) of uniform clearance (c) and length (L/2)

$$Q_{in-theory} = \frac{\pi D c^3}{12\mu} \frac{(P_O - P_a)}{(L/2)} \tag{4}$$

However, Eq.(4) assumes P_O acts over the whole circumference of the film land (πDc). Note the SFD has three feedholes 120° apart (see Figure 14) and the static pressure sharply drops in between the holes [50], as shown in Appendix C. As a result, the theoretical flow rate does not correlate well with the measured one, $Q_{in\text{-}theory} \sim 5 \cdot Q_{in}$.

Hence, the flow conductance of the SFD with three feedholes is estimated based on the flow rate measurements.

For an open ends damper A with c_A=0.254 mm, the flow conductances of the top and bottom lands are:

$$C_{TL} = \frac{1}{R_{TL}} = 8.43 \frac{\text{LPM}}{\text{bar}} \text{ and } C_{BL} = \frac{1}{R_{BL}} = 9.59 \frac{\text{LPM}}{\text{bar}} \tag{5}$$

Both top and bottom film lands offer similar flow conductances, albeit bottom land offers 14% larger conductance (C_{BL}/C_{TL}=1.14). The difference is most likely due to the uncertainty in the measurement of the flow through the bottom side of the damper (± 5%) and the journal and indicating the BC may not have been perfectly aligned. Notice that the conductance of one orifice is $C_O = 10.07 \, \text{LPM}/\text{bar}$ (see Table 2(a)).

For the top and bottom ends sealed damper A, the flow resistances (and conductances) are calculated as

$$\begin{aligned} R_{TS} &\cong \frac{1}{C_{TS}} = \frac{1}{C_T} - \frac{1}{C_{TL}} = 1.62 \frac{\text{bar}}{\text{LPM}} \rightarrow C_{TS} = \frac{1}{R_{TS}} = 0.62 \frac{\text{LPM}}{\text{bar}} \\ R_{BS} &\cong \frac{1}{C_{BS}} = \frac{1}{C_B} - \frac{1}{C_{BL}} = 2.03 \frac{\text{bar}}{\text{LPM}} \rightarrow C_{BS} = \frac{1}{R_{BS}} = 0.49 \frac{\text{LPM}}{\text{bar}} \end{aligned} \tag{6}$$

The average end seal conductance is $C_{ave-S1} = \frac{C_{TS} + C_{BS}}{2} = 0.56 \ \frac{\text{LPM}}{\text{bar}}$ which is ~6.2% that of the open ends SFD with an identical radial clearance.

The end seal flow conductance ($\bar{C}_{seal-1}$) per unit circumference length is

$$\bar{C}_{seal-1} = \frac{C_{ave-S1}}{\pi D} = 0.234 \ \frac{\text{mm}^3}{\text{s} \cdot \text{Pa} \cdot \text{m}} \tag{7}$$

Similarly, with another pair of piston ring seals, the estimated flow conductance C_{ave-S2}=0.89 LPM/bar, ~60% larger than the flow conductance of the damper sealed with C_{ave-S1}, i.e., C_{ave-S2}=1.6·C_{ave-S1}. See Table 2(c) for details. Note that second pair of piston rings has a larger slit gap than the first pair (dimensions are not specified due to its proprietary design).

Later, sets of tests consist of dynamic load excitations with damper A with the two pairs of piston seals (C_{ave-S1} and C_{ave-S2}), respectively.

Table 2. Feed pressure and lubricant flow rate for (a) three feed holes, (b): <u>open</u> ends and (c)-(d): <u>sealed</u> ends damper A (c_A=0.254 mm). Land length L=25.4 mm, ISO VG 2 oil at room temperature T_S=23°C. <u>P_O estimated based on Eq.(3).</u>

(a) Three feed holes open to ambient (P_O=P_a)

P_{in} (bar(g))	0.07	0.14	0.21	0.28
Q_{in} (LPM)	3.67	5.02	6.15	7.48
Flow conductance		$3C_o$	**30.20**	**LPM/bar**

(b) <u>Open</u> ends SFD (c_A=0.254 mm)

P_{in} (barg)	P_O (barg)	Q_{in} (LPM)	Q_B (LPM)	Ratio Q_B/Q_{in}
0.28	0.12	4.59	2.30	0.50
0.41	0.22	5.84	2.92	0.50
0.69	0.44	7.54	3.95	0.52
0.83	0.55	8.45	4.77	0.56
0.97	0.65	9.40	5.12	0.54
Average				
0.63	**0.40**	**7.16**	**3.81**	**0.53**
Flow Conductance	**Total** $C_{total\text{-}open\text{-}Po}$	**Top Land** $C_{TL\text{-}open\text{-}Po}$	**Bottom Land** $C_{BL\text{-}open\text{-}Po}$	
LPM/bar	**18.02**	**8.43**	**9.59**	

Table 2. Continued.

(c) Sealed ends SFD (c_A=0.254 mm): $C_{ave\text{-}s1}$=0.56 (LPM/bar)

P_{in} (barg)	P_O (barg)	Q_{in} (LPM)	Q_B (LPM)	Ratio Q_B/Q_{in}
0.59	0.57	0.64	0.29	0.46
1.10	1.06	1.25	0.55	0.44
1.38	1.33	1.48	0.64	0.43
1.65	1.60	1.71	0.73	0.43
2.07	2.01	1.78	0.86	0.48
Average				
1.36	**1.31**	**1.37**	**0.62**	**0.45**
Flow Conductance	**Total** $C_{total\text{-}seal}$	**Top Land** $C_{T\text{-}seal\text{-}1}$	**Bottom Land** $C_{B\text{-}seal\text{-}1}$	
LPM/bar	**1.045**	**0.576**	**0.469**	

(d) Sealed ends SFD (c_A=0.254 mm): $C_{ave\text{-}s2}$=0.89 (LPM/bar)

P_{in} (barg)	P_O (barg)	Q_{in} (LPM)	Q_B (LPM)	Ratio Q_B/Q_{in}
0.57	0.54	0.99	0.45	0.45
0.80	0.76	1.25	0.55	0.44
0.92	0.88	1.36	0.61	0.44
Average				
0.77	**0.73**	**1.20**	**0.54**	**0.45**
Flow Conductance	**Total** $C_{total\text{-}seal}$	**Top Land** $C_{T\text{-}seal\text{-}2}$	**Bottom Land** $C_{B\text{-}seal\text{-}2}$	
LPM/bar	**1.654**	**0.916**	**0.738**	

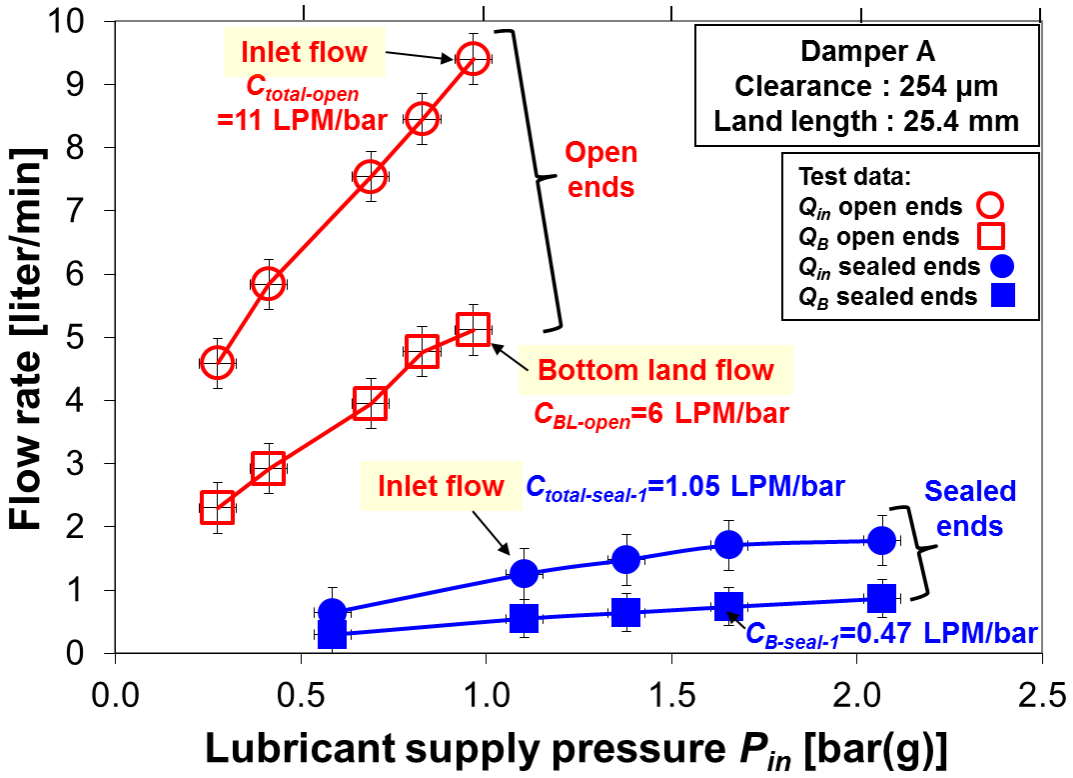

Figure 16. Oil flow rate at inlet (Q_{in}) and through bottom section (Q_B), versus feed hole pressure (P_S) for open and sealed ends SFD (c_A=0.254 mm). P_O estimated based on Eq.(3). Flow conductance labeled.

4. SINGLE FREQUENCY DYNAMIC LOAD TESTS*

4.1. Experimental Procedure

Figure 17 provides (a) a description of the BC kinematics for a whirl orbit motion, (b) the coordinate systems of the BC and a static loader (c) a depiction of various whirl orbits at centered and off-centered conditions. Figure 17(a) depicts the whirl motion of the BC with amplitude components (r_X, r_Y) at a frequency $\omega_{(t)}$. $\bar{e}_s$ and $\bar{e}_{(t)}$ denote the eccentricity vectors from the origin to the BC static position and origin to the orbital path, respectively. As shown in Figure 17(b), the static loader pulls the BC to a static off-centered condition along the $\bar{X}$ axis, 45˚ away from (X,Y).

For whirl orbit motions, the experiments include single-frequency dynamic load excitations. The dynamic load exerted by the shakers in the X and Y directions are

$$\mathbf{F}_{CW} = F\begin{bmatrix}\cos(\omega t)\\ \sin(\omega t)\end{bmatrix};\ \mathbf{F}_{CCW} = F\begin{bmatrix}\cos(\omega t)\\ -\sin(\omega t)\end{bmatrix} \tag{8}$$

where F is the load magnitude and subscripts CW and CCW denote clockwise and counter-clockwise BC motions corresponding to two linearly independent excitations force vectors.

* Reprinted with permission from "Transient Response of a Short-Length (L/D=0.2) Open Ends Elastically Supported Squeeze Film Damper: Centered and Largely Off-Centered Whirl Motions" by San Andrés, L., Den, S., and Jeung, S.-H., 2016, ASME J. Gas Turb. Pwr., 138(12), p.122503, Copyright 2016 by ASME.

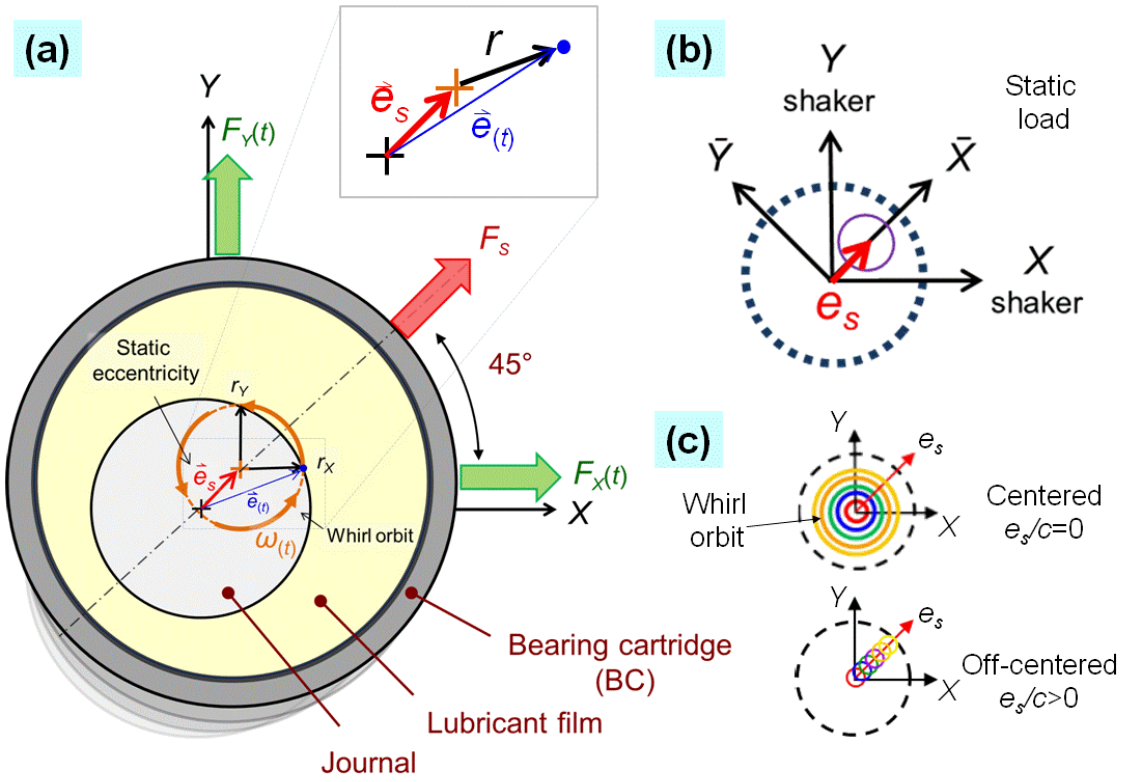

Figure 17. (a) Schematic view of whirl orbit kinematics (Exaggerated film clearance for illustrative purposes), (b) coordinate systems for motion, (c) various orbits with amplitude (*r*) at centered and off-centered conditions (e_s) [9].

The test rig is modeled as a two degree of freedom mechanical system and governed by the following equation of motion in the frequency domain

$$[\mathbf{K}_{\mathrm{L}} - \omega^2 \mathbf{M}_{\mathrm{L}} + i\omega \mathbf{C}_{\mathrm{L}}]\mathbf{Z}_{(\omega)} = \mathbf{F}_{(\omega)} - M_{BC}\mathbf{a}_{(\omega)} \tag{9}$$

where $\mathbf{F}_{(\omega)}$, $\mathbf{Z}_{(\omega)}$, $\mathbf{a}_{(\omega)}$ are vectors of the discrete Fourier transforms of the recorded dynamic load, bearing cartridge (BC) displacement relative to the journal, and BC acceleration, respectively. Above, M_{BC}=15.15 kg is the mass of the BC.

Discrete Fourier transforms of the data obtained from two linearly independent excitation force vectors $\mathbf{F}_{CW}$ and $\mathbf{F}_{CCW}$ produce:

$$\mathbf{F}_{CW} \Rightarrow \begin{Bmatrix} \mathbf{Z}_{CW} \\ \mathbf{a}_{CW} \end{Bmatrix}, \mathbf{F}_{CCW} \Rightarrow \begin{Bmatrix} \mathbf{Z}_{CCW} \\ \mathbf{a}_{CCW} \end{Bmatrix} \tag{10}$$

Then Eq. (9) can be solved for using the recorded data.

$$\mathbf{H}_L = [\mathbf{F}_{CW} - M_{BC}\mathbf{a}_{CW} \;\; \mathbf{F}_{CCW} - M_{BC}\mathbf{a}_{CCW}][\mathbf{Z}_{CW} \;\; \mathbf{Z}_{CCW}]^{-1} \tag{11}$$

To identify the lubricated system force coefficients (**K**, **C**, **M**)$_L$, a complex stiffness matrix is defined as

$$\mathbf{H}_L = [\mathbf{K} - \omega^2\mathbf{M} + i\omega\mathbf{C}]_L \tag{12}$$

where the real part Re($\mathbf{H}_L$) → ($\mathbf{K}_L$-$\omega^2\mathbf{M}_L$) yields the lubricated system stiffness ($\mathbf{K}_L$) and added mass ($\mathbf{M}_L$) coefficients, and the imaginary part Im($\mathbf{H}_L$)→($\omega\mathbf{C}_L$) yields the lubricated system damping coefficients ($\mathbf{C}_L$).

The SFD complex stiffnesses ($\mathbf{H}_{SFD}$) follow by subtracting the dry system complex stiffnesses ($\mathbf{H}_S$), calculated in the same manner, from the lubricated system complex stiffnesses. That is

$$\mathbf{H}_{SFD} = \mathbf{H}_L - \mathbf{H}_S \tag{13}$$

Appendix D details the identification of mechanical parameters (K, C, M)$_S$ for the test dry system. In brief, the estimated structural force coefficients for the dry system (without lubricant in the film land) are K_s=12.0 MN/m, M_s=3.5 kg, and C_s=0.6 kN.s/m. Note that the BC mass M_{BC} =15.15 kg. The estimated damping ratio (ζ) for the dry (no oil) test system is ~2% or less, typical of a steel structure. The dry system natural frequency is $f_n = \sqrt{\frac{K_S}{M_{BC}}}$ =127 Hz.

Table 3 outlines the operating conditions for whirl orbit motions resulting from a single frequency dynamic load. For single-frequency dynamic loads (α=0), the excitation frequency ω is fixed, at intervals of 10 Hz, over the frequency range 10-100 Hz. Note that a sealed ends damper produces much larger reaction forces which reach the load capacity of the shakers (2.2 kN); thus the tests are limited to an excitation frequency (ω) less than 100 Hz.

The static loader, positioned 45° away from the *X* and *Y* directions, pulls the bearing cartridge to a desired static eccentricity e_s ($\bar{X}$ -direction). The shakers exert single frequency forces to produce circular whirl motions of the BC with amplitude *r*. For sealed ends SFD, Dynamic load tests are conducted at static eccentricity (e_s=0.0c_A, 0.25c_A, and 0.50c_A) and with orbit radius r/c_A =0.15, 0.30, 0.45, and 0.60. Note that for the sealed ends SFD, larger orbit radii could not be produced at a high static eccentricity (e_s/c_A >0.5). Ref.[5] details experimental results with single frequency dynamic loads for open ends damper A (c_A=254 μm).

During the tests for sealed damper (with flow conductance C_{ave-S1}) the lubricant supply pressure upstream of the feedholes is maintained at $P_{in\text{-}1}$~0.69 bar(g) and the lubricant flow rate is $Q_{in\text{-}1}$=0.68 LPM. Afterwards, an identical tests is conducted but with ~4 times higher oil supply pressure, $P_{in\text{-}2}$~2.76 bar(g), and the corresponding lubricant flow rate $Q_{in\text{-}2}$=2.71 LPM.

After all the tests are completed with the first sealed ends damper. A second pair of piston rings replaces the first set. Here C_{ave-S2} =0.89 LPM/bar thus allowing more leakage. Note again that the second pair of piston rings makes a larger ring slit (gap)

upon installation than the first pair (dimension proprietary). Note that the lubricant supply pressure is set to P_{in-1}=0.69 barg.

Table 3. Test conditions for open ends SFD and sealed ends SFD for whirl circular orbit motions with a single frequency dynamic load (α=0).

Single frequency dynamic load					
End condition	Whirl amplitude, r/c_A	Static eccentricity, e_s/c_A	Inlet flow rate, Q_{in} (LPM)	Static inlet Pressure, P_{in} (bar(g))	Seal conductance, C_{ave-S} (LPM/bar)
Open ends [5]	r/c_A = 0.15, 0.3, 0.45, 0.6, 0.75	e_s/c_A = 0.0	5.03	P_{in-3}=0.35	-
	r/c_A = 0.15, 0.3, 0.45, 0.6, 0.75	e_s/c_A = 0.15			
	r/c_A = 0.15, 0.3, 0.45, 0.6	e_s/c_A = 0.30			
	r/c_A = 0.15, 0.3, 0.45	e_s/c_A = 0.45			
	r/c_A = 0.15, 0.3	e_s/c_A = 0.60			
	r/c_A = 0.15	e_s/c_A = 0.75			
Sealed ends	r/c_A = 0.15, 0.3, 0.45, 0.6	e_s/c_A = 0.0	2.71	P_{in-2}=2.76	0.56
	r/c_A = 0.15, 0.3, 0.45	e_s/c_A = 0.25			
	r/c_A = 0.15, 0.3	e_s/c_A = 0.5			
	r/c_A = 0.15, 0.3, 0.45, 0.6	e_s/c_A = 0.0	0.68	P_{in-1}=0.69	
	r/c_A = 0.15, 0.3, 0.45	e_s/c_A = 0.25			
	r/c_A = 0.15, 0.3	e_s/c_A = 0.5			
	r/c_A = 0.15, 0.3, 0.45, 0.6, 0.75	e_s/c_A = 0.0	1.07		0.89

*Frequency range: 10 - 100 Hz. Damper clearance c_A=0.254 mm.

4.2. Experimental Results

This section presents experimental results obtained from circular whirl motion of the sealed ends SFD induced by single frequency dynamic loads. Ref.[5] reports in full the operation condition and the experimental results for open ends damper. In summary, for open ends SFD [5], the SFD direct damping coefficients increase both with increasing orbit amplitude (r) and static eccentricity (e_s) while the direct added mass increase dramatically with static eccentricity (e_s) while being less sensitive to the orbit radius r (see later in Figs. 19 and 20).

For sealed ends damper A (c_A=0.254 mm), Figure 18 depicts the real and imaginary parts of the lubricated system direct impedances, H_{XX} and H_{YY}, as well as the corresponding physical model curves for circular orbit tests with orbit radius r/c_A=0.3 and 0.6 at the centered condition e_s=0, and with radius r/c_A=0.3 at the off-centered condition e_s/c_A=0.5.

Note that the test data spans frequency range 10-100 Hz. It is important to state that the identification of parameters considers only the data obtained within the frequency range f_{start}=10 Hz to f_{end}=100 Hz. For the most part, the physical model curve fits show satisfactory correlation factor ($R^2 > 0.95$) indicating its adequacy.

The imaginary part of the system direct impedances shows a constant slope denoting the damping is viscous in character. In addition, the slope increases with an increase in orbit size (r) and in journal static eccentricity (e_s), thus evidencing that C_{XX} and C_{YY} are a function of both r and e_s.

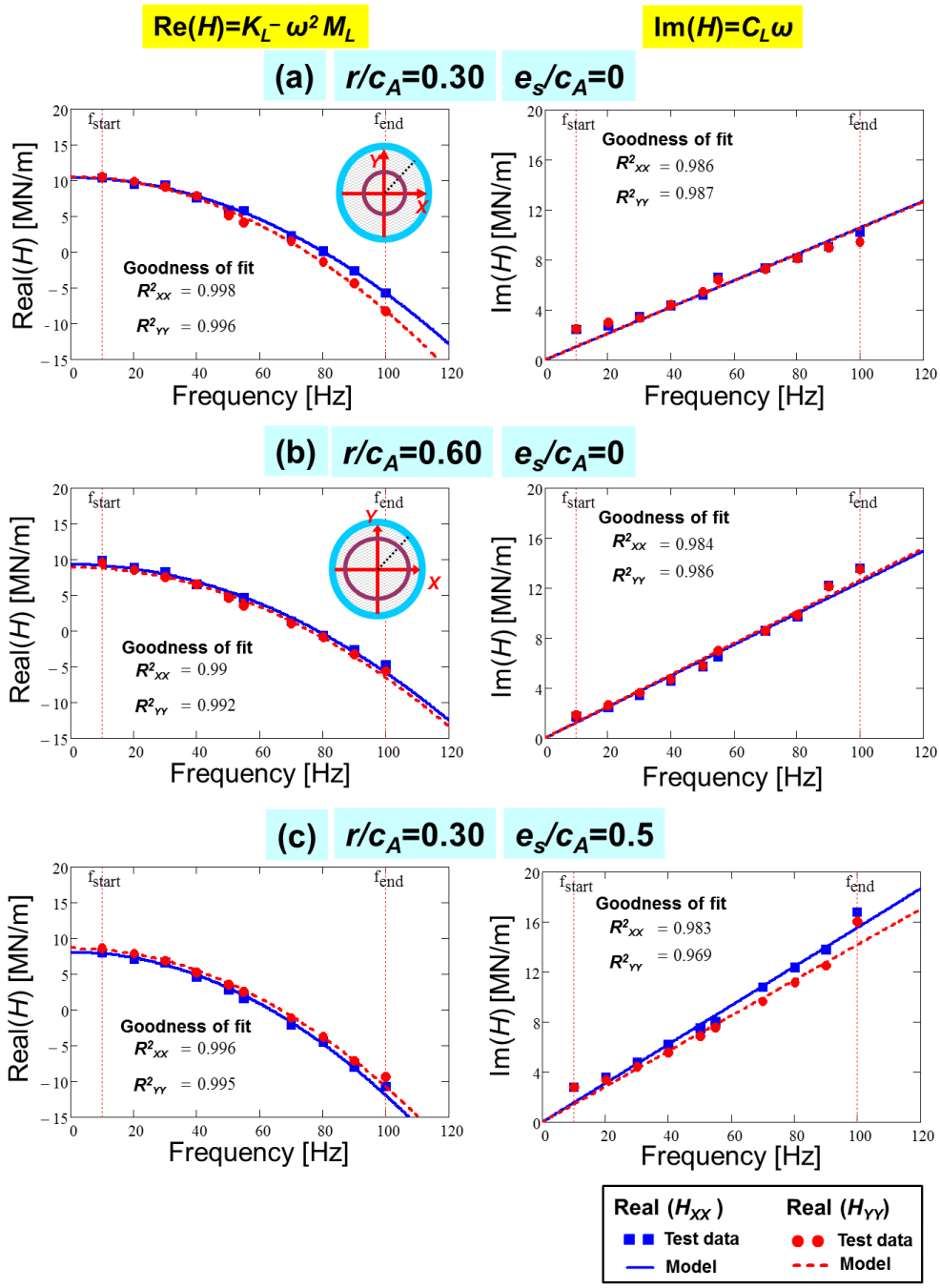

Figure 18. Sealed ends damper A (c_A=0.254 mm): Real and imaginary parts of test system direct complex stiffness (H_{XX}, H_{YY}) versus excitation frequency. Test data and corresponding physical model curve fits. Circular orbits of amplitude (a) r/c_A=0.3 and e_s/c_A=0, (b) r/c_A=0.6 and e_s/c_A=0, (c) r/c_A=0.3 and e_s/c_A=0.5. Lubricant supply pressure $P_{in\text{-}2}$=2.76 bar. Seal conductance $C_{ave\text{-}S1}$=0.56 LPM/bar.

Figures 19 and 20 show surface plots of SFD direct and cross-coupled damping (C), inertia (M) and stiffness ($-K$) coefficients for operating conditions with two lubricant supply pressures $P_{in\text{-}1}$=0.69 bar and $P_{in\text{-}2}$=2.76 bar, respectively. The test data correspond to centered circular orbit tests of increasing orbit amplitude (r/c_A) and at three static eccentricities ($e_s = 0.0c_A$, $0.25c_A$ and $0.50c_A$).

For a sealed ends SFD with oil supply pressure $P_{in\text{-}1}$=0.69 bar in Figure 19, the SFD direct damping coefficients ($C_{A\text{-}XX}$, $C_{A\text{-}YY}$) increase both with increasing orbit radius (r/c_A) and static eccentricity (e_s). In general, the direct and cross-coupled SFD damping coefficients for the X and Y axes are virtually identical ($C_{A\text{-}XX} \sim C_{A\text{-}YY}$, $C_{A\text{-}XY} \sim C_{A\text{-}YX}$) evidencing a high degree of isotropy; hence only the X-axis coefficients are shown for brevity. Cross-coupled damping $C_{A\text{-}XY}$ increases with static eccentricity and reaches ~23% of the direct coefficient one ($C_{A\text{-}XX}$) at e_s/c_A=0.5. However, $C_{A\text{-}XY}$ is insensitive to the orbit amplitude (r).

The SFD direct inertia coefficients ($M_{A\text{-}XX} \sim M_{A\text{-}YY}$) increase with static eccentricity (e_s) while decreasing quickly with orbit amplitude (r/c_A). The cross-coupled coefficient $M_{A\text{-}XY}$ does not show a distinguishable trend with the orbit amplitude (r/c_A), but increases with static eccentricity. For whirl motions departing from e_s/c_A=0.5 with amplitude r/c_A=0.15, the direct inertia $M_{A\text{-}XX}$ is ~22% larger than the $M_{A\text{-}XX}$ for whirl motions departing from e_s/c_A=0 with the same orbit amplitude.

The SFD stiffness coefficients are all negative (softening) and are a fractional amount of the support stiffness ($K_{A\text{-}XX}$ ~0.21 K_S) at e_s/c=0.5. Note that $|K_{A\text{-}XX}|$ grows

linearly with both the static eccentricity (e_s) and orbit amplitude (r) while the cross-coupled stiffness coefficients are infinitesimal at all conditions.

For a higher lubricant supply pressure $P_{in\text{-}2}$=2.76 bar in Figure 20, the SFD direct damping ($C_{A\text{-}XX}$) is more or less constant with increasing orbit radius (r) yet increases with static eccentricity (e_s). Cross-coupled terms ($C_{A\text{-}XY}$) are small compared to the direct ones, albeit increases with e_s and reaches ~20% of $C_{A\text{-}XX}$ at e_s/c=0.5.

The SFD direct and cross-coupled inertia coefficients ($M_{A\text{-}XX}$, $M_{A\text{-}XY}$) show a similar trend. That is, the direct added mass increases with e_s, but shows a constant magnitude with across all r. Cross-coupled inertia increases with static eccentricity and $M_{A\text{-}XY}$ is ~0.11 $M_{A\text{-}XX}$ at e_s/c=0.5. The SFD stiffness coefficient ($K_{A\text{-}XX}$) increases both with e_s and r while $K_{A\text{-}XY}$ is minute over the test range.

Appendix E presents the detailed procedure for the calculation of uncertainty in the SFD force coefficients. In general, the direct damping, added mass and stiffness coefficients have a total uncertainty of U_C<9.2%, U_M<17.4% and U_K<2.3%, respectively. The uncertainties are valid for the identification frequency range 10-100 Hz only.

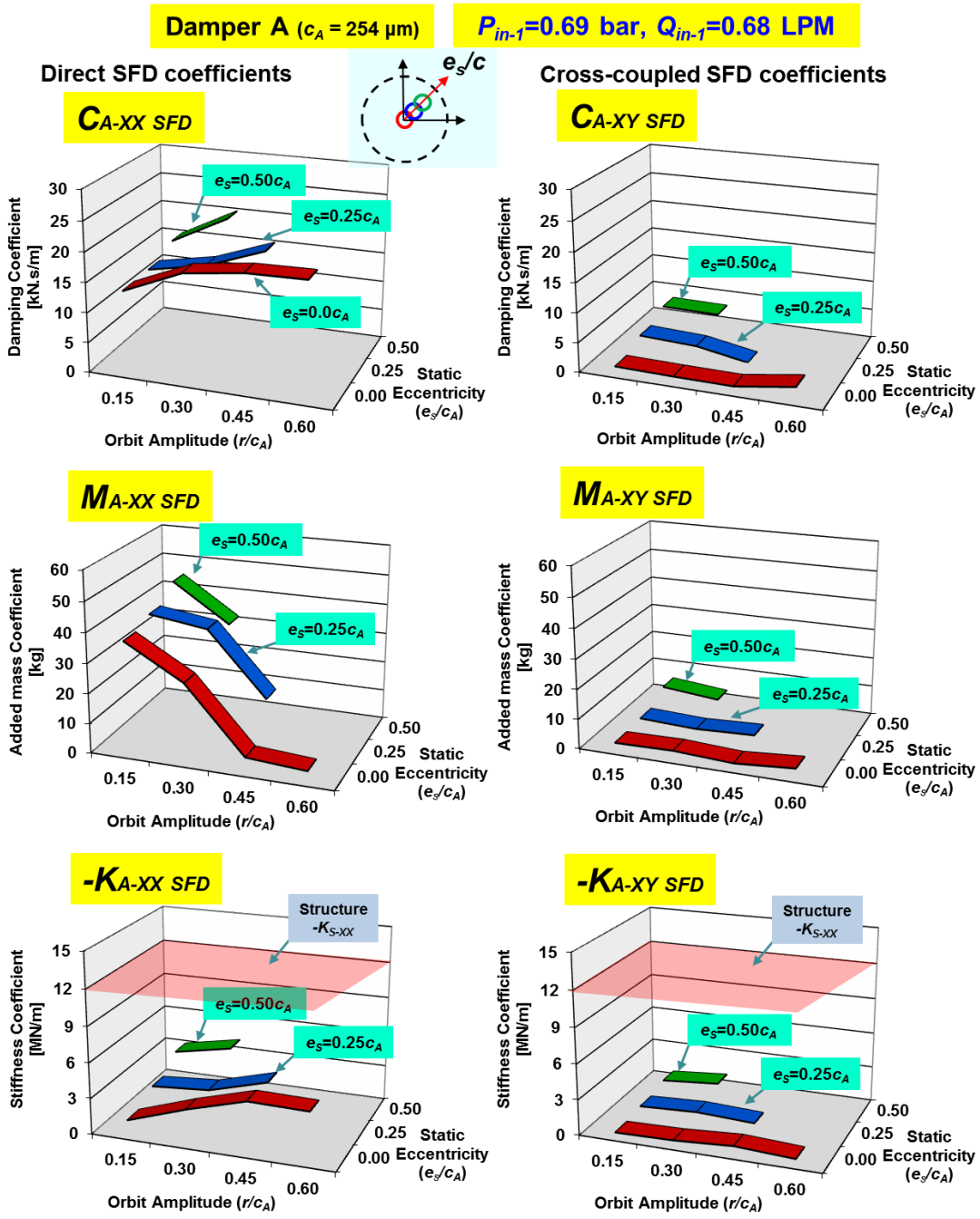

Figure 19. Sealed ends damper A (c_A=254μm) with lubricant supply pressure P_{in-1}=0.69 bar (¼·P_{in-2}). SFD direct and cross-coupled dynamic force coefficients versus orbit amplitude (r/c_A) at three static eccentricities (e_S/c_A=0.0, 0.25, 0.50). Seal conductance C_{ave-S1}=0.56 LPM/bar. Identification frequency range 10–100 Hz.

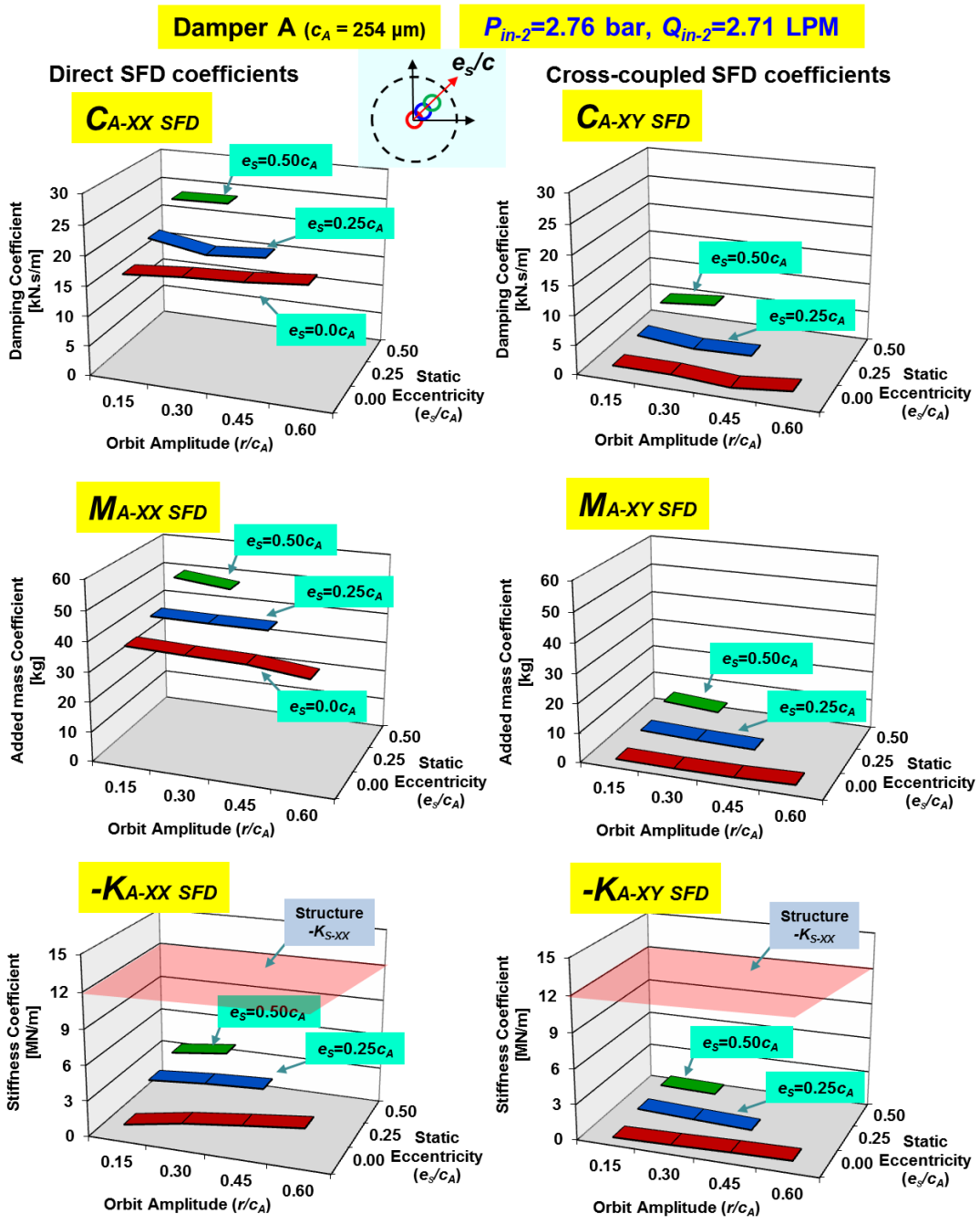

Figure 20. Sealed ends damper A (c_A=254μm) with lubricant supply pressure P_{in-2}=2.76 bar (4·P_{in-1}). SFD direct and cross-coupled dynamic force coefficients versus orbit amplitude (r/c_A) at three static eccentricities (e_s/c_A=0.0, 0.25, 0.50). Seal conductance C_{ave-S1}=0.56 LPM/bar. Identification frequency range 10–100 Hz.

4.2.1. Effect of Lubricant Supply Pressure on Sealed Ends SFD Force Coefficients

Figure 21 depicts the experimental SFD direct damping $(C_{XX}, C_{YY})_{SFD}$ and added mass $(M_{XX}, M_{YY})_{SFD}$ coefficients for the sealed ends SFD supplied with lubricant at P_{in-1}~0.69 barg (Q_{in-1}=0.68 LPM) and P_{in-2}~2.76 barg (Q_{in-2}=2.68 LPM). The test data correspond to centered circular orbit tests (e_S/c_A = 0.0) with orbit radii r = 0.15c_A-0.60c_A. Note that the end seals flow conductance is C_{ave-S1}=0.56 LPM/bar.

For a small whirl amplitude motion r = 0.15c_A, the direct damping $(C_{XX}, C_{YY})_{SFD}$ obtained with a large oil supply pressure P_{in-2}~2.76 barg is ~26% larger in magnitude than those coefficients obtained with a smaller P_{in-1}~0.69 barg. Note that the difference (~26%) is out of the uncertainty range of damping coefficients ~18.4% ($2\times U_C$). For two sets of supply pressure, P_{in-1} and P_{in-2}, and $r \leq 0.15c_A$, the direct damping coefficients should have shown a similar magnitude. This is because, at a small $r \leq 0.15c_A$ and $\omega \leq$ 100 Hz, oil cavitation most likely does not occur (see later in Figure 32). The difference of ~26% may be due to a dry friction arising from the seal for operation at larger supply pressure P_{in-2}.

With an increase in amplitude motion (r), $C_{XX(Pin-1)}$ and $C_{XX(Pin-2)}$ show an opposite trend; $C_{XX(Pin-1)}$ increases rapidly and then tends to plateau, while $C_{XX(Pin-2)}$ shows a constant magnitude. For a low oil supply pressure P_{in-1}~0.69 barg, the inertia coefficients (M_{XX}, M_{YY}) decrease quickly with orbit amplitude whereas the damper with a higher P_{in-2} decrease slightly with orbit size r. This difference in trends may be attributed to the larger lubricant supply pressure (P_{in-2}>P_{in-1}) that leads to a larger generation of dynamic pressure. See later section 4.2.4 for a more detailed discussion.

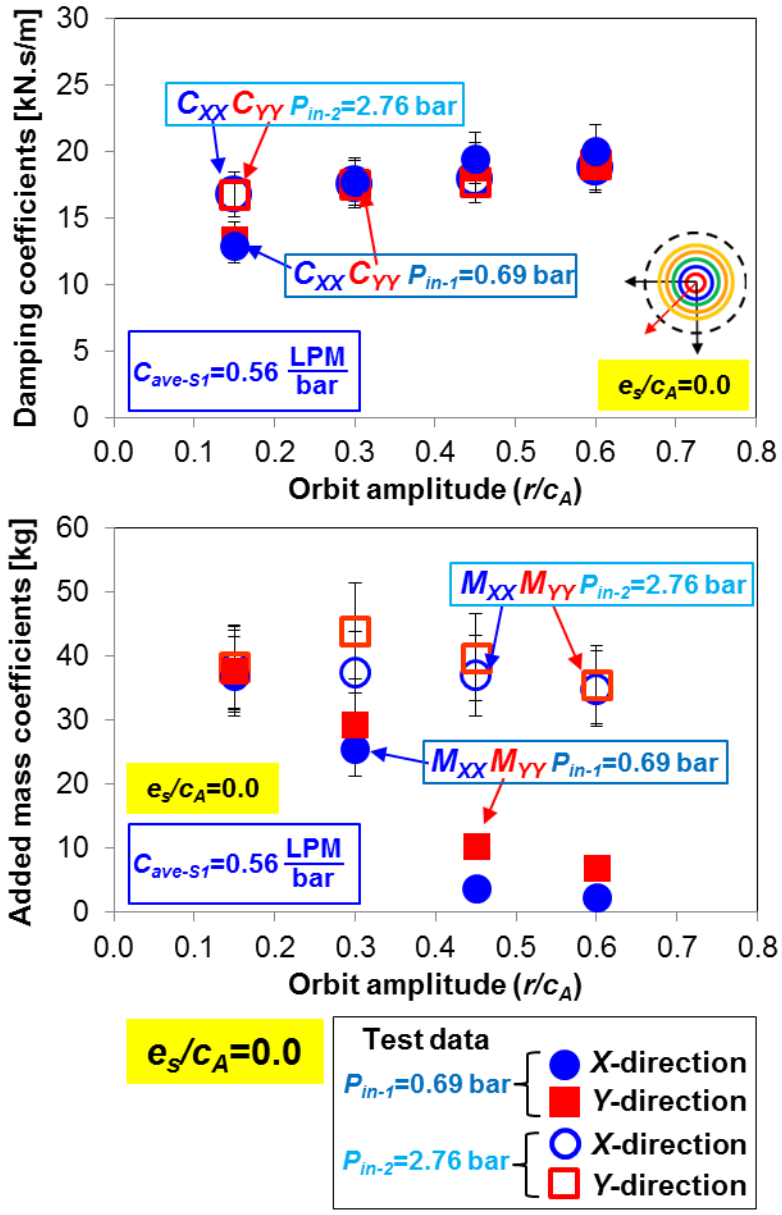

Figure 21. Effect of lubricant supply pressure: sealed ends SFD direct damping (C)$_{SFD}$ and added mass (M)$_{SFD}$ force coefficients versus whirl orbit amplitude (r/c_A) at journal centered condition (e_s/c_A=0.0). Lubricant supply pressure $P_{in\text{-}1}$=0.69 bar and $P_{in\text{-}2}$=2.76 bar. Seal conductance $C_{ave\text{-}S1}$=0.56 LPM/bar. Identification frequency range 10–100 Hz.

Figure 22 shows the identified direct damping $(C)_{SFD}$ and inertia $(M)_{SFD}$ coefficients for the SFD supplied with lubricant at two supply pressures. The coefficients are identified from whirl orbits with amplitude r/c_A=0.15 and for increase in static eccentricity e_s/c_A = 0.0-0.5. The damping coefficients increase with static eccentricity (e_s). The sealed ends damper operating with higher supply pressure (P_{in-2}) provides ~26% - 50% larger damping coefficients than those with lower supply pressure (P_{in-1}). The difference in magnitude becomes larger with an increase in static eccentricity (e_s). The inertia force coefficients for both conditions, P_{in-1} and P_{in-2}, overlap onto each other; albeit $M_{YY(Pin-2)}$ is ~10% larger than at e_s/c_A=0.5. The difference of the added mass coefficients $M_{YY(Pin-1)}$ and $M_{YY(Pin-2)}$ is not as glaring as those from the damping coefficients. This is perhaps due to the uncertainty of the measurement. Recall that the direct added mass coefficient has a total uncertainty of and U_M<17.4% while the uncertainty of the damping coefficient is U_C<9.2%.

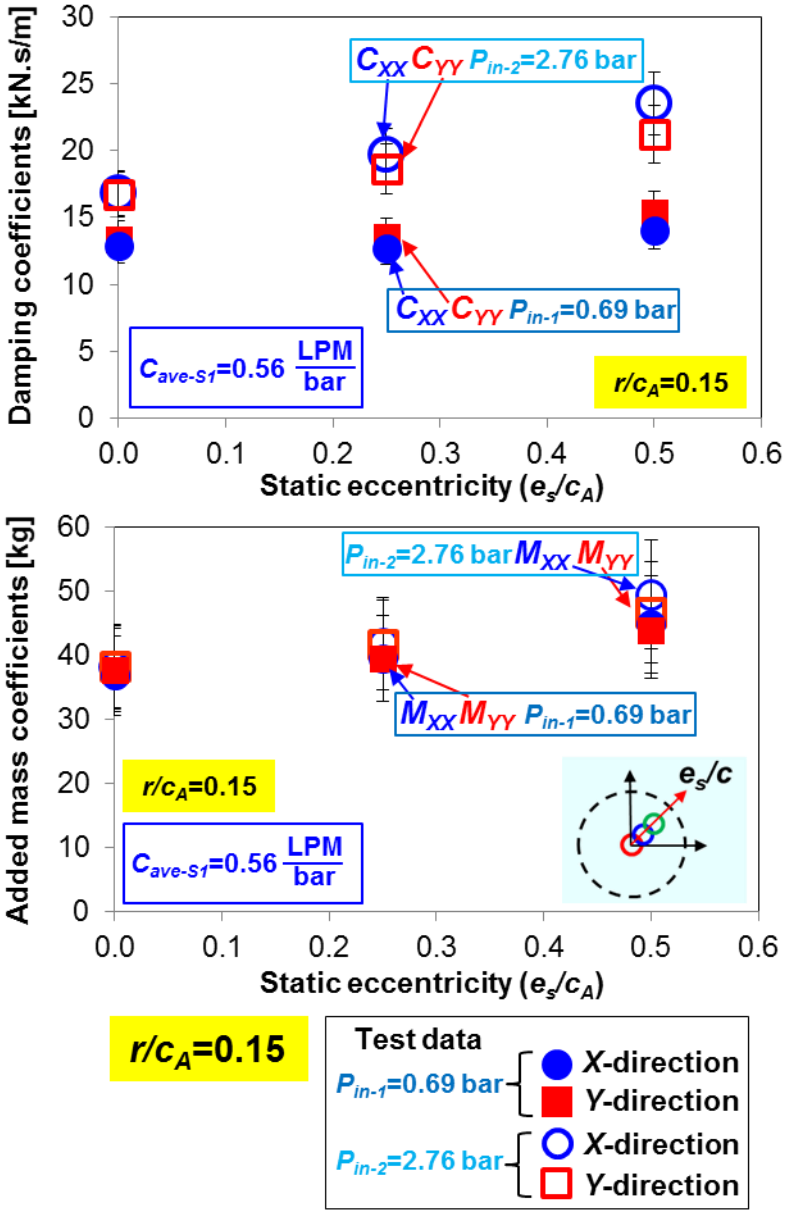

Figure 22. Effect of lubricant supply pressure: sealed ends SFD direct damping (C)$_{SFD}$ and added mass (M)$_{SFD}$ force coefficients versus static eccentricity (e_s/c_A) at whirl orbit amplitude (r/c_A=0.15). Lubricant supply pressure P_{in-1}=0.69 bar and P_{in-2}=2.76 bar. Seal conductance C_{ave-S1}=0.56 LPM/bar. Identification frequency range 10–100 Hz.

4.2.2. Effect of Flow Conductance on Sealed Ends SFD Force Coefficients

Figure 23 depicts the experimental direct damping (C_{XX}, C_{YY})$_{SFD}$ and inertia (M_{XX}, M_{YY})$_{SFD}$ for sealed ends SFDs operating with lubricant inlet pressure $P_{in\text{-}1}$~0.69 barg. There are two ends seals configurations, one with a seal flow conductance C_{ave-S1}=0.56 LPM/bar, and the other with C_{ave-S2}=0.89 LPM/bar. Recall that the two pairs of PRs provide two distinct seal conductances C_{ave-S1} and C_{ave-S2} (Table 2). The second damper leaks 60% more than the damper with C_{ave-S1}, i.e., $\frac{C_{ave-S2}}{C_{ave-S1}}$=1.6. The test data correspond to motions with whirl orbit amplitude r=0.15c_A to 0.60c_A at a journal centered condition (e_S/c_A=0.0).

The direct damping coefficients (C)$_{SFD}$ obtained for both configurations (C_{ave-S1} and C_{ave-S2}) increase mildly with orbit amplitude motion (r). However, in general, the damping coefficients with the lower flow conductance C_{ave-S1} (tighter seal) increase more with an increase in whirl amplitude (r/c_A); and eventually showing ~20% larger damping for motions with orbit amplitude r/c_A=0.6. Note that for small amplitude whirl motions (r/c_A<0.15), both damping coefficients ($C_{XX-C_{ave-S1}}$ and $C_{XX-C_{ave-S2}}$) are equal within the uncertainty range (U_C~9.2%). For the seal ends damper with C_{ave-s} < 1 LPM/bar ($\overline{C}_{seal-1}$, $\overline{C}_{seal-2}$), both damping and inertia coefficients do not increase significantly (later see predictions in Figure 36).

For a damper with either flow conductance, the SFD inertia coefficients decrease with an increase in whirl amplitude motion (r). For a small amplitude of whirl motion

($r/c_A \leq 0.3$), the added mass $(M)_{SFD}$ for the damper with a higher flow resistance (C_{ave-S1}) shows ~12% - 30% larger magnitude than those coefficients for the damper with a smaller flow resistance (C_{ave-S2}). For a damper with either flow conductance ($\bar{C}_{seal-1}$, $\bar{C}_{seal-2}$), both added masses reach close a negligible magnitude ($M_{SFD} \rightarrow 0$) as the orbit amplitude increases to $r/c_A > 0.3$.

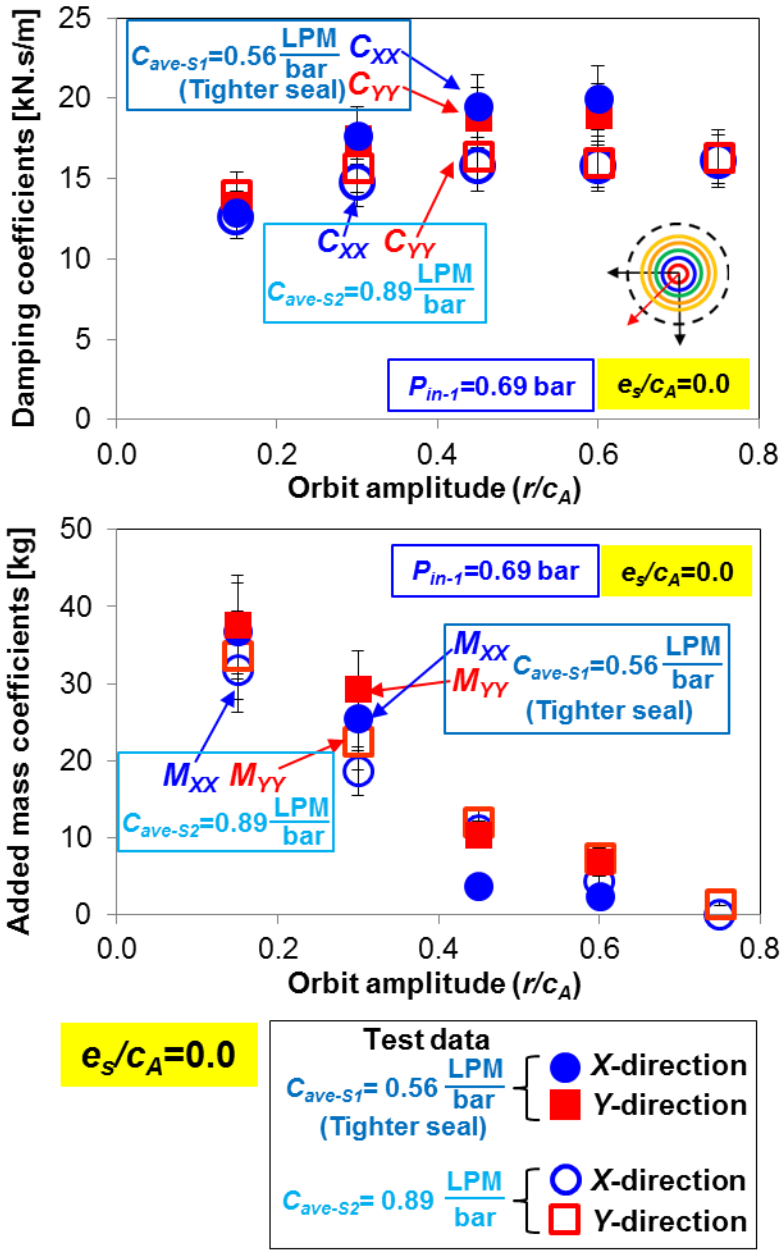

Figure 23. Effect of flow conductance: sealed ends SFD direct damping $(C)_{SFD}$ and added mass $(M)_{SFD}$ force coefficients versus whirl orbit amplitude (r/c_A) at journal centered condition (e_s/c_A=0.0). Lubricant supply pressure $P_{in\text{-}1}$=0.69 bar. Seal conductances $C_{ave\text{-}S1}$=0.56 LPM/bar and $C_{ave\text{-}S2}$=0.89 LPM/bar. Identification frequency range 10–100 Hz.

4.2.3. Comparison of Experimental Force Coefficients for an Open Ends SFD and a Sealed Ends SFD

Table 4 (reproduced from Table 3 for convenience) lists the geometry and the operating conditions for both open ends and sealed ends SFDs. The damper configurations have identical radial clearance c_A=0.254 mm and axial film length L =25.4 mm. Without the piston rings in place, the open ends damper has a total wetted length L_{tot}=36.83 mm (including end lips and chamfered edges (See Figure 12)) and an effective film length[2] L_{eff}=29.7 mm [5]. The oil feed pressure is set at $P_{in\text{-}3}$~0.35 barg (5 psig) and $P_{in\text{-}1}$~0.69 barg (10 psig) for operation with open ends and sealed ends, respectively. The corresponding flow rates (Q_{in}) are 5.03 LPM and 0.68 LPM. Note the significant drop in flow rate (Q_{in}) when the film land ends are sealed with the piston rings. The lubricant inlet flow rate (Q_{in}) and pressure (P_{in}) are chosen to be comparable with those in prior work [3].

Table 4. Open ends and sealed ends SFD configurations and operating conditions

Parameter	Open ends [5]	Sealed ends
Radial clearance	254 μm	
Land length	L_{eff}=29.7 mm*	L=25.4 mm
Static inlet pressure, P_{in}	$P_{in\text{-}3}$=0.35 bar(g)	$P_{in\text{-}1}$=0.69 bar(g)
Inlet flow rate, Q_{in}	5.03 LPM	0.68 LPM

*Denotes the effective film land length (L_{eff})

Figures 24 and 25 show the SFD force coefficients (C_{SFD}, M_{SFD}) obtained for both the sealed ends and the open ends condition versus orbit amplitude (r/c_A) and static

[2] See footnote 1.

eccentricity (e_s). The test data for the open ends SFD is taken from Ref. [5]. Refer to the author's work in [5] for detailed experimental results obtained with the open ends damper A. The inset in Figures 24 and 25 depicts cross-section views of the two dampers.

Both the sealed ends and open ends dampers show an increase in damping coefficient with an increase in whirl amplitude (r) as well as an increase in static eccentricity (e_s). The sealed ends SFD shows, not surprisingly, eleven to thirteen times more damping than the open ends configuration. This is because the end seals restrict the flow of the squeezed lubricant and thus generate a large hydrodynamic pressure in the film land. A detailed comparison of recorded dynamic film pressures for the sealed ends and the open ends dampers follows.

The sealed ends damper also provides nearly eleven times more mass (inertia) coefficients than those coefficients for the open ends. The magnitude is larger than M_{BC}=15.2 kg. The significant increase in added mass coefficient is an important consideration as it will affect the placement of rotor-bearing system critical speeds. Nonetheless, for motions around a journal centered conditions (e_s=0), the sealed ends SFD added mass coefficients decrease with an increase in orbit amplitude (r), and eventually reach the magnitude found for the open ends damper M_{SFD}~3kg. Note all force coefficients shown in the figure are identified with a frequency range ω=10-100 Hz.

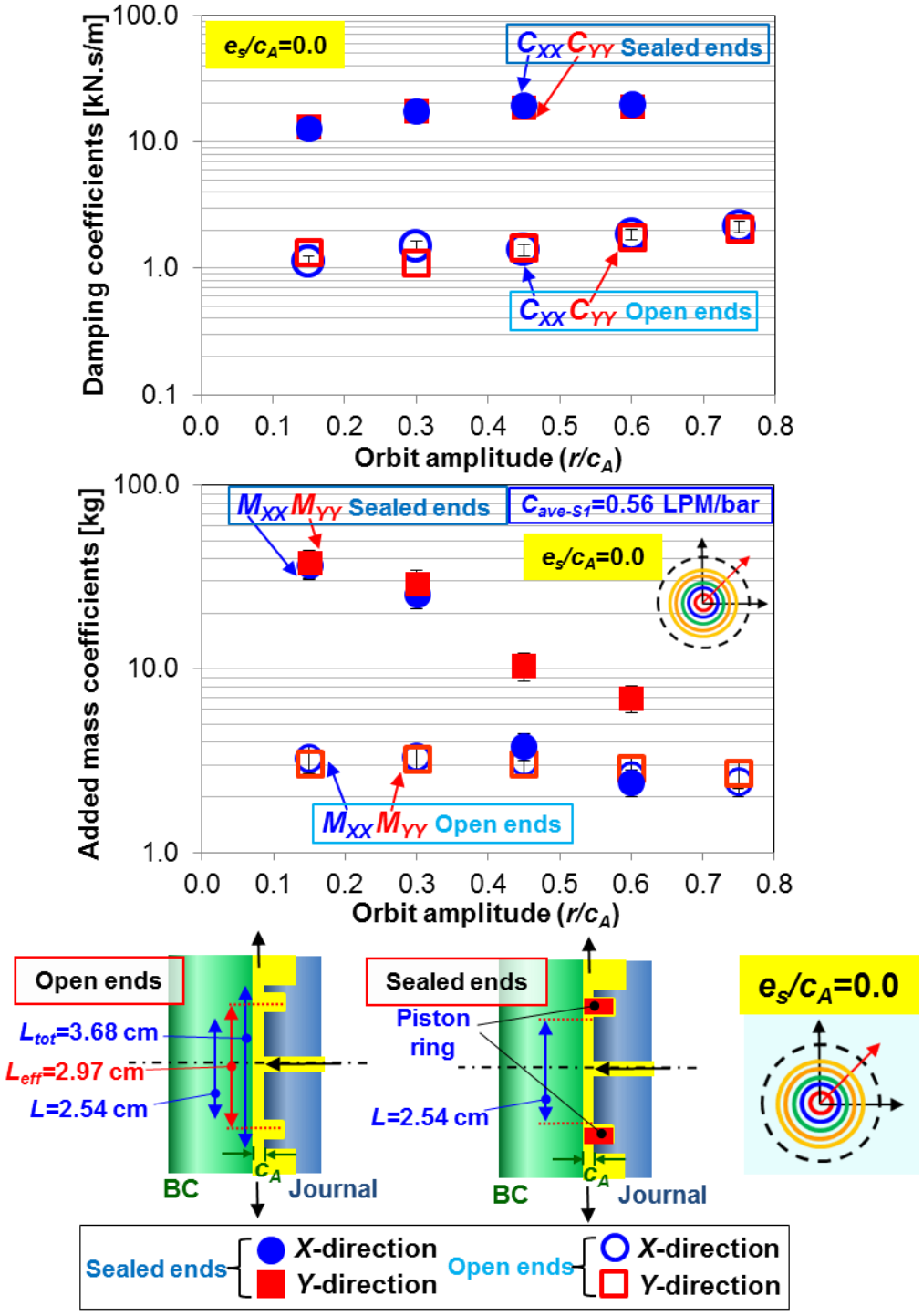

Figure 24. Sealed ends SFD vs Open ends SFD [5]: direct damping $(C)_{SFD}$ and added mass $(M)_{SFD}$ force coefficients versus whirl orbit amplitude (r/c_A) at journal centered condition (e_s/c_A=0.0). Seal conductance C_{ave-S1}=0.56 LPM/bar. Identification frequency range 10–100 Hz.

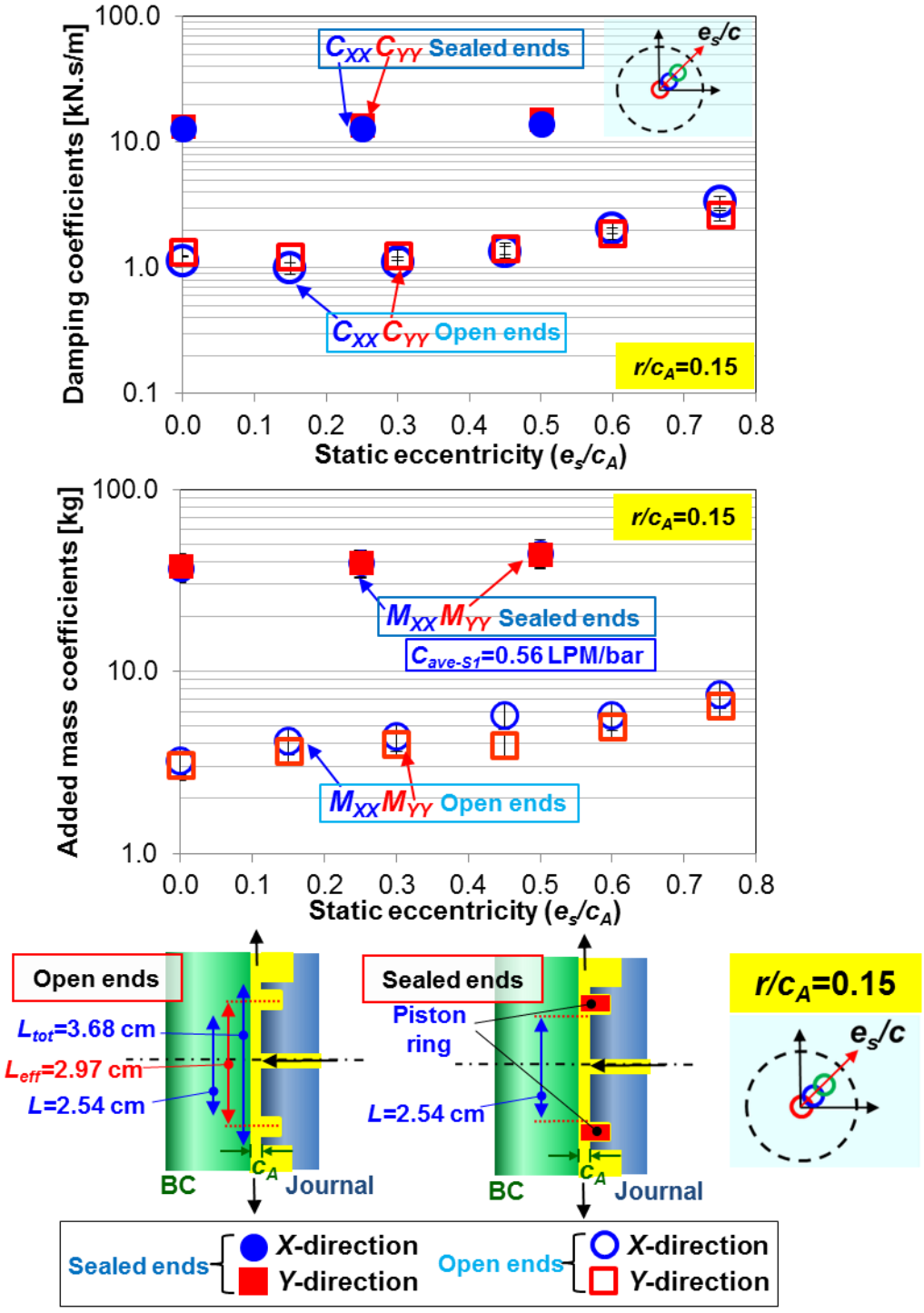

Figure 25. Sealed ends SFD vs Open ends SFD [5]: direct damping $(C)_{SFD}$ and added mass $(M)_{SFD}$ force coefficients versus static eccentricity (e_s/c_A) at whirl orbit amplitude (r/c_A=0.15). Seal conductance C_{ave-S1}=0.56 LPM/bar. Identification frequency range 10–100 Hz.

4.2.4. Comparison of Recorded Film Pressures in an Open Ends SFD and a Sealed Ends SFD

Figure 26 shows the position of pressure sensors in the bearing cartridge (BC). Eight piezoelectric dynamic pressure sensors ($P_1 - P_8$) are installed in the BC around its circumference. Two sets of three pressure sensors ($P_{1\text{-}3} - P_{4\text{-}6}$), spaced apart by 90º, record the dynamic pressure at the top, bottom and mid sections of the damper land as shown in the figure. Note that $P_{1\text{-}2\text{-}3}$ and $P_{4\text{-}5\text{-}6}$ are spaced 15º apart. Two other piezoelectric pressure sensors (P_7 and P_8) measure the film dynamic pressures in the end grooves at the exit of the squeeze film land.

This section presents an analysis of the film dynamic pressures as a function of the amplitude (r) and whirl frequency (ω) of the test damper. Ref. [5] give further details on the film dynamic pressure measurement as a function of amplitude (r) and whirl frequency (ω). The following figures depict the *peak-to-peak* (*p-p*) dynamic film pressures for the sealed ends damper and the open ends damper configurations.

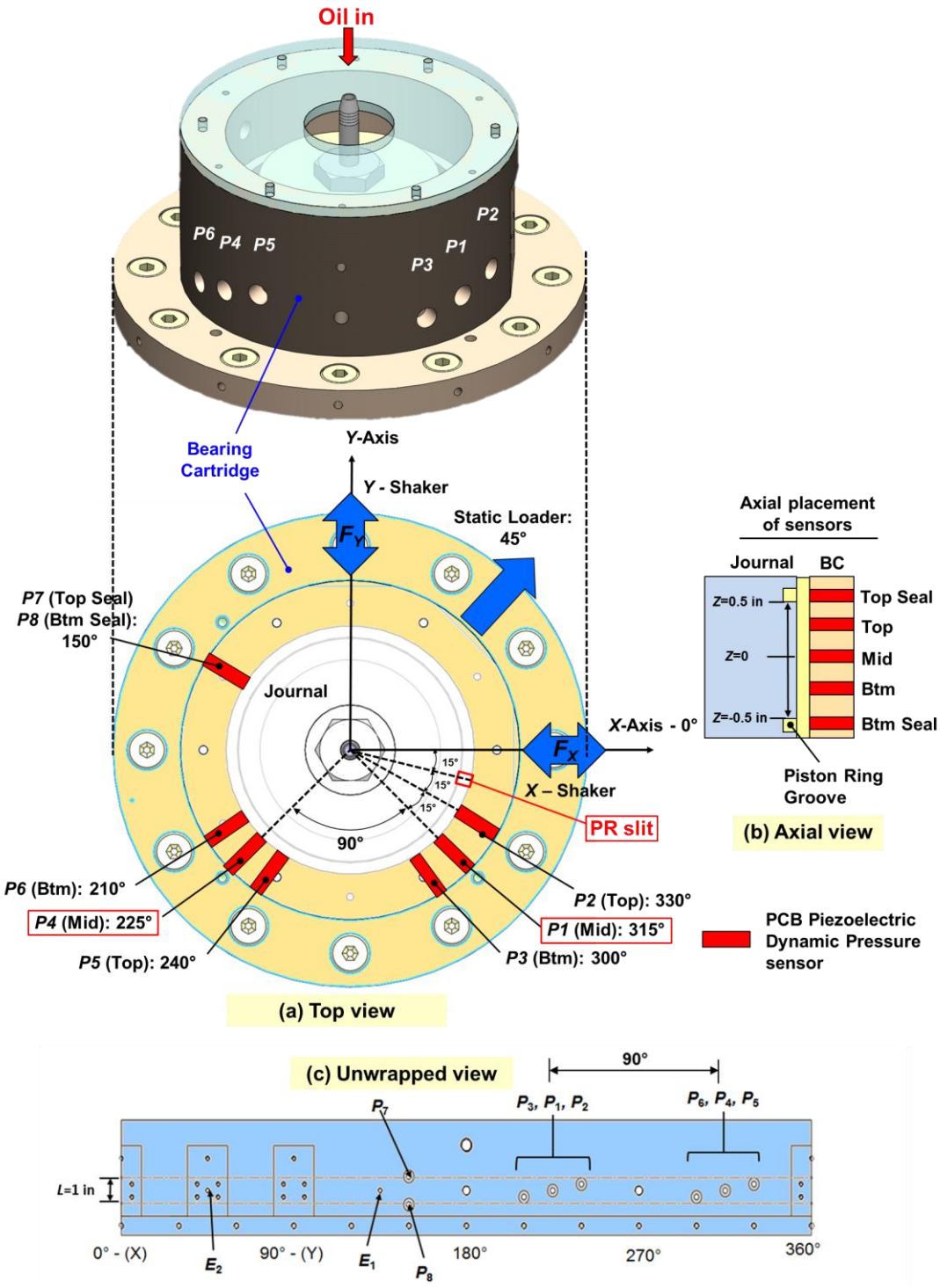

Figure 26. Schematic views of the disposition of pressure sensors in the BC: (a) top view, (b) axial view and (c) unwrapped view [5].

Figure 27 shows the *p-p* (peak to peak) film dynamic pressures recorded at the top (z=½ L), bottom (z=-½ L), and mid plane (z=0) versus whirl frequency (ω). The data corresponds to circular centered orbits with an amplitude of r/c_A=0.15 (e_s=0). For the ends sealed damper, the dynamic pressures are recorded to a maximum excitation frequency (ω)=100 Hz. This frequency is lower than the maximum frequency of 250 Hz for the open ends dampers. Since the sealed ends SFD produces much larger reaction forces which reach the load capacity of the excitation shakers, tests could only be conducted for ω<100 Hz. Figure 27(c) shows the ratio of peak-peak dynamic pressures ($\frac{p_{sealed\ ends}}{p_{open\ ends}}$). Note the difference in horizontal axis scales in Fig. 27(a,b) and (c). Note that the maximum squeeze film velocities ($\omega \times r$) for r/c_A=0.15 at 100 Hz and 250 Hz are 2.4 cm/s and 6.0 cm/s, respectively.

Recall that, for the open ends SFD and sealed ends SFD, the lubricant supply pressure upstream of the feed holes is maintained at $P_{in\text{-}3}$~0.35 barg and $P_{in\text{-}1}$~0.69 barg, respectively. The supplied oil flow rate, measured by a turbine flow meter, (Q_{in}) equals 5.03 LPM for the open ends damper and 0.68 LPM for the sealed ends damper.

For both configurations, an increase in whirl frequency produces an increase in *p-p* dynamic film pressure. Dynamic *p-p* pressures for the sealed ends damper are roughly ten to fifteen times higher than the *p-p* pressures for the open ends damper, in particular for ω > 50 Hz (see Figure 27(c)). Moreover, the disparity in *p-p* dynamic pressures between the sealed and open ends damper increases with whirl frequency. The comparison demonstrates that the piston ring seals, by restricting the axial flow,

effectively increase the generation of dynamic pressures in the film land. Notice that for an open ends condition, the film pressures at the end grooves ($z=\pm½L$) are not nil, they are ~20% of the *p-p* pressures at the mid-plane. Expectedly, the top and bottom film pressures ($z=\pm12.7$ mm (±0.25 in.)) are similar in magnitude; and at the mid-plane ($z=0$ mm), the pressures P_1 and P_4 are also similar in magnitude. Ref. [5] details the measurement of dynamic pressure at the end grooves in an open ends SFD.

Figure 28 shows the peak-to-peak dynamic film pressure at the top ($z=½\ L$), bottom ($z=-½\ L$), and mid plane ($z=0$) versus whirl frequency (ω) for the sealed ends damper supplied with a higher lubricant pressure $P_{in-2}=2.76$ bar. The data corresponds to circular centered orbits with an amplitude of $r/c_A=0.15$ ($e_s=0$). An increase in frequency (ω) results in an increase in *p-p* pressure. The *p-p* pressures from operation with the two oil supply pressures $P_{in-1}=0.69$ bar (Fig.27 (b)) and 2.76 bar (Fig.28) are similar in magnitude.

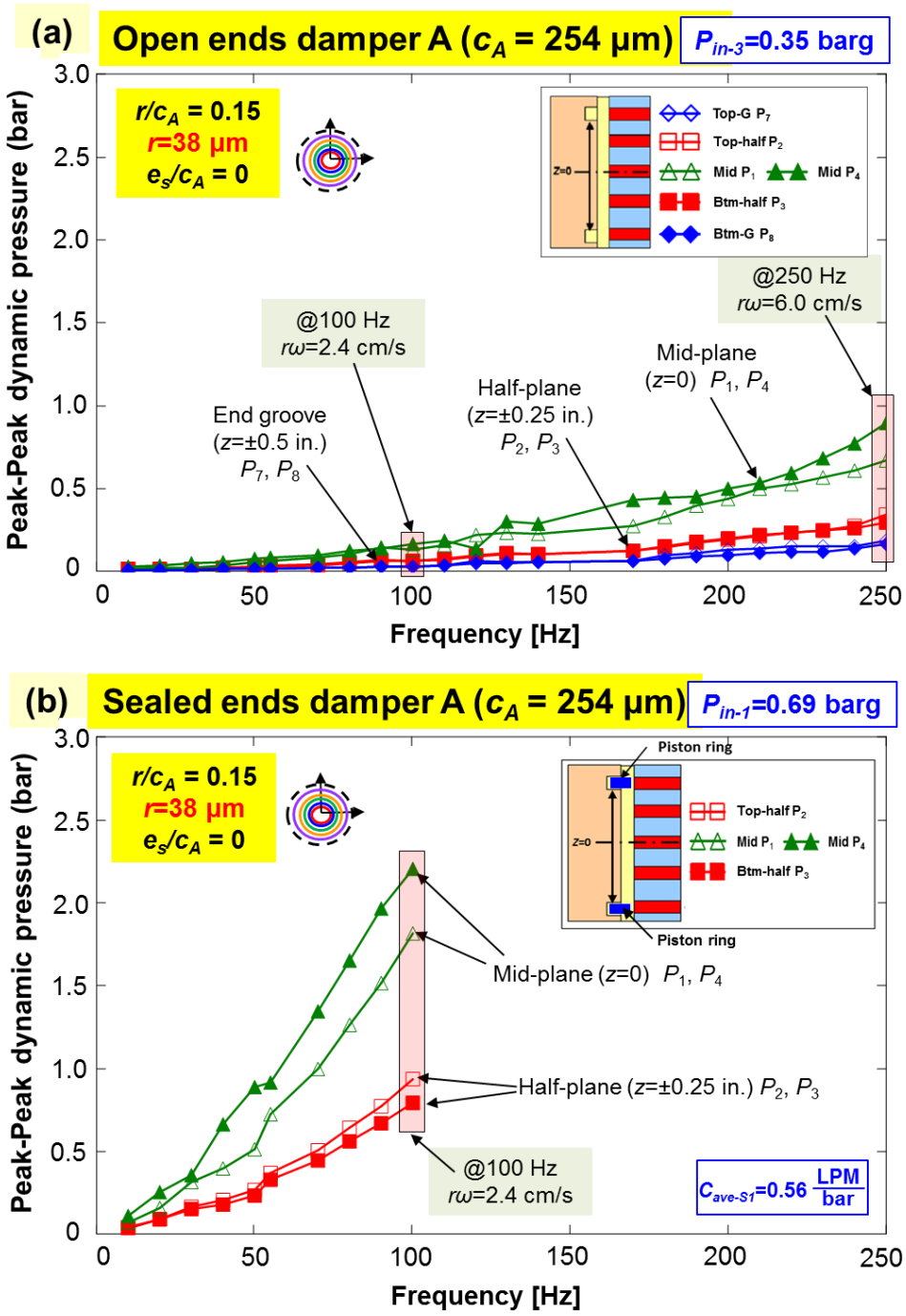

Figure 27. Recorded *peak-to-peak* film dynamic pressures versus excitation frequency (ω) for (a) open ends damper A, (b) sealed ends damper A, and (c) ratio of *p-p* dynamic pressure, P_{sealed}/P_{open}. Circled pressures indicate high whirl frequency ω>60Hz. Centered (e_s=0) circular orbit tests with radius r/c_A=0.15. Measurements at damper mid-plane, top and bottom (half-planes) and end grooves. (Inset shows location of pressure sensors).

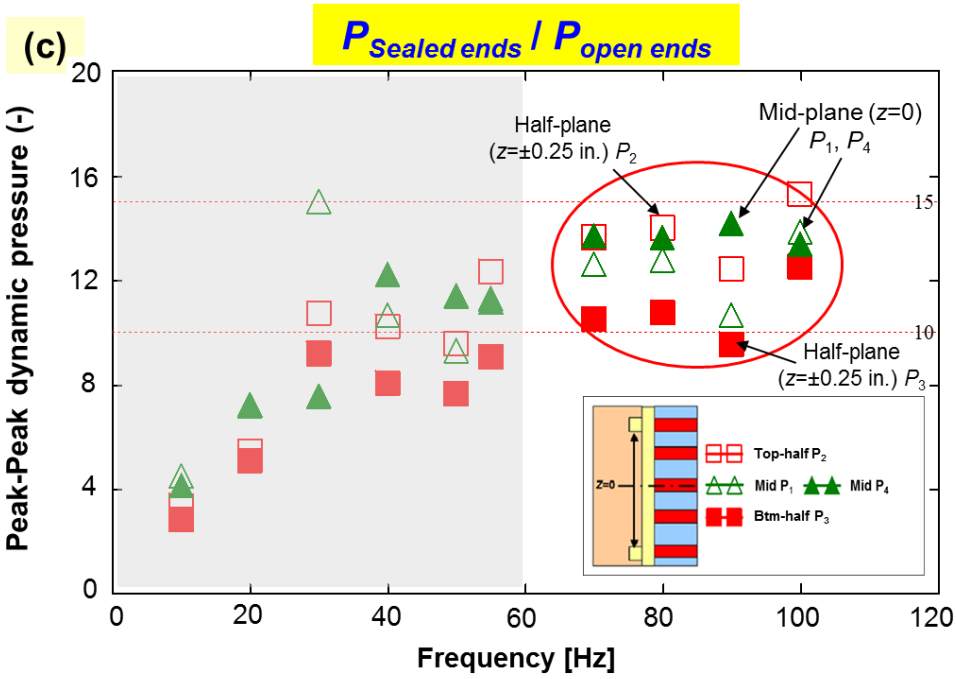

Figure 27. Continued.

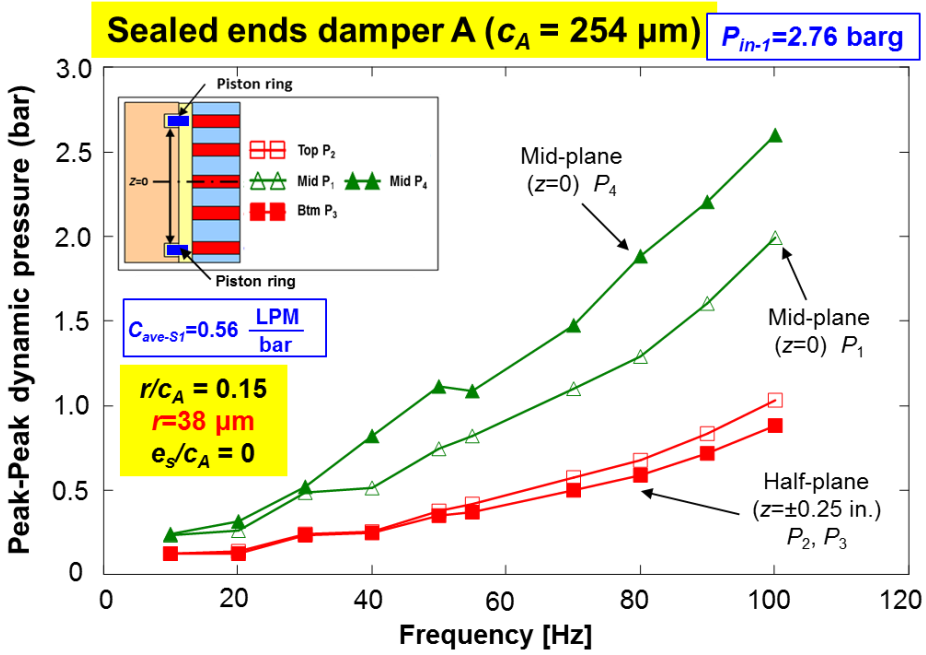

Figure 28. Sealed ends damper A: Recorded *peak-to-peak* film dynamic pressures versus excitation frequency (ω). Centered (e_s=0) circular orbit tests with radius r/c_A=0.15. Measurements at damper mid-plane, top and bottom (half-planes) and end grooves. (Inset shows location of pressure sensors).

For the damper operating with either supply pressure ($P_{in\text{-}1}$ and $P_{in\text{-}2}$) undergoing circular centered orbits (e_s=0), Figure 29 shows the *p-p* dynamic pressures recorded at the mid-plane (z=0) versus whirl frequency (ω) as well as orbit radius (r). Expectedly, increasing the orbit radius produces an increase in *peak-peak* fluid film pressure. For small to moderate orbit radii $r/c_A \leq 0.30$, the *p-p* pressures for the sealed ends SFD with both $P_{in\text{-}1}$ and $P_{in\text{-}2}$ are similar in magnitude. However, for moderate to large amplitude motion $r/c_A \geq 0.45$ and at high whirl frequency ω > 60 Hz, the sealed ends damper supplied with large pressure $P_{in\text{-}2}$ provides ~25% higher *p-p* pressures than those for the damper operating with $P_{in\text{-}1}$.

Figure 30 reveals the ratio of the peak-peak dynamic pressures for the two lubricant supply pressures ($\frac{p_{sealed} : P_{in-2} = 2.76\,\text{bar}}{p_{sealed} : P_{in-1} = 0.69\,\text{bar}}$). The data corresponds to circular centered orbits (e_s=0) with an amplitude of r/c_A = 0.60. In general, the sealed ends damper supplied with a large pressure $P_{in\text{-}2}$ = 2.76 bar generates ~20% larger *p-p* dynamic film pressure that those pressures obtained for operation with a lower lubricant supply pressure $P_{in\text{-}1}$ = 0.69 bar. The ratio of *p-p* pressures tends to increase with whirl frequency, in particular for ω > 60 Hz[3]. This is attributed to a large supply pressure delays the onset of air ingestion and oil cavitation in the film land.

Appendix E details the uncertainty of the *p-p* dynamic pressure U_P~12%. In brief, the uncertainty increases with increase in fluctuation of the *p-p* pressure at high whirl frequency (ω) and large amplitude motion (r) due to air ingestion and oil cavitation.

[3] Note that for low whirl frequency ω < 50 Hz, the *p-p* dynamic pressure is small compared to those obtained at high whirl frequency ω > 60 Hz, but still shows *p-p* ratio ($P_{in\text{-}2}/P_{in\text{-}1}$)~1.

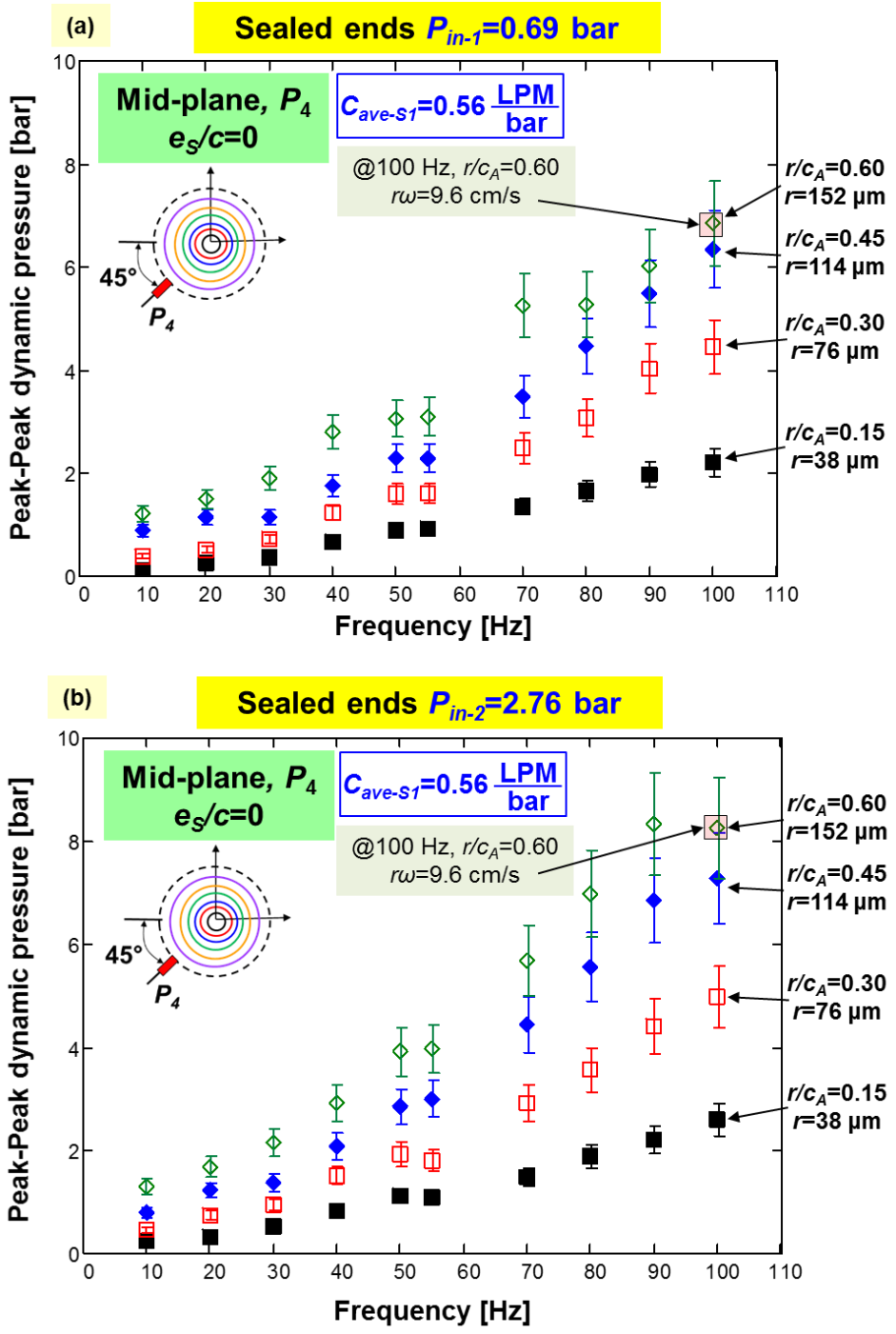

Figure 29. Sealed ends damper A: Measured film *peak-peak* pressures (P_4) at mid-plane (z=0) versus whirl frequency (ω) for increasing orbit radii (r): Lubricant supply pressure (a) P_{in-1}=0.69 bar and (b) P_{in-2}=2.76 bar. Centered condition (e_S=0).

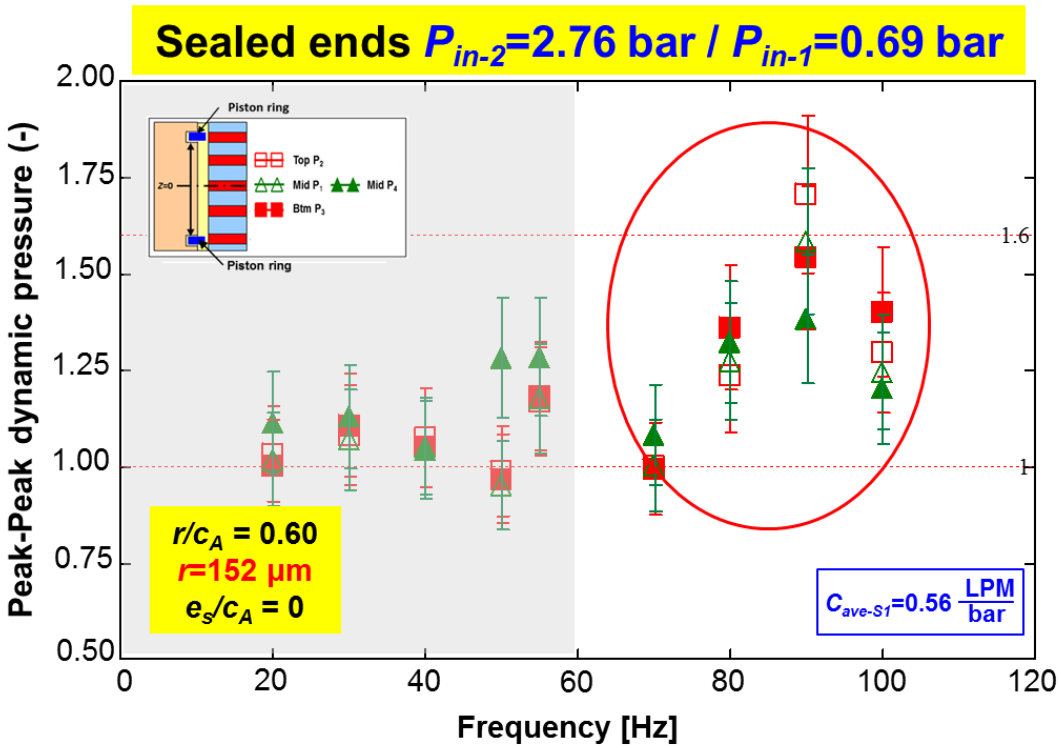

Figure 30. Sealed ends damper A: Ratio of recorded *peak-to-peak* film dynamic pressures, P_{sealed}: P_{in-2}=2.76 bar/P_{in-1}=0.69bar, versus excitation frequency (ω). Centered (e_s=0) circular orbit tests with radius r/c_A=0.60. Circled pressures indicate high whirl frequency ω>60Hz. Measurements at damper mid-plane, top and bottom (half-planes) and end grooves. (Inset shows location of pressure sensors).

Note that during the tests with the sealed ends SFD (C_{ave-S1} =0.56 LPM/bar) supplied with a low pressure (P_{in-1}=0.69 bar) operating at a large amplitude motion r/c_A>0.45 and at high whirl frequency ω>60 Hz, visual inspection of the oil collectors at the damper top and bottom discharge sections reveals a foamy-bubbly air-in-oil mixture that can be described as a milky oil.

Figure 31(a) displays the phenomenon of air ingestion for a test with the sealed ends damper operating with P_{in-1} = 0.69 bar, r/c_A > 0.45 and ω = 80 Hz (squeeze velocity $r\omega$ =

5.7 cm/s). Note that the foamy-mixture leaks first through the piston ring slit (Θ=345º (-15º)) and later extends towards the oil outlet (Θ=150º). Hence, air ingestion[4] persists on the sealed ends SFD configuration operating with a low lubricant supply pressure $P_{in\text{-}1}$=0.69 psig. The red dashed line indicates the location of piston ring slit.

On the other hand, the same damper with ~4 times higher lubricant supply pressure $P_{in\text{-}2}$=2.76 bar does not show signs of a bubbly air-oil mixture (milky oil) at the top oil collector, see Fig 27(b). For $P_{in\text{-}2}$=2.76 bar, the jet flow ejects through the ring slit to break later into small droplets falling into the surface at the top oil collector to create surface aeration (bubbles). These sporadic bubbles are not induced by air ingestion in the SFD. Note that the incident of air ingestion in the SFD is differentiated by a milky oil emerging from the PR slit.

For further illustration, please watch the video (https://www.youtube.com/watch?v=PulQisPDRtY) showing the time evolution of the bubbly mixture for operation with oil delivered at two lubricant supply pressure conditions ($P_{in\text{-}1}$=0.69 bar, $P_{in\text{-}2}$=2.76 bar).

[4] Later in Figures 32, 33 and 34 evidence the occurrence of air ingestion and oil cavitation.

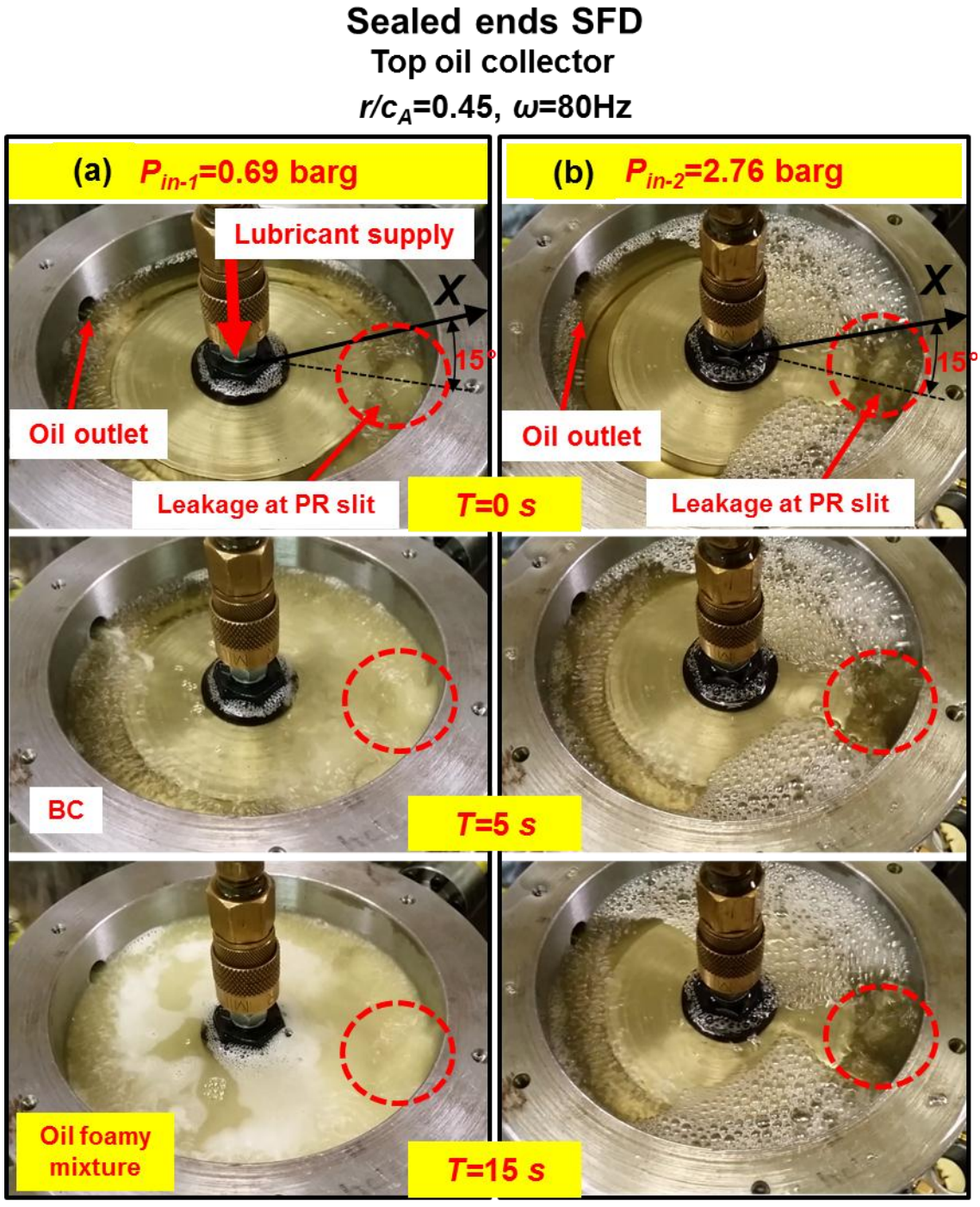

Figure 31. Photographs of top oil collector showing a lubricant exit condition. Sealed ends damper sections for whirl motions with r/c_A=0.45 and ω=80 Hz with lubricant supply pressure (a) P_{in-1}=0.69 bar and (b) P_{in-2}=2.76 bar. Top figures: elapse time T=0 s. Middle figures: elapse time T=5 s. Bottom figures: elapse time T=15 s. (Pictures taken on October 9, 2015). https://www.youtube.com/watch?v=PulQisPDRtY

4.2.5. Examples of Recorded Squeeze Film Dynamic Pressures Profiles

Figures 32 and 33 depict the recorded squeeze film dynamic pressures (at z=0) and the film thickness for the sealed ends damper with two distinct lubricant supply pressure $P_{in\text{-}1}$~0.69 barg ($Q_{in\text{-}1}$=0.68 LPM) and $P_{in\text{-}2}$~2.76 barg ($Q_{in\text{-}2}$=2.68 LPM) operating with circular centered orbits with amplitudes r/c_A=0.30, 0.45 and 0.60 and whirl frequency ω=90 Hz. Note that the end seal flow conductance is C_{ave-S1} =0.56 LPM/bar.

The figures show the recorded pressure data for three periods of whirl motion (T_P=2π/ω=0.011 s) as recorded by sensors P_4 (Θ=225°) and P_1 (Θ=315°, see Fig. 26). The film thickness is calculated as

$$h_{(\Theta,t)} = c + X_{(t)} \cos\Theta + Y_{(t)} \sin\Theta \tag{14}$$

where

$$\begin{aligned} X_{(t)} &= r_x \cos(\phi_x + \omega t) + e_s \cos\left(\tfrac{\pi}{4}\right) \\ Y_{(t)} &= r_y \cos(\phi_y + \omega t) + e_s \sin\left(\tfrac{\pi}{4}\right) \end{aligned} \tag{15}$$

where e_s is the static eccentricity along (Θ=45°); r_x, r_y are the displacements of whirl motion along the X,Y directions, and ϕ_x, ϕ_y =ϕ_x + ½ π, are the arguments of the fundamental components of the Fourier series built functions from the measured displacements along the X, Y axes.

In Figures 32 and 33, the dynamic film pressures increase with an increase in orbit amplitude (r) and are periodic in nature. Importantly enough, with an increase in orbit amplitude (r), the sealed ends damper supplied with a higher pressure $P_{in\text{-}2}$=2.76 bar generates larger dynamic pressures than those pressures obtained with the damper with a

low oil supply pressure ($P_{in\text{-}1}$=0.69 bar). At moderate to large orbit amplitude motions of $r/c_A \geq 0.3$, the difference is due to air ingestion and oil cavitation in the lubricant film land for the sealed ends damper with lower $P_{in\text{-}1}$. Interestingly enough, for sealed ends damper with smaller oil leakage C_{ave-S1} =0.56 LPM/bar and with motion amplitudes r/c_A=0.6, the *peak-peak* dynamic film land pressure reaches ~8.5 barg that is, ~8.5 times the ambient pressure (1 bar).

The pressure profile shows high frequency spikes perhaps evidencing the collapse of air/gas bubbles. Note the negative dynamic pressure zone ends with a shape typical of oil vapor cavitation [51-53]. Eventually, a foamy-bubbly air-oil mixture exits through the piston rings slit as in the visual inspection shown in Fig. 31. It is important to note, however, that the oil in the test rig has an unknown amount of dissolved air.

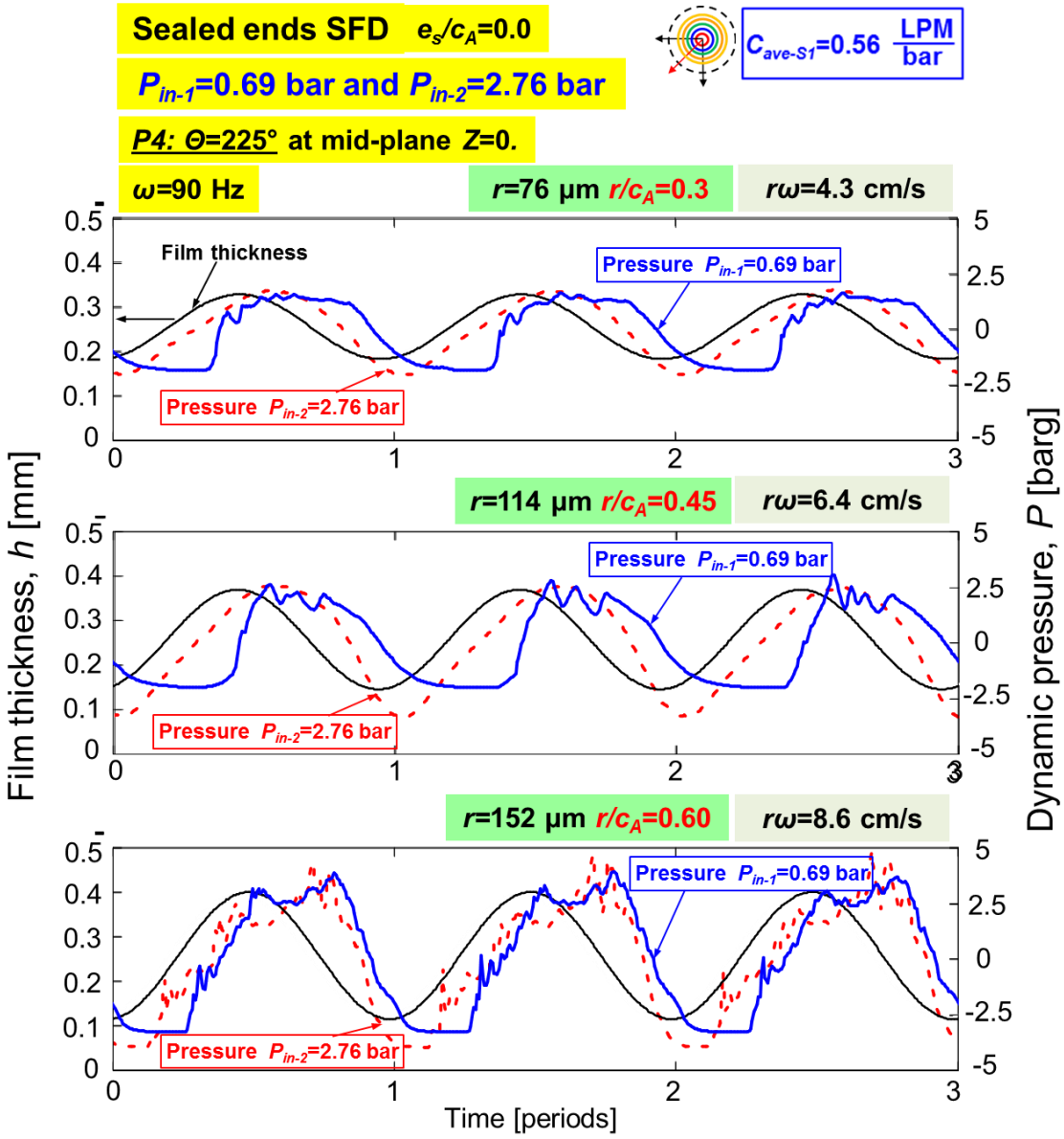

Figure 32. Sealed ends damper with lubricant supply pressure P_{in-1}=0.69 bar and P_{in-2}=2.76 bar: Dynamic film pressures (P) and film thickness (h) recorded at Θ=225° ($P4$) versus time (t/T) for measurements at mid-plane (z=0). Circular centered orbit with frequency ω=90 Hz. Graphs show data for orbits with magnitude r/c_A=0.30, 0.45 and 0.60. (nominal clearance c_A=254 μm).

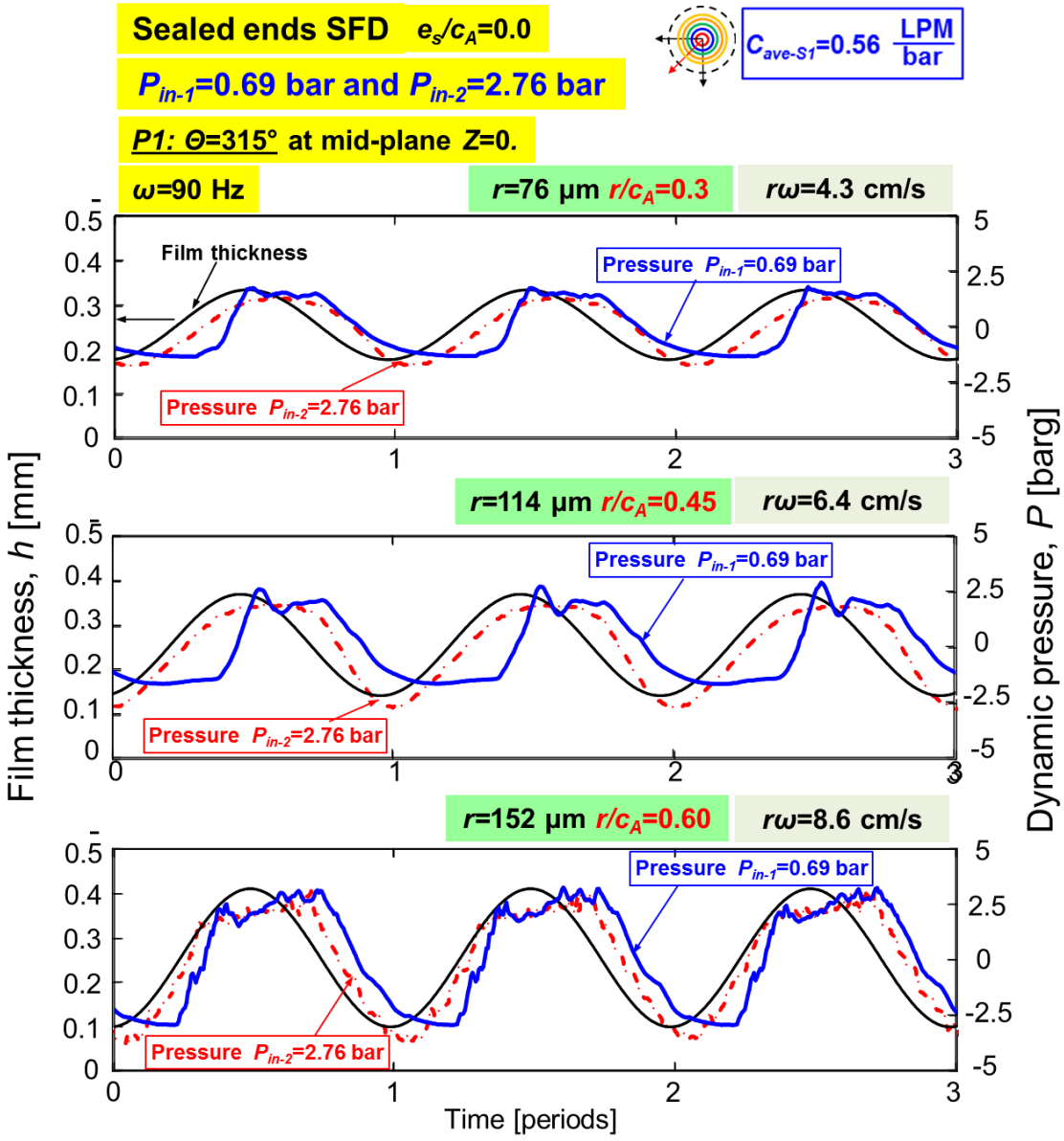

Figure 33. Sealed ends damper with lubricant supply pressure P_{in-1}=0.69 bar and P_{in-2}=2.76 bar: Dynamic film pressures (P) and film thickness (h) recorded at Θ=315° ($P1$) versus time (t/T) for measurements at mid-plane (z=0). Circular centered orbit with frequency ω=90 Hz. Graphs show data for orbits with magnitude r/c_A=0.30, 0.45 and 0.60. (nominal clearance c_A=254 μm).

Figure 34 shows the measured dynamic pressure and the film thickness for both the open and sealed ends dampers, respectively. Note the pressure for the open ends SFD is multiplied by 10 for better visualization. For damper A (c_A=254 μm), the sealed ends configuration generates ~12-15 times larger peak-peak dynamic pressures than those in the open ends configuration. Recall the sealed ends damper (C_{ave-S1}=0.56 LPM/bar) generates ~13 times larger damping and ~11 times more inertia coefficients than those of open ends. In general, the open ends SFD shows a peak pressure after the location of maximum squeeze velocity, |dh/dt|, whereas the sealed ends SFD shows a much broader pressure profile.

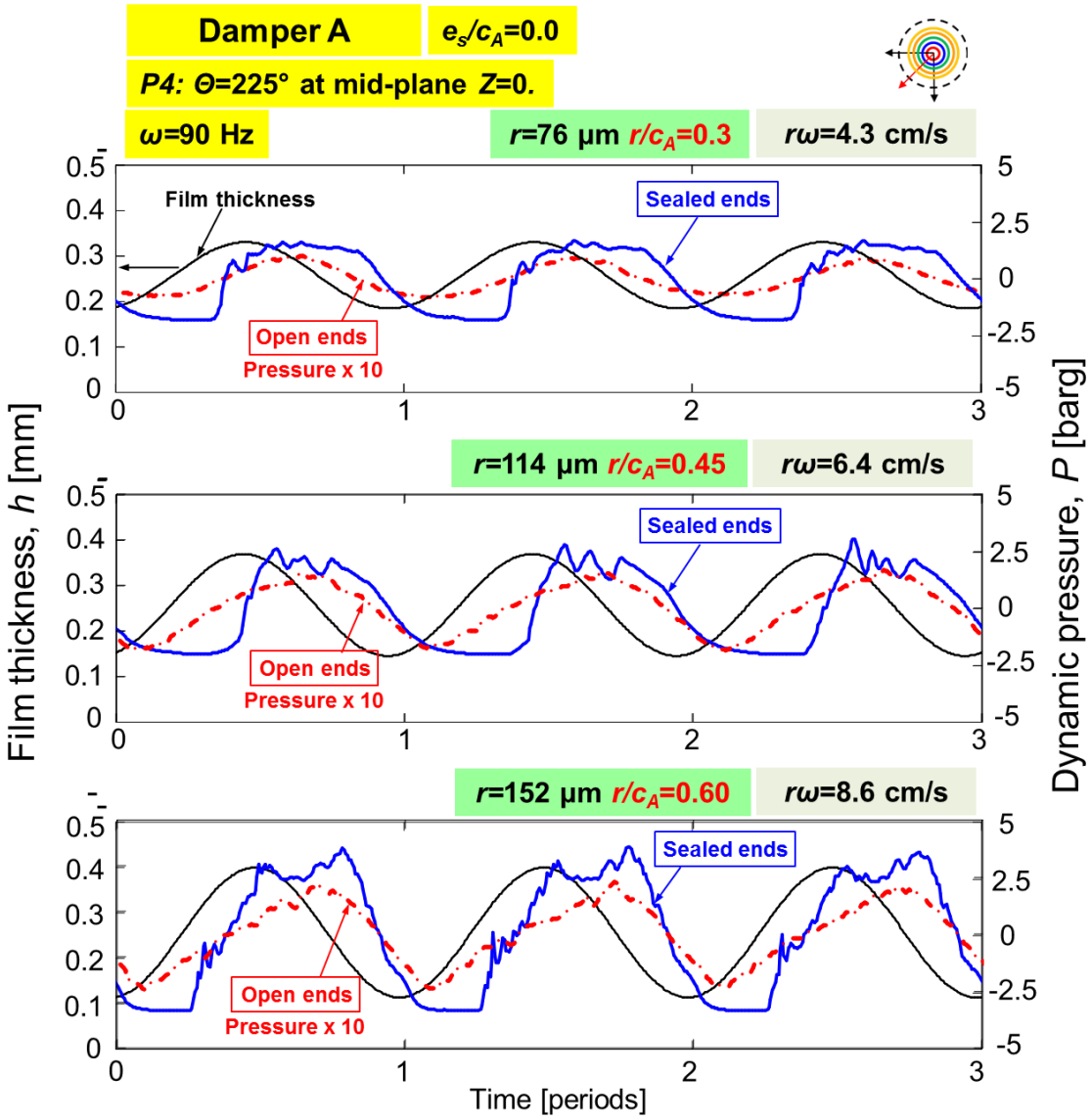

Figure 34. Damper A with sealed ends and open ends: Dynamic film pressures (*P*) and film thickness (*h*) recorded at Θ=225° versus time (*t*/*T*) for measurements at mid-plane (*z*=0). Circular centered orbit with frequency *ω*=90 Hz. Graphs show data for orbits with magnitude *r*/c_A=0.30, 0.45 and 0.60. Pressure for the open ends damper multiplied by 10 for better visualization. (nominal clearance c_A=254 μm, pressure supply at $P_{in\text{-}1}$~0.69 barg for sealed ends damper and at $P_{in\text{-}3}$~0.35 barg for open ends damper).

4.3. Predicted Versus Experimental SFD Force Coefficients

This section presents predictions from *orbit analysis* [7] and comparisons results against the experimentally identified SFD force coefficients. Recall that the computational physics model implements a Finite Element Method (FEM) to solve a modified Reynolds equation that includes temporal fluid inertia effects [33,34], i.e.,

$$\frac{\partial}{\partial x}\left(h^3\frac{\partial P}{\partial x}\right)+\frac{\partial}{\partial z}\left(h^3\frac{\partial P}{\partial z}\right)=12\mu\frac{\partial h}{\partial t}+\rho h^2\frac{\partial^2 h}{\partial t^2} \tag{16}$$

where P, μ, and ρ are film pressure, lubricant viscosity and density, respectively. Note the model satisfies flow continuity at the intersection between a groove and a film land.

Table 5 lists the physical parameters to obtain predictions of the SFD dynamic force coefficients for a sealed ends configuration. Figure 35 depicts schematic views of the SFD test rig and the damper axial film length and radial clearance as modeled in computational program. The piston ring seals are installed at the top and bottom ends grooves of the journal. Due to symmetry, only half of the damper axial length needs to be modeled. Five elements model half of the axial film land length and 121 elements model the circumference of the damper. The computational model best reproduces the experimental dynamic pressure when the lubricant gaseous cavitation pressure is set to P_{cav}=-1 barg, i.e., P_{cav}=0 bar (absolute).

Note that the piston ring is modeled as a local end seal using its flow conductance $\bar{C}_{seal-1}$ despite the (measurement) fact that the PR slit is the only route through which the lubricant evacuates the damper. Although modeling PRs as a local flow restriction is common [31,54], the practice is likely physically incorrect.

Table 5. Dimensions of sealed ends SFD with large clearance (c_A=254 μm). Three feed holes (ϕ=2.5 mm) at damper mid-plane (120° apart)

Parameter	Value	Units
Journal Diameter, D	127 (5)	mm (inch)
Nominal Axial Film Land Length, L	25.4 (1.00)	mm (inch)
Nominal Radial Clearance, c	0.254 (10)	mm (mil)
Ambient pressure at ends	0.0	barg (psig)
Supply pressure, P_{in}	0.69 (10) or 2.76 (40)	barg (psig)
Flow conductance, $\bar{C}_{seal-1}=\frac{C_{ave-S1}}{\pi D}$	$2.34\text{x}10^{-4}$ ($2.49\text{x}10^{-3}$)	($mm^2/(s\cdot Pa)$) ($in^2/(s\cdot psig)$)
Seal conductance, C_{ave-S1}	0.56	LPM/bar
Cavitation pressure, P_{cav}	-1.0 (-14.5)	barg (psig)
Supply Temperature, T_S	23 (73)	°C (°F)
Viscosity[5]	2.60 (0.377)	cP (micro-Reyns)
Density	799 (49.9)	kg/m^3 (lb/ft^3)

[5] Please see Appendix B for further details.

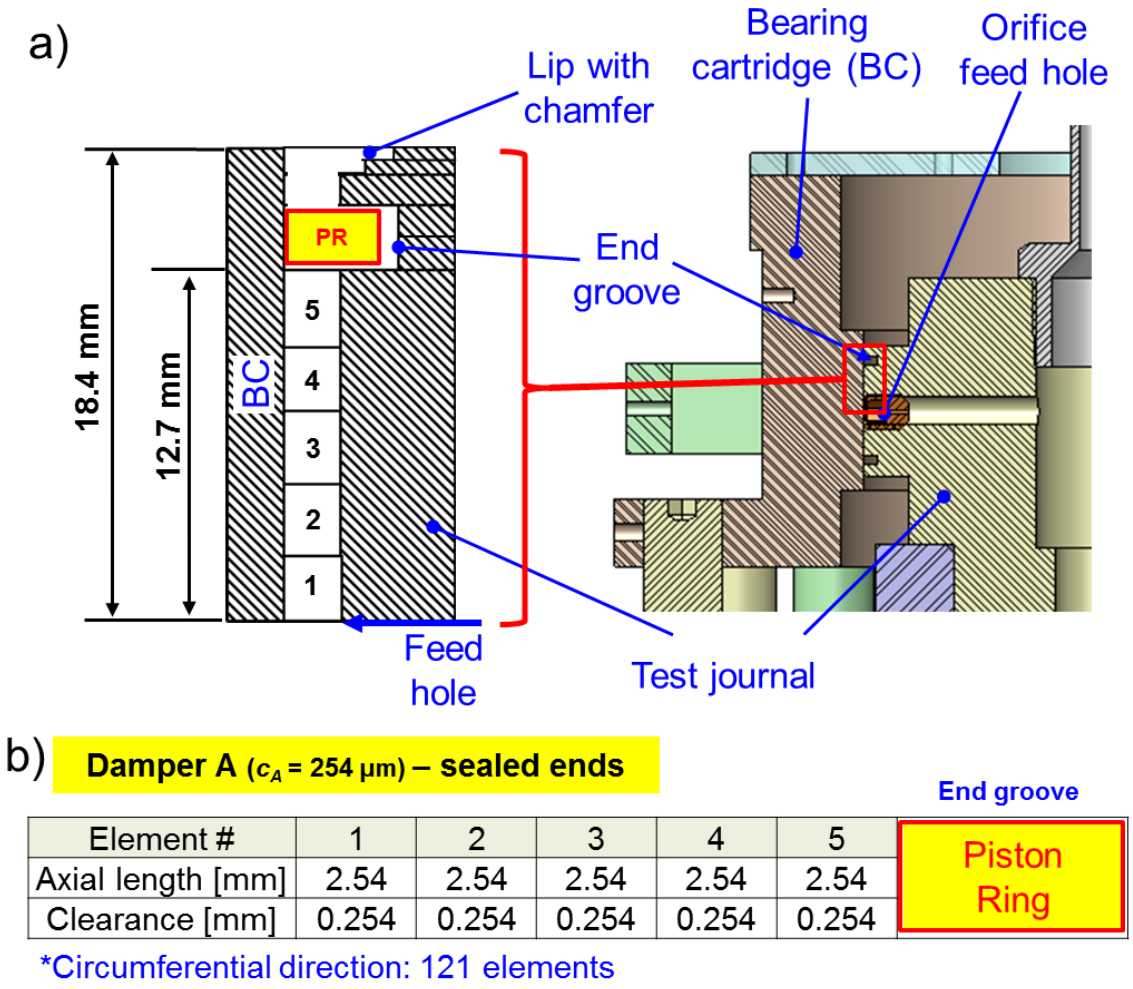

Figure 35. (a) Depiction of SFD test rig section and elements to model half the damper axial length. Elements 1-5: film land (axial).

The computational program performs an *orbit analysis* [7] process to estimate the SFD force coefficients. This feature numerically reproduces the actual test conditions; that is, the program computes the instantaneous damper reaction forces to specific journal amplitude motion (r_X, r_Y), static eccentricity (e_X, e_Y) and whirl frequency (ω) in one cycle of whirl motion for a selected range of frequencies as shown in the Figure 36.

Then, calculated SFD forces (time domain) are transformed into the frequency domain using a Fourier analysis to construct impedance functions (**H**). SFD force coefficients (*K,C,M)* are identified by curve fitting the real and imaginary parts of the impedance over a designated frequency range; that is, Re(**H**)→**K**-ω^2**M,** Im(**H**)→***C***ω.

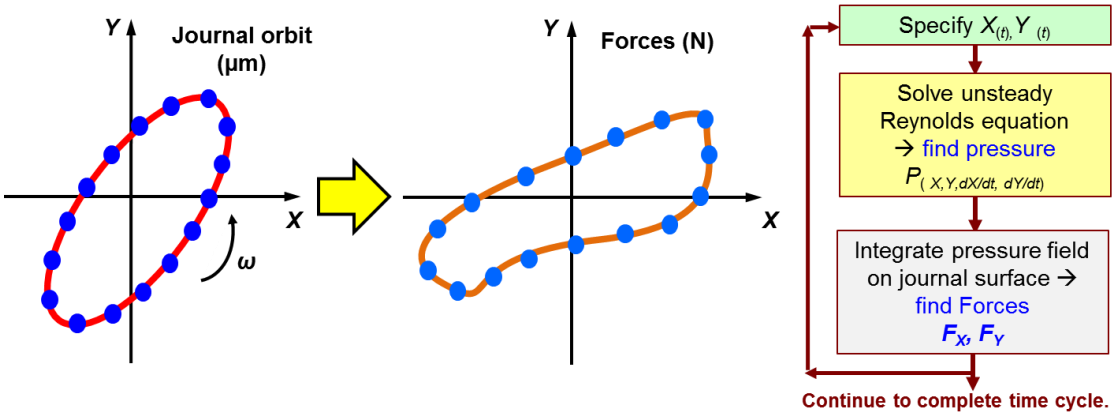

Figure 36. (a) Example of analysis for an elliptical off-centered orbit: journal motion *X* versus *Y* and fluid film bearing reaction forces (F_X versus F_Y). Dots indicate discrete points at which the numerical program predicts forces and (b) illustration of algorithm flow chart [7].

4.3.1. Predictions Based on Classical Lubricant Theory

Classical Lubrication Theory for an open ends, full film SFD (i.e., full film cavitation and small amplitude motion ($r \to 0$) about center), predicts damping and inertia force coefficients [1] as (with L_{eff}=1.17L)

$$C_{XX-Open\ ends} = C_{YY-Open\ ends} = \pi \frac{\mu R L_{eff}^3}{c^3} = 0.9 \frac{\text{kN.s}}{\text{m}}, \qquad (17)$$

$$M_{XX-Open\ ends} = M_{YY-Open\ ends} = \pi \frac{\rho R L_{eff}^3}{12c} = 1.4\ \text{kg}$$

The simple model does not account for any feeding hole(s). It is noteworthy to realize that the simple equation uses an effective film length L_{eff}. As detailed in Ref.[5], L_{eff} accounts the pressure generation at the end grooves L_{eff} larger than the design film land length L=25.4 mm and shorter than the actual wetted length L_{tot}=36.8 mm.

For a damper with perfectly sealed ends (i.e., without axial leakage or the long bearing model) operating at small amplitude motions ($r \rightarrow 0$) about the journal center (e_s=0), predicts damping and inertia force coefficients as [18]

$$C_{XX-Sealed} = C_{YY-Sealed} = 12\pi \frac{\mu R^3 L}{c^3} = 39.7 \frac{\text{kN.s}}{\text{m}},$$
$$M_{XX-Sealed} = M_{YY-Sealed} = \pi \frac{\rho R^3 L}{c} = 64.4 \text{ kg} \tag{18}$$

It is noteworthy to realize that an ideal fully sealed ends SFD can provide $12(R/L)^2$ ~75 times more damping and added mass than an open ends SFD.

Figure 37 depicts the predicted SFD direct damping and added mass force coefficients versus end seal flow conductance ($\bar{C}_{seal}$) and flow rate (Q_{in}). The predictions correspond to a circular orbit amplitude of r/c_A=0.15 about a centered condition (e_s/c_A=0), where cross-coupled force coefficients are negligible as obtained in the experiments. Both the damping and inertia force coefficients increase with a decrease in flow conductance, i.e., a reduction in flow rate through the piston ring seal. Note that the prediction assumes a constant lubricant temperature. As the flow conductance becomes larger $\bar{C}_{seal} \rightarrow \infty$ (more leakage), the SFD force coefficients (C, M) converge to those for the open ends (full film) SFD model in Eq.(17). On the other hand, with $\bar{C}_{seal} \rightarrow 0$ (less

leakage, $1.0 \cdot 10^{-5} \text{mm}^2/(\text{sPa})$), the SFD force coefficients are less than ~50% of those obtained with perfectly sealed ends model in Eq.(18). This is because the simple model in Eq.(18) does not account for the oil feed hole(s).

The end seals flow conductances ($\bar{C}_{seal-1}$ and $\bar{C}_{seal-2}$) are overlaid with the predictions. As the seal flow conductance increases both the damping and added mass force coefficients decrease until they reach the open ends SFD condition. Note that for $\bar{C}_{seal} < 4.0 \cdot 10^{-4} \frac{\text{mm}^2}{\text{s} \cdot \text{Pa}}$ (~C_{ave} = 1 LPM/bar) both damping and inertia coefficients do not increase significantly. Additionally, notice that the predicted added mass coefficients for C_{ave-S1} and C_{ave-S2} fell short by ~30% of the experimental added mass coefficients, M_{SFD}=~37 kg. Further discussion follows when presenting Figure 38.

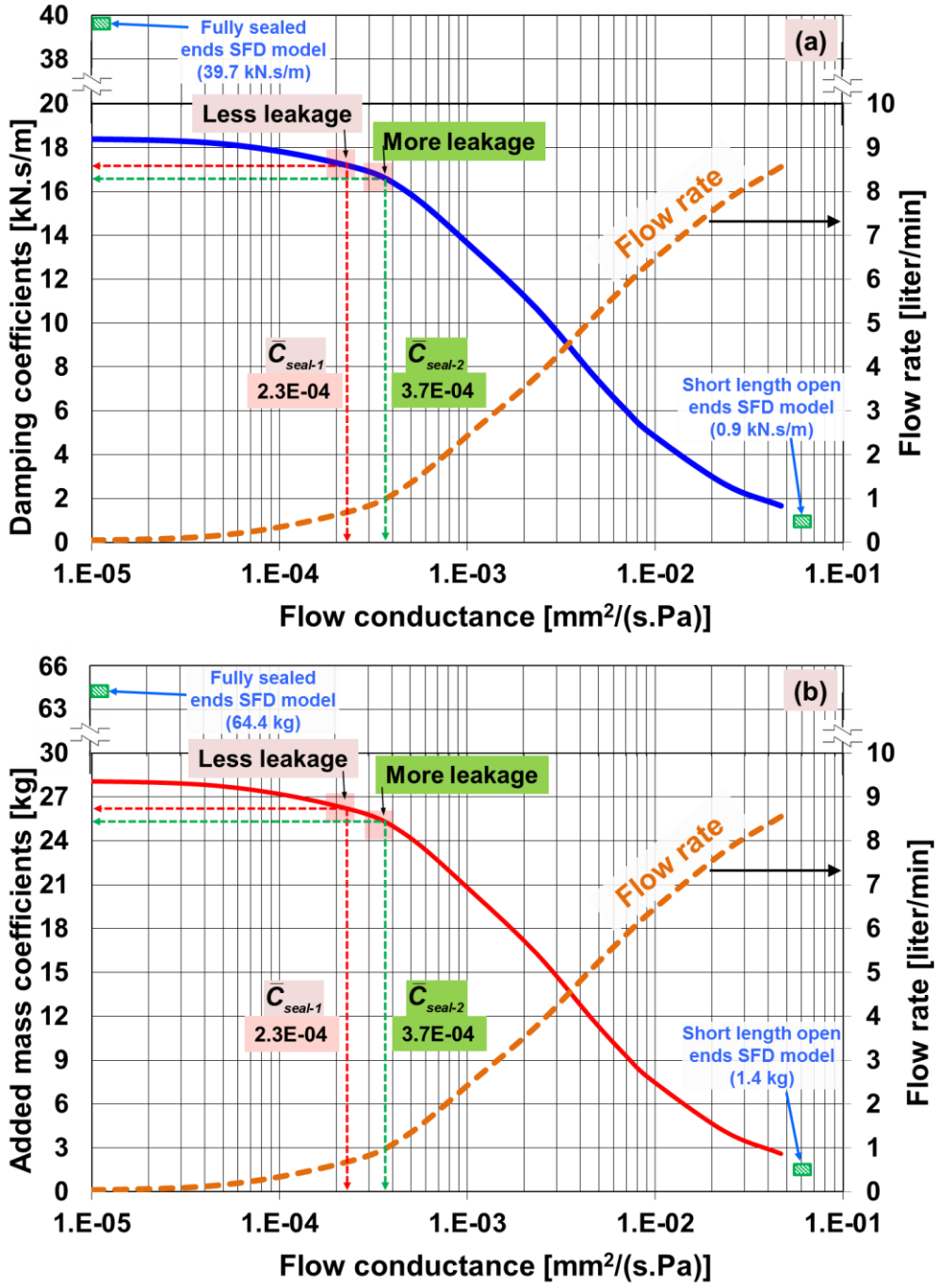

Figure 37. Predicted SFD dynamic force coefficients versus end seal flow conductance and flow rate: (a) damping (C_{XX}=C_{YY})$_{SFD}$ and (b) mass (M_{XX}=M_{YY})$_{SFD}$ coefficients. Lubricant supply pressure P_{in-1}=0.69 bar. End seal flow conductance labeled C_{seal-1}=2.34·10^{-4}mm^2/(sPa) and C_{seal-2}=3.70·10^{-4}mm^2/(sPa). Graphs show data for orbit with magnitude r/c_A=0.15 and e_s=0.

Figures 38 and 39 show comparisons of the experimental and predicted damping (C) and added mass (M) coefficients identified over the frequency range 10 – 100 Hz from small to large amplitude whirl motions (r/c_A = 0.15 – 0.60) at the centered position (e_s/c_A = 0). In Figures 38 and 39, notice the difference in oil feed pressures set at P_{in}~0.69 barg and P_{in}~2.76 barg for operation. The figures also includes predictions from Eq.(17) for an open ends SFD, and from Eq.(18) for a fully sealed ends SFD, respectively.

With a low lubricant supply pressure $P_{in\text{-}1}$~0.69 barg, (as shown in Figure 38) the predicted damping force coefficients show an opposite trend of the test coefficients with increasing whirl motion amplitude (r). That is, predicted C_{XX} and C_{YY} first decrease as the whirl amplitude grows to $r/c_A < 0.3$, then remain constant above $r/c_A > 0.3$. On the other hand, the experimental damping coefficients show an increase with orbit amplitude r.

Both predicted and experimental added mass coefficients (M_{XX}, M_{YY}) decrease with the whirl motion (r). The predictions agree well with the test M_{XX} and M_{YY} for $r/c_A >$ 0.15; however, the mass coefficients are under predicted by ~30% at the small amplitude motion for r/c_A = 0.15.

In Figure 39, for operation with a larger $P_{in\text{-}2}$, the predicted damping coefficients remain constant with increasing orbit amplitude motions. These trends closely resemble the test results.

The predicted and experimental SFD added mass coefficients (M_{XX} , M_{YY}) show a large discrepancy from small to large amplitude whirl motions (r/c_A = 0.15 - 0.60). This difference increases from 30% to 65% with increasing orbit motions. The difference is

perhaps due to the physical model representing the PR as a local end seal and/or neglecting the volume in the three feed holes. Note that the feedholes amount to ~15% of the lubricant volume in the film land (see Appendix A) [5].

4.4. Conclusion

The section presented single frequency dynamic loads tests conducted with both an open ends and a sealed ends SFD. The operating conditions differ in lubricant supply pressure and two end seals with differing seal flow conductance. For the sealed ends SFD, by increasing four times the lubricant supply pressure from $P_{in\text{-}1}$~0.69 barg to $P_{in\text{-}2}$~2.76 barg, the SFD direct damping coefficients do not significantly increase with increasing amplitude of motion (r/c_A) while the SFD added mass coefficients show a large increase (see Fig. 22).

For small orbit amplitude r/c_A = 0.15 and for increasing static eccentricity e_s/c_A = 0.0-0.5, the sealed ends damper operating with large $P_{in\text{-}2}$ provides ~26% - 50% larger direct damping while the inertia coefficients show similar magnitude for both dampers for $P_{in\text{-}1}$ and $P_{in\text{-}2}$ (see Fig. 23).

The piston ring end seals are effective in reducing the side leakage and thus the sealed SFD with C_{ave-S1} provides 11-13 times more damping and eleven times larger added mass coefficients than the open ends configuration.

The peak-peak dynamic film pressures measurements obtained for operation with two lubricant supply pressures show that the tests with large oil supply pressure ($P_{in\text{-}2}$ = 2.76 bar) generate ~20% larger *p-p* dynamic film pressure. For increasing orbit

amplitudes r/c_A = 0.15 – 0.60, the dynamic pressure measurements and a visual inspection show that the air ingestion and oil cavitation persists for the sealed ends SFD with a low lubricant supply pressure $P_{in\text{-}1}$=0.69 psig which most likely leads to a large decrease in direct added mass coefficients.

Physical model (numerical) predictions agree well with the experimental damping and added mass coefficients; albeit under predicting by ~30% the added mass coefficients for motions with r/c_A = 0.15. The difference may be caused due to the physical model neglecting the volume in the three feed holes (see Appendix A) and/or the PR modeled as a local end seal. Notice the fully sealed ends SFD model and simple formulas in Eq.(18) over-predict the damping and inertia force coefficients by a factor of 2. The notable discrepancy between the simple formulas and the test result is attributed to the three feed holes that prevent the generation of (high) dynamic pressure in the film land.

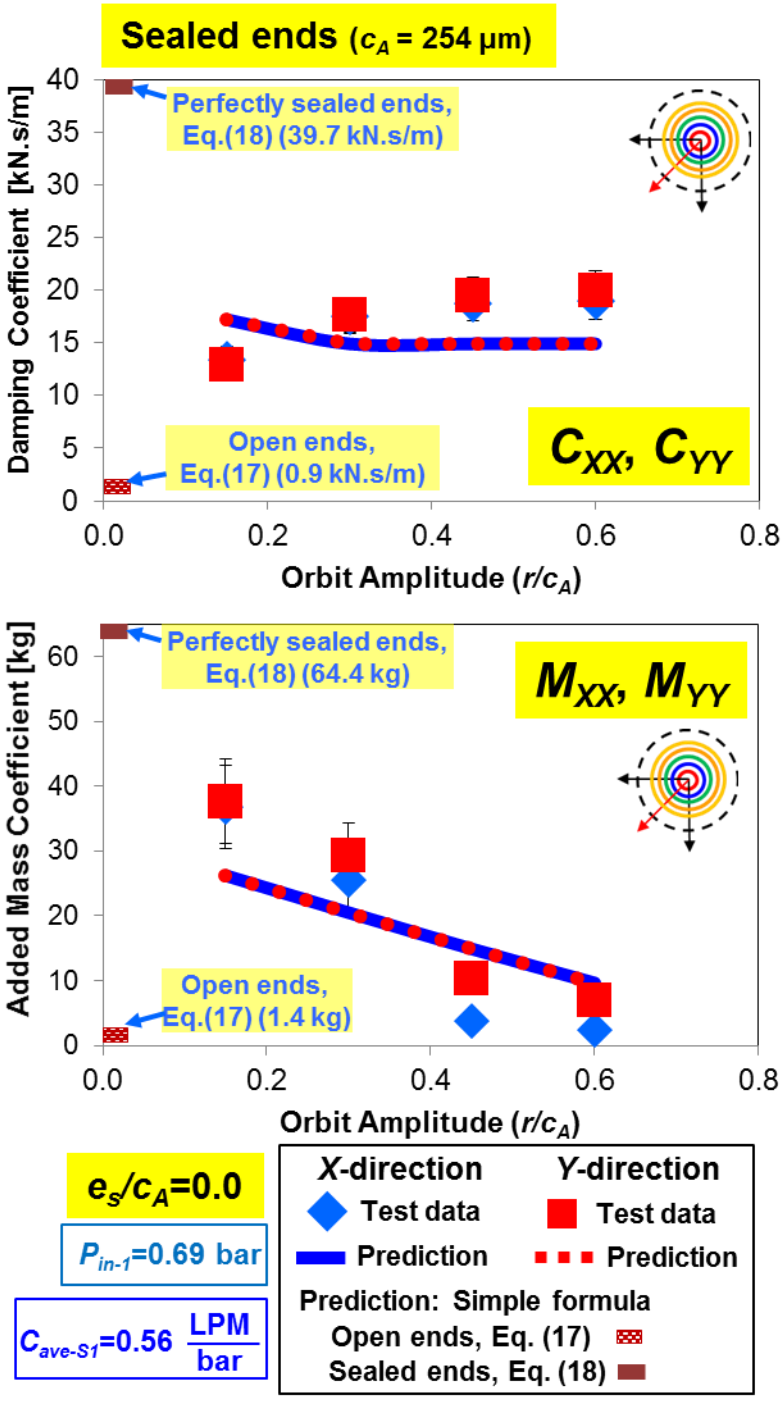

Figure 38. Sealed ends: Experimental and predicted SFD direct damping (*C*) and added mass (*M*) coefficients versus amplitude (r/c_A) for circular orbits, centered (e_S=0) with lubricant supply pressure P_{in-1}=0.69 bar. End seal flow conductance C_{ave-S1}=0.56 LPM/bar.

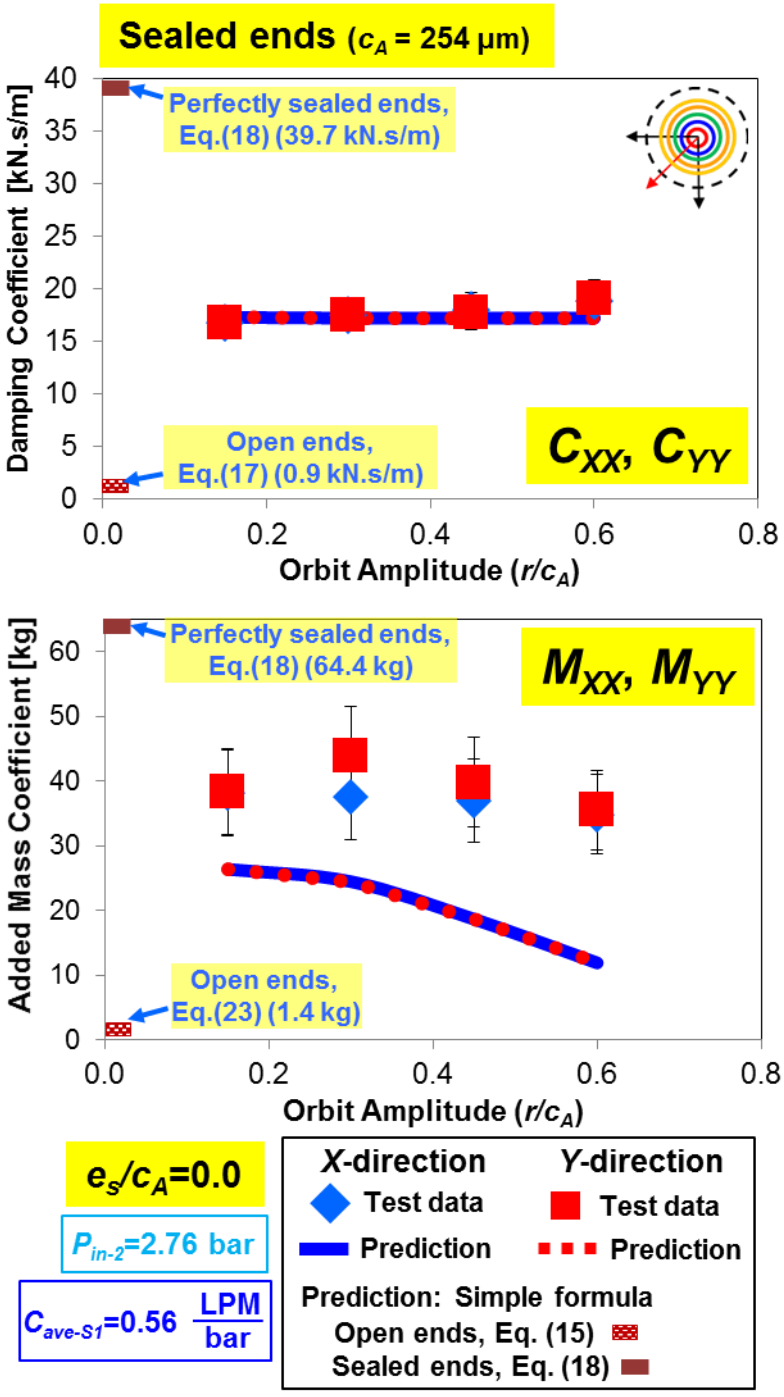

Figure 39. Sealed ends: Experimental and predicted SFD direct damping (*C*) and added mass (*M*) coefficients versus amplitude (r/c_A) for circular orbits, centered (e_S=0) with lubricant supply pressure P_{in-2}=2.76 bar. End seal flow conductance C_{ave-S1}=0.56 LPM/bar.

5. SINE-SWEEP FREQUENCY DYNAMIC LOAD TESTS*

5.1. Experimental Procedure

Sine-sweep frequency dynamic load tests aim to validate the SFD force coefficients identified from the single frequency dynamic load tests. The substantial benefit of a sine-sweep frequency dynamic load test is that it saves time to identify the system force coefficients as compared to a multitude of single frequency dynamic load tests (with constant angular acceleration α=0)[6].

The sine-sweep frequency dynamic load test utilizes a similar procedure to the one described in section 'Description of Single Frequency Dynamic Load'. That is, the dynamic loads are exerted by the shakers in the *X* and *Y* directions as

$$\mathbf{F}_{CW} = F\begin{bmatrix}\cos(\phi_{(t)})\\ \sin(\phi_{(t)})\end{bmatrix};\ \mathbf{F}_{CCW} = F\begin{bmatrix}\cos(\phi_{(t)})\\ -\sin(\phi_{(t)})\end{bmatrix} \tag{19}$$

where $\phi_{(t)} = \omega_{(t)}t$ with $\omega_{(t)} = \alpha t + \omega_{start}$; α denotes a constant angular acceleration (frequency ramp rate) defined as

$$\alpha = \left(\frac{\omega_{end} - \omega_{start}}{T^*}\right) \tag{20}$$

* Reprinted with permission from "Transient Response of a Short-Length (*L/D*=0.2) Open Ends Elastically Supported Squeeze Film Damper: Centered and Largely Off-Centered Whirl Motions" by San Andrés, L., Den, S., and Jeung, S.-H., 2016, ASME J. Gas Turb. Pwr., 138(12), p.122503, Copyright 2016 by ASME.

[6] The single-frequency dynamic load tests requires ~10 s to save test data at each frequency, that is, total ~100 s (10 s × 10) for tests from 10 Hz to 100 Hz. While the sine-sweep frequency dynamic load tests with a constant angular acceleration α=6.5 Hz/s requires less than ~20 s to collect test data over an identical frequency range (10 - 100 Hz).

The variables ω_{start} and ω_{end} above denote the start and end excitation frequencies, and T^* is the elapsed time of the dynamic load excitation. The sine-sweep dynamic load tests cover the frequency range 5-105 Hz with α=6.5 Hz/s.

Based on recent work in Ref.[9], if the angular acceleration is too large (α > 6.5 Hz/s), the test system is not able to reach a quasi-steady state response at each discrete frequency. Recall that the procedure for extraction of force coefficients assumes the SFD achieves a quasi-steady-state at each discrete whirl frequency. Consequently, the process affects the measured system complex stiffnesses, thus causing a poor correlation to the physical *K*-*C*-*M* model. On the other hand, if α is too small (α<6.5 Hz/s), the sine-sweep frequency dynamic load test takes a long time to collect all data. This leads to losing its advantage for quick evaluation of force coefficients.

Table 6 lists the sine-sweep dynamic load tests performed with sealed ends damper A. The operating conditions include various sets of static eccentricity (e_s/c_A=0.0, 0.25, 0.5) and various shaker force amplitude (F_{avg}=120 N, 260 N, 400 N), and at lubricant supply conditions $P_{in\text{-}1}$=0.69 barg and $P_{in\text{-}2}$=2.76 barg.

Table 6. Sine-sweep frequency dynamic load tests for sealed ends damper A. End seal flow conductance $C_{seal\text{-}1}$=2.34·10^{-4} mm^2/(s·Pa). Excitation frequency range 10 – 100 Hz.

Sine-sweep frequency dynamic load (α=6.5 Hz/s)				
Dynamic load amplitude (N)	Static eccentricity, e_s/c	Inlet flow rate, Q_{in} (LPM)	Static inlet Pressure, P_{in} (bar(g))	Seal conductance, $C_{ave\text{-}S}$ (LPM/bar)
120, 260, 400	e_s/c_A = 0.0	0.68	0.69	0.56
120, 260, 400	e_s/c_A = 0.25			
120, 260, 400	e_s/c_A = 0.5			
260	e_s/c_A = 0.0	2.71	2.76	
260	e_s/c_A = 0.25			
260	e_s/c_A = 0.5			

Figure 40 shows the applied forces in the X direction (F_X) and Figure 41 shows the ensuing BC displacement from two tests of frequency ranges[7] (i) 5 – 55 Hz and (ii) 55 – 105 Hz. Note that the sweep frequency ramp rate α=6.5 Hz/s for motions departing from e_s/c_A=0. For brevity, only the applied forces and ensuing displacement in the X direction are shown; typically $F_X \sim F_Y$ and $Z_X/c_A \sim Z_Y/c_A$. The test data correspond to the average amplitude of dynamic load (a) $F_X=F_Y=F_{avg}$=120 N, (b) $F_X=F_Y=F_{avg}$=260 N, (c) $F_X=F_Y=F_{avg}$=400 N with lubricant supply pressure $P_{in\text{-}1}$=0.69 bar and (d) $F_X=F_Y=F_{avg}$=260 N with $P_{in\text{-}2}$=2.76 bar. Figures 40 and 41 both show the time trace of applied dynamic load and ensuing displacement and its discrete Fourier transform (DFT) amplitude of applied load and BC motion versus frequency.

[7] The DAQ's limitations prevent recording more than 11 s of data for a sampling rate 16384 samples/s. Thus, an experiment uses two frequency ranges (i) 5 – 55 Hz and (ii) 55 – 105 Hz to perform tests with the frequency ramp rate α=6.5 Hz/s.

Recall that the dynamic load amplitude along the X and Y direction remains fairly constant $F_X=F_Y=F_{avg}$. While the delivered dynamic load tends to decrease for whirl frequency ω=10 Hz through 30 Hz. In general, for a sine-sweep frequency dynamic load, the shakers receive a periodic voltage signal with increasing frequency and constant amplitude. However, the delivered dynamic load amplitude is not necessarily constant. This is due to a resonance (~30Hz) in the shakers' armature that leads to an inconstant in the delivered dynamic load around ω~30 Hz. Refs.[55,56] detail the explanation of the resonance of the E-shakers.

Notice that at the start and end of the excitation for both frequency ranges (i) 5 – 55 Hz and (ii) 55 – 105 Hz, the DFT amplitude of applied load rapidly changes while maintaining a magnitude that is relatively small compared to those in the 8 – 50 Hz and 60 – 95 Hz ranges. Hence, maintaining a parameter identification range of 5-105 Hz but excluding data in the ranges at the start and end of the excitation (5-7 Hz, 51-59 Hz, 96-105 Hz) give a good correlation between the assumed physical model and the experimental data (see later Figure 42). Note that the frequency range does not excite a resonance of the structure.

For dynamic loads from F_{avg}=120 N to 260 N or 400 N, the BC whirls with average orbit amplitude from Z/c_A=~0.1 to ~0.15 or ~0.2 over the identification frequency ranges. Similar to the delivered dynamic load, the BC amplitude motion first decreases with increasing whirl frequency up to ω~30 Hz and then increases to ω~50 Hz. As the frequency of the dynamic load increases from 50 Hz to 100 Hz, the BC amplitude motions tend to decrease with increasing whirl frequency.

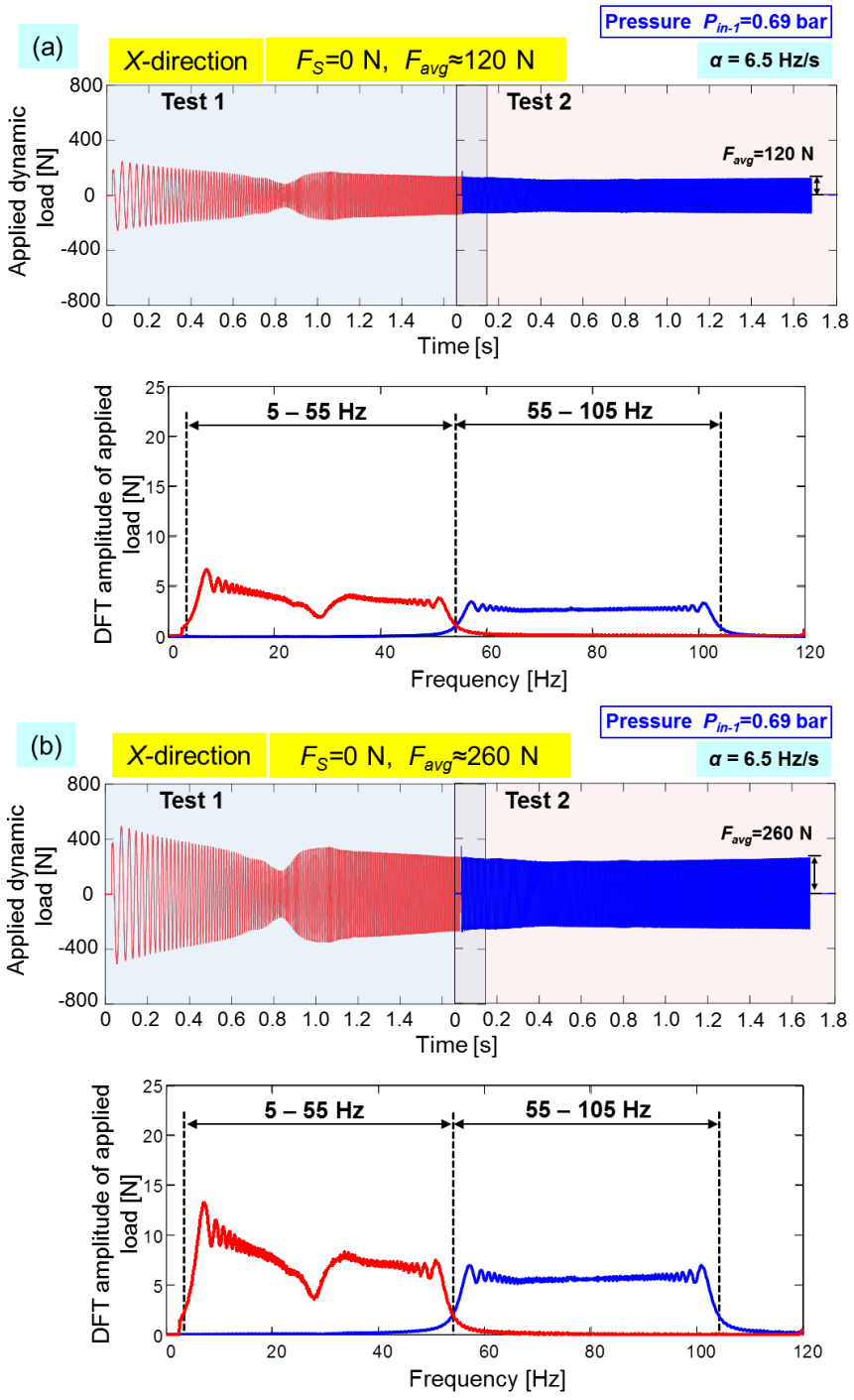

Figure 40. Time trace and DFT of applied dynamic load (F_X) for (a) F_{avg}=120 N, (b) F_{avg}=260 N, (c) F_{avg}=400 N with lubricant supply pressure P_{in-1}=0.69 bar and (d) F_{avg}=260 N with P_{in-2}=2.76 bar. Frequency range from (i) 5-55 Hz and (ii) 55-105 Hz. α = 6.5 Hz/s and static journal eccentricity e_s=0.

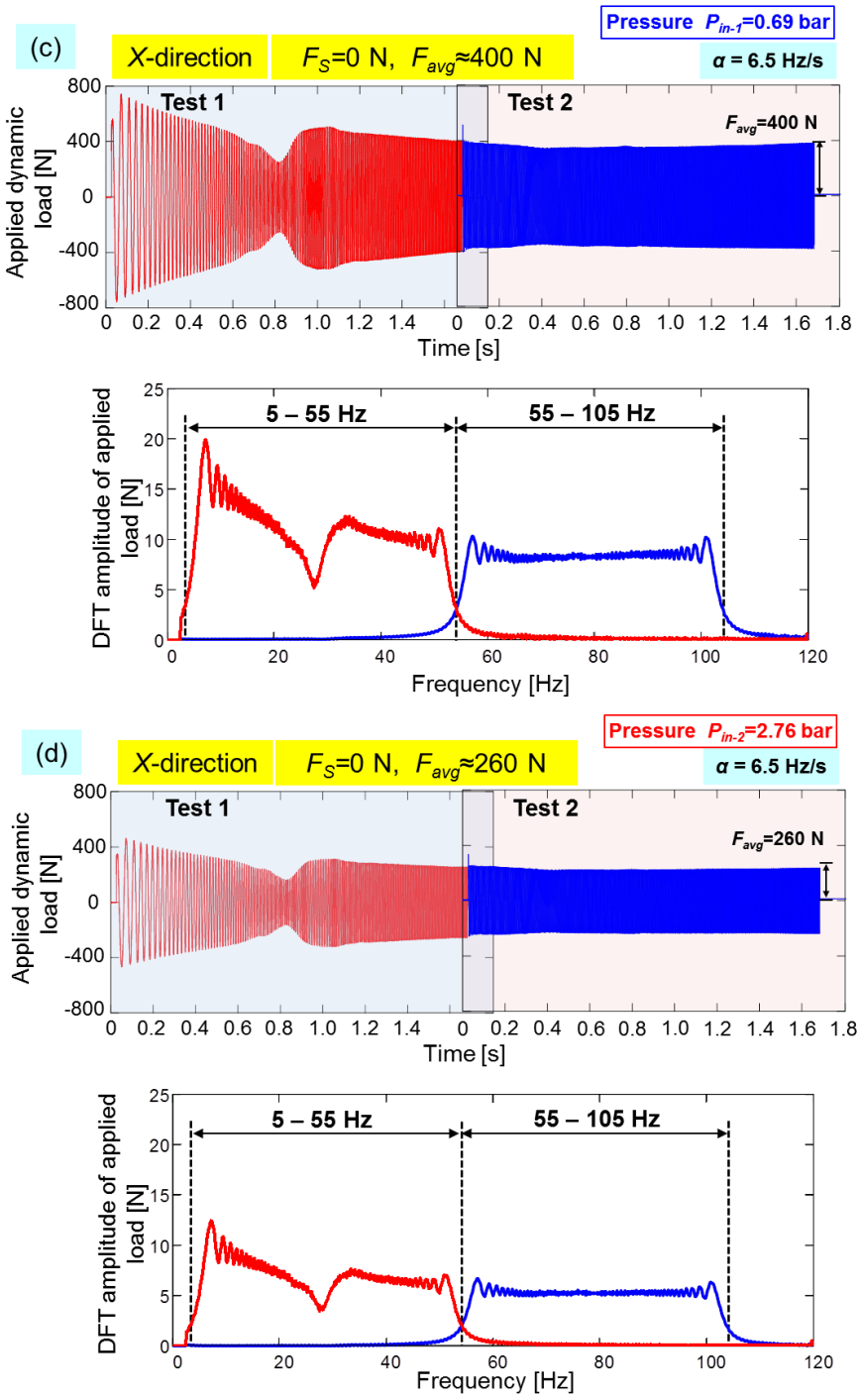

Figure 40. Continued.

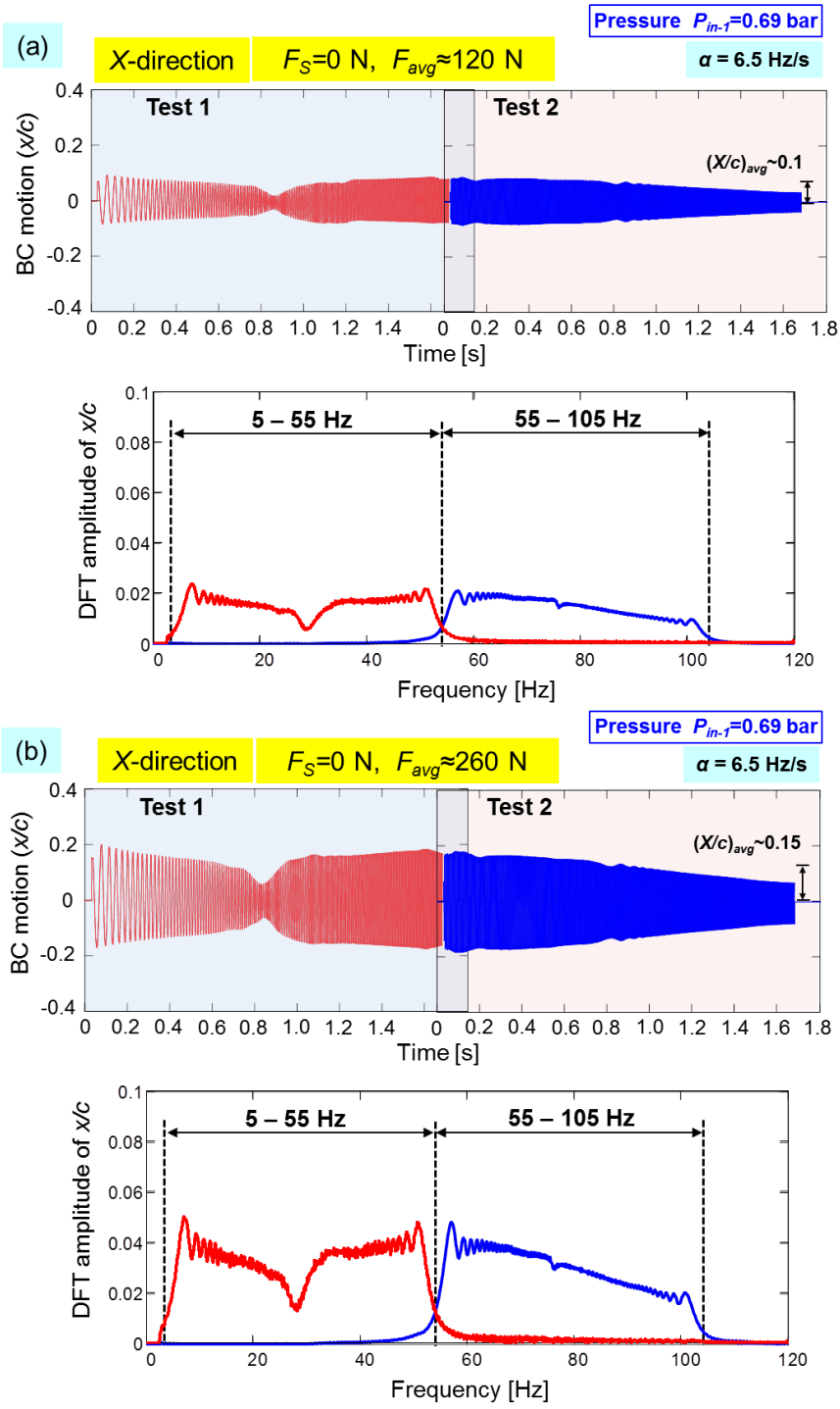

Figure 41. Time trace and DFT of ensuing BC motion (*x/c*) for (a) F_{avg}=120 N, (b) F_{avg}=260 N, (c) F_{avg}=400 N with lubricant supply pressure P_{in-1}=0.69 bar and (d) F_{avg}=260 N with P_{in-2}=2.76 bar. Frequency range from (i) 5-55 Hz and (ii) 55-105 Hz. α = 6.5 Hz/s and static journal eccentricity e_s=0.

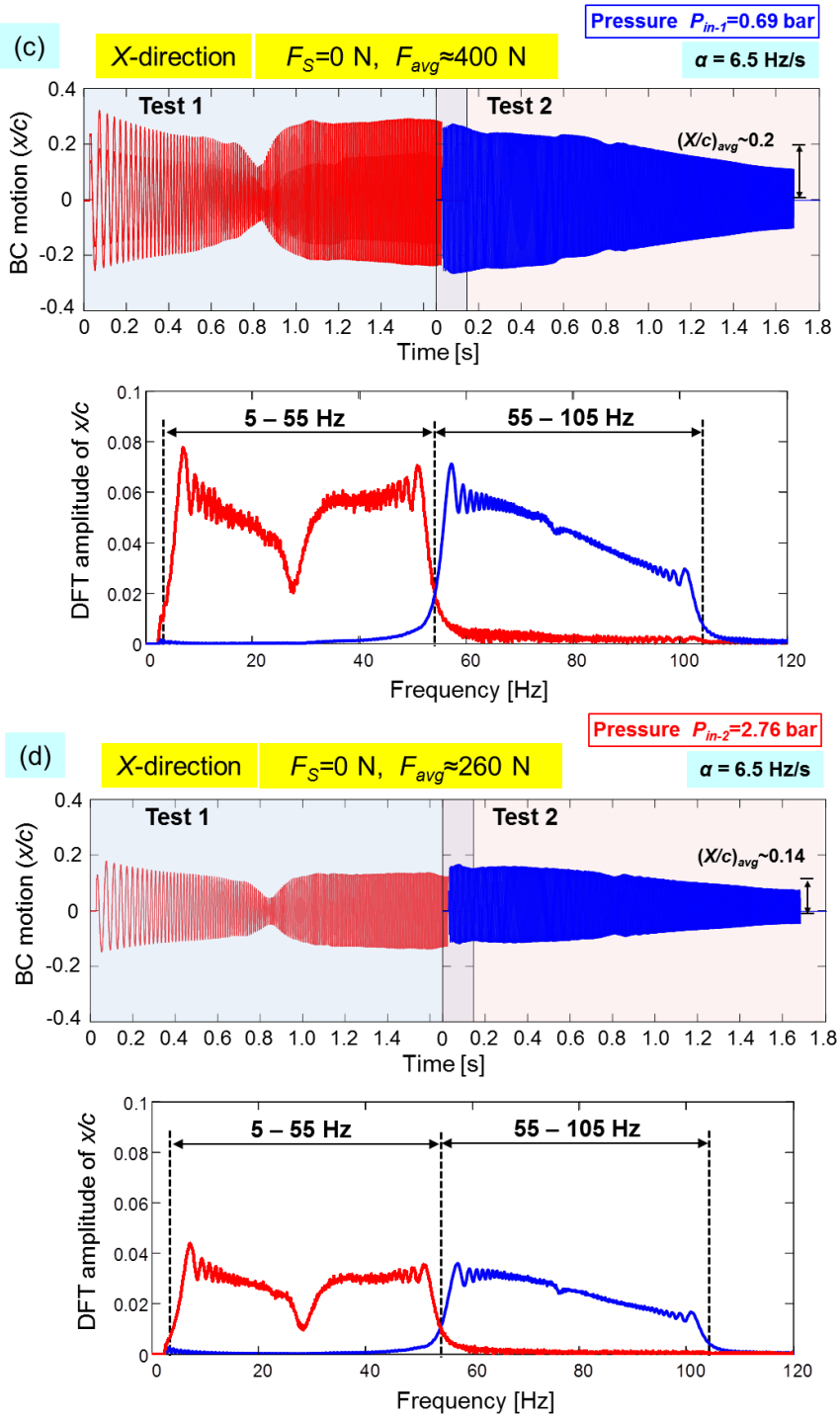

Figure 41. Continued.

5.2. Experimental Results

Figure 42 presents the real and the imaginary parts of the direct and cross-coupled dynamic impedances (H_{XX}, H_{YY}, H_{XY}, H_{YX}) obtained from sine-sweep dynamic load tests of the sealed ends SFD with an average amplitude of dynamic load F_{avg}=260 N and operating with lubricant supply pressure $P_{in\text{-}1}$=0.69 bar. Note that the frequency range for the respective physical model curve fits spans from f_{start}=5 Hz to f_{end}=95 Hz. The majority of the physical model fits show a high correlation factor (R^2 > 0.9) over the selected frequency range (f_{start}, f_{end}).

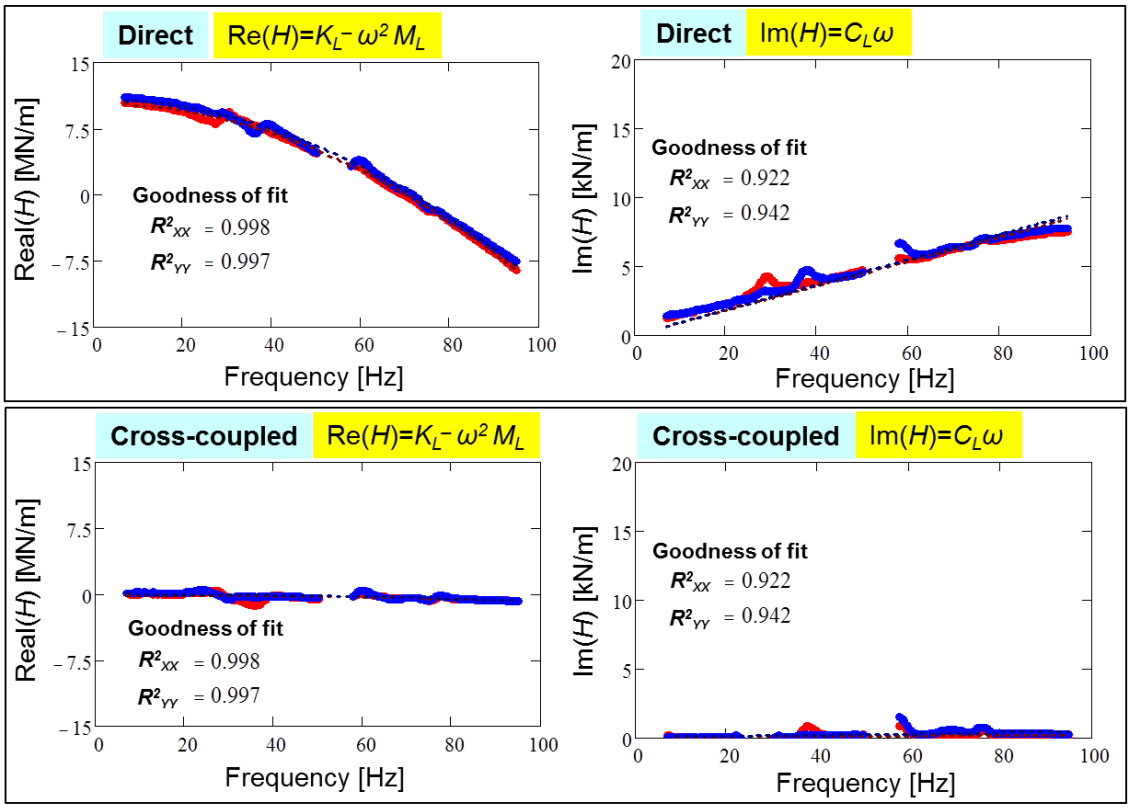

Figure 42. Real and imaginary parts of direct complex stiffness (H_{XX}, H_{YY}, H_{XY}, H_{YX}) versus excitation frequency and corresponding physical model (dash lines). α = 6.5 Hz/s. Sealed ends SFD with F_{avg}=260 N with lubricant supply pressure $P_{in\text{-}1}$=0.69 bar. End seal flow conductance $C_{ave\text{-}S1}$=0.56 LPM/bar.

Figures 43 and 44 present a comparison of the experimental direct damping and added mass coefficients versus static eccentricity (e_s/c_A) as identified from both the sine-sweep frequency dynamic loads and the single-frequency dynamic load excitations. Do notice that the SFD cross-coupled coefficient magnitudes are one order of magnitude smaller or lesser than the direct coefficients; and hereby omitted for brevity.

In general, the identified C_{SFD}, M_{SFD} coefficients versus orbit amplitude (Figure 43) and static eccentricity (Figure 44) obtained from sine-sweep frequency dynamic load tests and single frequency tests agree with each other. The SFD direct added mass coefficients (M_{XX}, M_{YY}) obtained from sine-sweep frequency dynamic load tests show a ~15% larger magnitude; however, the magnitudes are within the uncertainty (U_M~17.4%) range of the added mass coefficients for circular orbit tests.

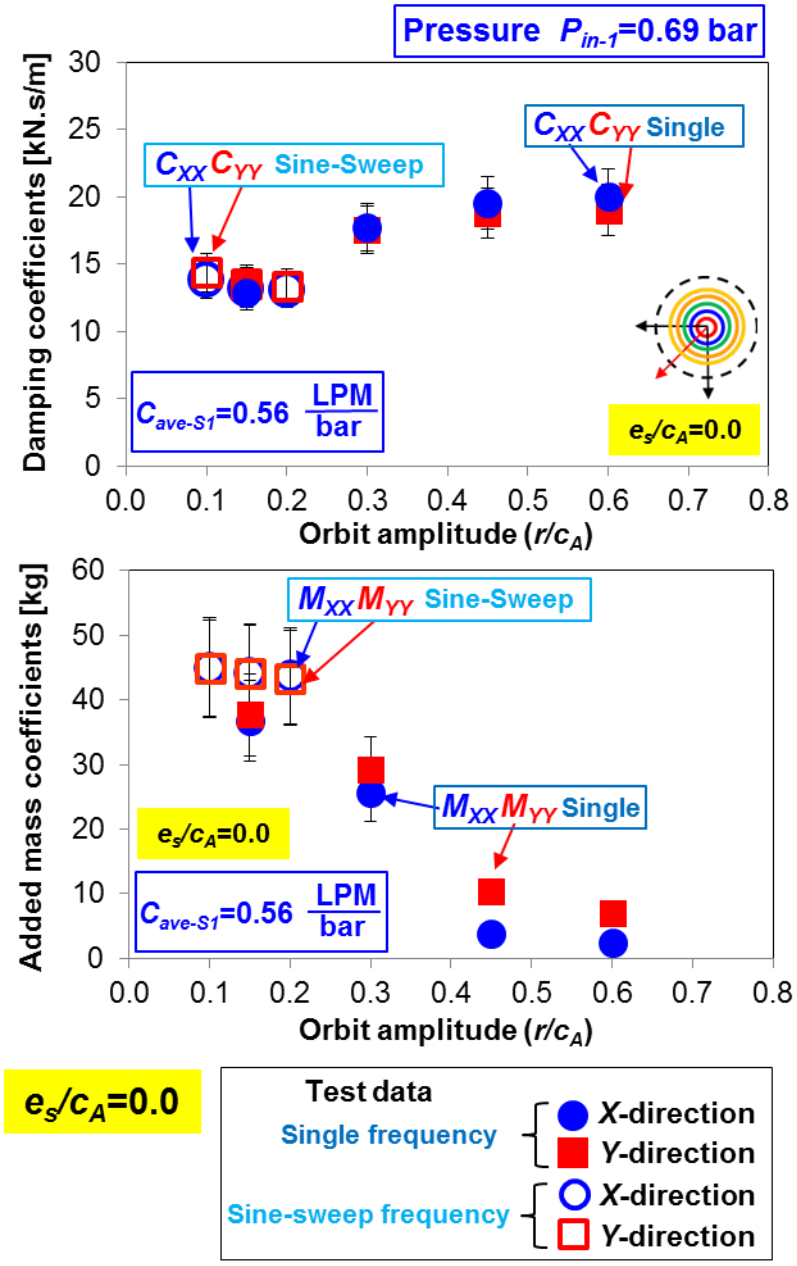

Figure 43. Sealed ends SFD direct damping (C_{SFD}) and added mass (M_{SFD}) force coefficients versus whirl orbit amplitude (r/c_A) for motions at the centered condition (e_s/c_A=0.0) and obtained from sine-sweep frequency dynamic load tests (α = 6.5 Hz/s) and single-frequency circular orbit tests. End seal flow conductance C_{ave-S1}=0.56 LPM/bar. Identification frequency range 10–100 Hz.

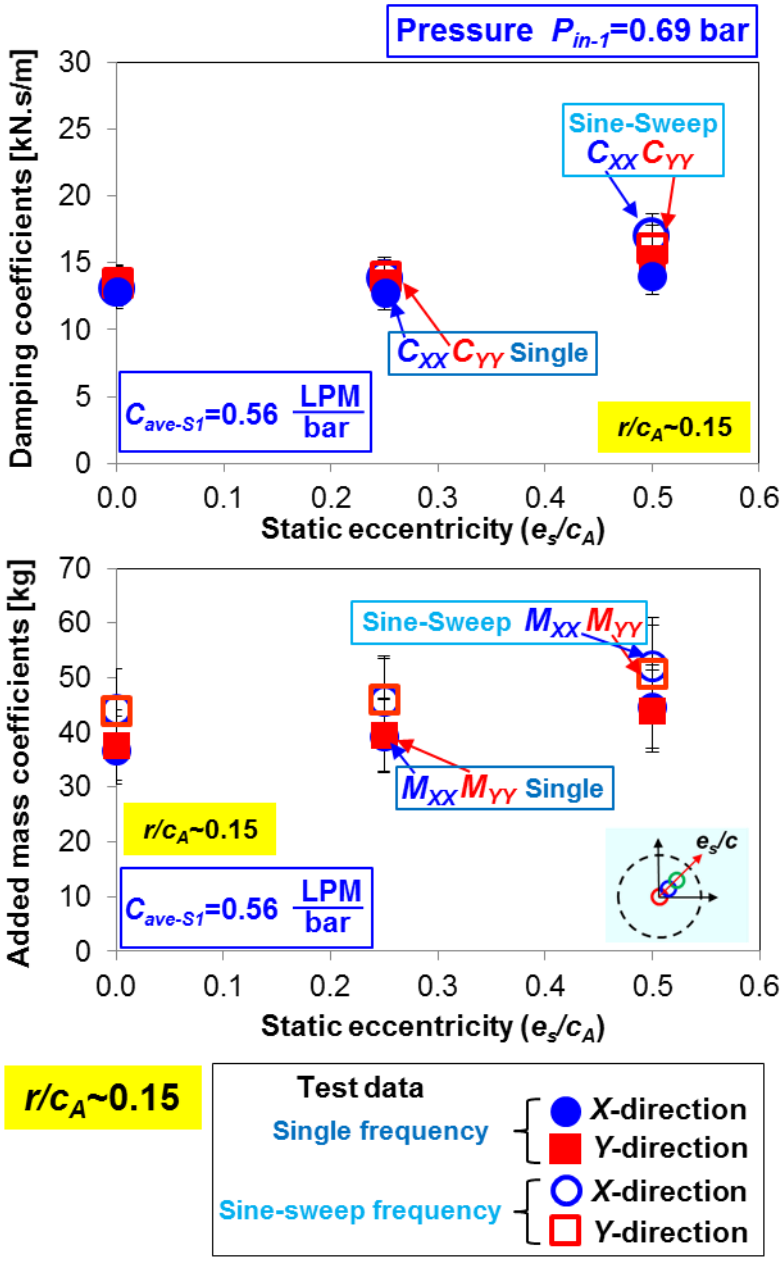

Figure 44. Sealed ends SFD direct damping (C_{SFD}) and added mass (M_{SFD}) force coefficients versus static eccentricity (e_s/c_A) for motions with whirl orbit amplitude (r/c_A=0.15) and obtained from sine-sweep frequency dynamic load tests (α= 6.5 Hz/s) and single-frequency circular orbit tests. End seal flow conductance C_{ave-S1}=0.56 LPM/bar. Identification frequency range 10–100 Hz.

Figure 45 presents the experimental SFD direct damping (C_{XX}, C_{YY})$_{\text{SFD}}$ and added mass (M_{XX}, M_{YY})$_{\text{SFD}}$ coefficients for the sealed ends SFD operating with supply pressure $P_{in\text{-}1}$~0.69 barg ($Q_{in\text{-}1}$=0.68 LPM) and also $P_{in\text{-}2}$~2.76 barg ($Q_{in\text{-}2}$=2.68 LPM). Recall that the end seal flow conductance is C_{ave-S1} =0.56 LPM/bar. The test data correspond to circular whirl motions with orbit amplitude r/c_A~0.15 and departing from static eccentricity e_s/c_A = 0.0 to 0.5. The frequency range of the sine-sweep dynamic load excitation is f=10-100 Hz and the ramp rate α=6.5 Hz/s. In both cases, the SFD damping coefficients increase with an increase in static eccentricity (e_s). A larger supply pressure $P_{in\text{-}2}$, however, provides constantly ~25% larger damping coefficients than those provided by a damper supplied with a lower pressure $P_{in\text{-}1}$. On the other hand, the inertia force coefficients for both $P_{in\text{-}1}$ and $P_{in\text{-}2}$ overlap onto each other. Recall that similar trends are observed for SFD force coefficients estimated from single-frequency operating with circular centered orbit motions e_s=0 (see Figure 22).

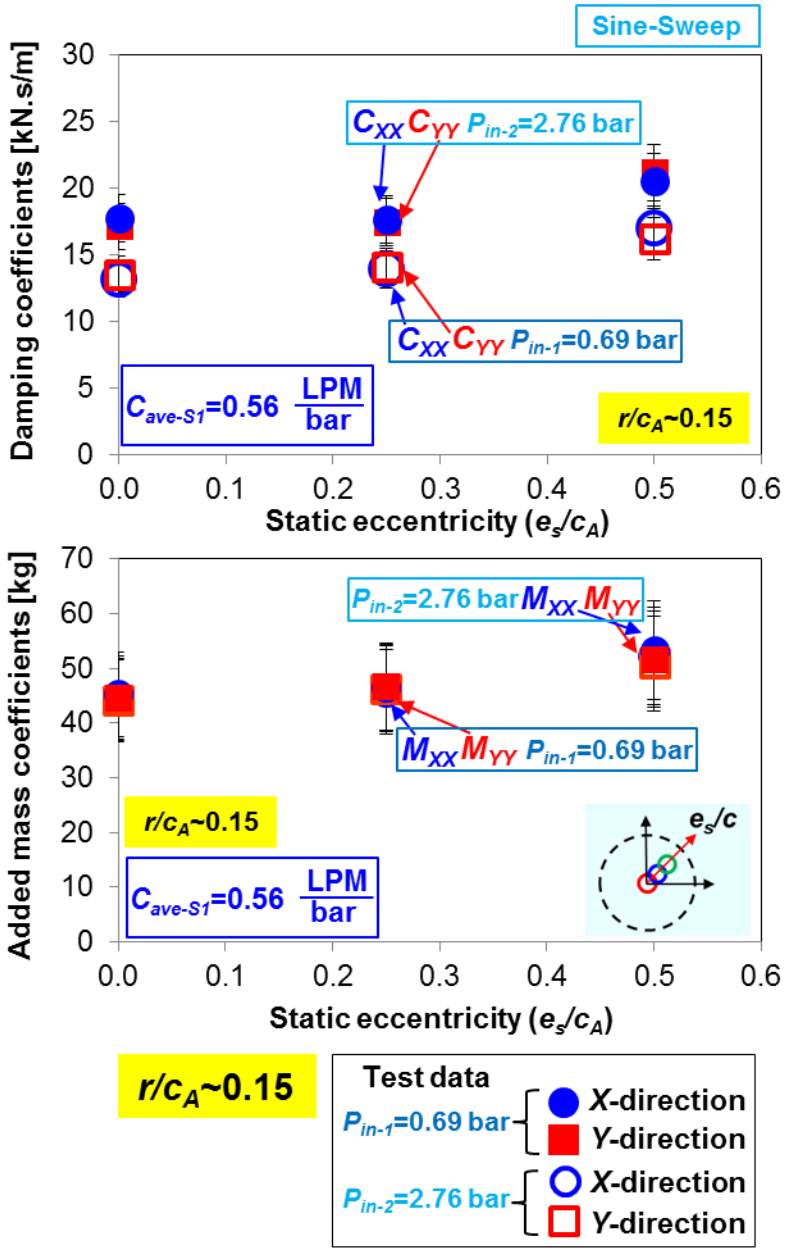

Figure 45. Effect of lubricant supply pressure: sealed ends SFD direct damping (C_{SFD}) and added mass (M_{SFD}) force coefficients versus static eccentricity (e_s/c_A) at whirl orbit amplitude (r/c_A=0.15). End seal flow conductance C_{ave-S1}=0.56 LPM/bar. Identification frequency range 10–100 Hz.

5.3. Conclusion

This section presented SFD force coefficients of a sealed ends SFD in response to a sine-sweep frequency dynamic load. Further comparisons are shown between the sine-sweep frequency dynamic load tests and single frequency dynamic loads test for sealed ends SFDs.

The estimated direct SFD damping and inertia force coefficients obtained from both sine-sweep frequency and single frequency dynamic load tests overlap onto each other within their respective uncertainty ranges. This is because of the slow angular acceleration rate (α=6.5 Hz/s) which allows the mechanical system to attain a quasi-steady state response during the sine-sweep load test. This condition ultimately enables the accurate estimation of system complex stiffnesses. Ref.[9] also describes the similar findings for tests with an open ends SFD.

The sine-sweep frequency dynamic load tests evaluate quickly the SFD force coefficients while sweeping from a low to a high excitation frequency. The single frequency load tests require multiple tests to excite the system over a range of frequencies. The experimental results conducted with a low ramp rate (α=6.5 Hz/s) provide credence to a sine-sweep frequency dynamic load test to identify the SFD force coefficients.

6. TEST SYSTEM RESPONSE DUE TO IMPACT LOADS*

6.1. Experimental Procedure

Single impact load tests are performed to quantify the effect of an impact load on the response of an elastically supported SFD. The transient response happens from either centered or off-centered conditions for both the open and the sealed ends damper configurations.

First, to perform an impact load test, one side of a steel rod stinger is detached from the BC thus the stingers are not affixed rigidly to the BC, but facing a pair of load cells located at the center of mass of the BC as shown in Figure 46. A load cell aligned with a stinger records the dynamic force ($F_{X(t)}$ or $F_{Y(t)}$) from the shakers.

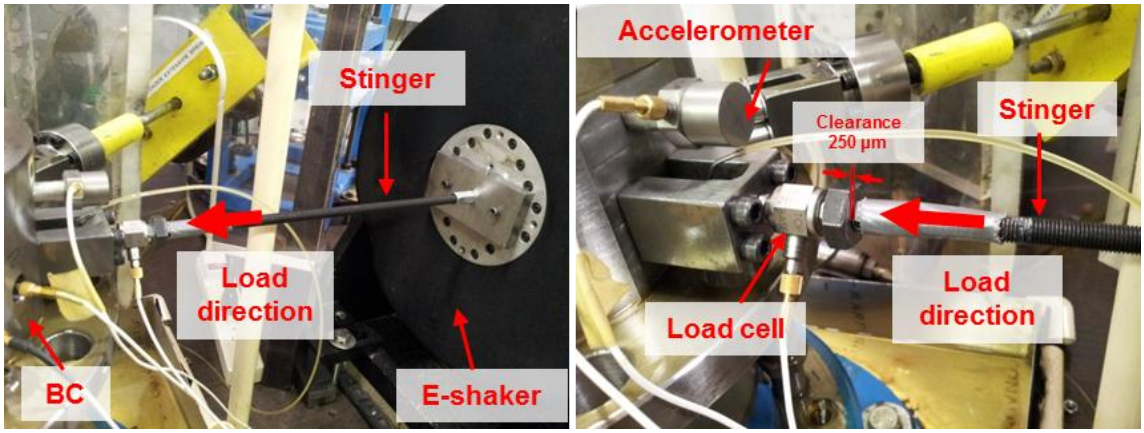

Figure 46. Photographs of stinger connection to a shaker and instrumentation set up

* Reprinted with permission from "Response of a Squeeze Film Damper-Elastic Structure System to Multiple and Consecutive Impact Loads," by San Andrés, L., and Jeung, S.-H., 2016, ASME J. Gas Turb. Pwr., 138(12), p.122504, Copyright 2016 by ASME.

Figure 47 displays a schematic view of the bearing cartridge (BC) at a statically off-centered condition. Note that with an increasing static eccentricity (e_s), the damper clearance at Θ=225° decreases; this is the location of the minimum clearance. One end of the stinger is not fastened to the load cell mounted on the BC and the free end stinger travels 0.254 mm (10 mil) before imposing a dynamic load on the BC.

Table 7 summarizes the operating conditions for single impact load tests performed on the open ends SFD and sealed ends SFD for motions departing from the journal center. Figure 48 depicts isometric views of the bearing cartridge (BC) and journals for the configurations detailed in Table 7. Again, note that the lubricant inlet flow rate (Q_{in}) and pressure (P_{in}) are chosen to be comparable with those in prior tests in Ref.[3].

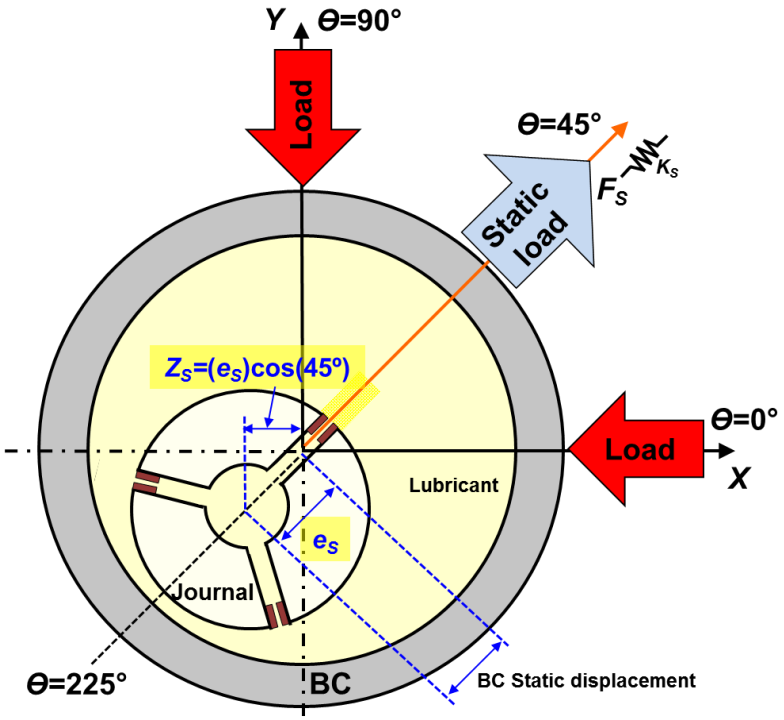

Figure 47. Schematic view of BC statically displaced (e_s) relative to a stationary journal (Exaggerated film clearance for illustrative purposes) [10].

Table 7. Test conditions for single impact loads.

Impact load								
Damper Config.	Radial clearance, c(mm)	End condition	Duration of impact, t_{IMP} (ms)	Peak impact load, F_{MAX}/LD (bar)	Static eccentricity, e_s/c	Inlet flow rate, Q_{in} (LPM)	Static inlet Pressure, P_{in} (bar(g))	Seal conductance, $C_{ave\text{-}S}$ (LPM/bar)
A	0.254	Sealed	1.3	1.6, 3.1, 4.7, 6.2	e_s/c_A = 0.0	0.68	0.69	0.56
				1.6, 3.1, 4.7, 6.2	e_s/c_A = 0.25			
				1.6, 3.1, 4.7, 6.2	e_s/c_A = 0.5			
		Open		1.6, 3.1, 4.7, 6.2	e_s/c_A = 0.0	5.03	0.35	-
				1.6, 3.1, 4.7, 6.2	e_s/c_A = 0.25			
				1.6, 3.1, 4.7, 6.2	e_s/c_A = 0.5			
B	0.267	Open [10]		1.5, 2.4, 3.1, 4.7, 6.2, 7.8	e_s/c_C = 0.0	5.21	0.34	-

*Number of averaged impacts' sets: 15

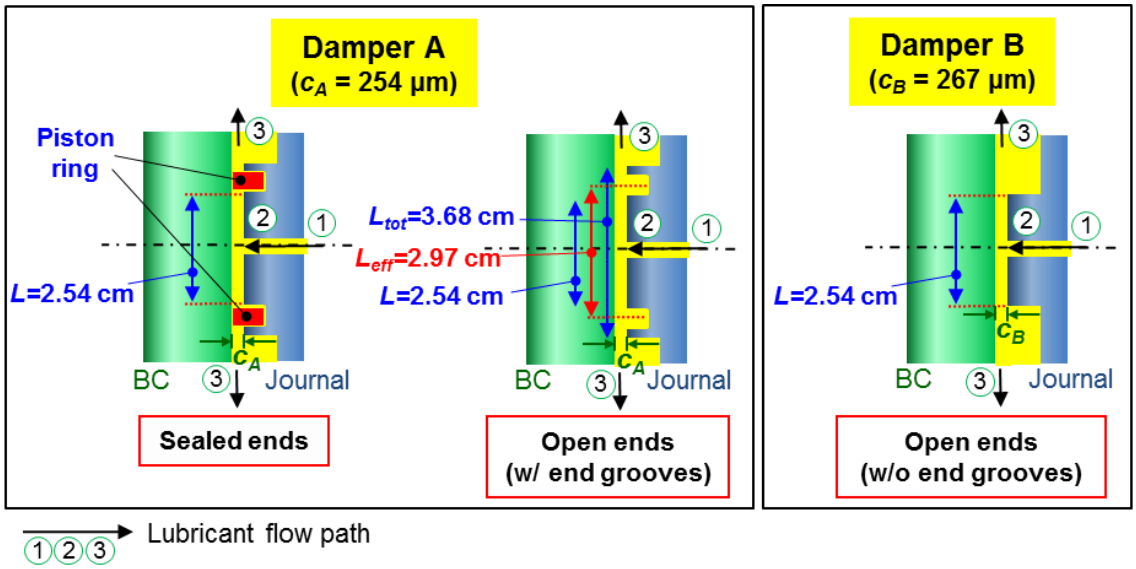

Figure 48. Cross-section views of two test squeeze film dampers. Damper A: (a) sealed ends and (b) open ends with end grooves for piston rings. Damper B [10]: (c) open ends without end grooves.

In each set, fifteen single impact loads are delivered along the X direction while no dynamic load is applied along the Y direction. Next, the same process is conducted with the load delivered along the Y direction. The load sets include impact forces with a peak magnitude from 0.5 kN to 2.0 kN ($F_{MAX}/(LD)$=1.6 – 6.2 bar). The shaker controller in a data acquisition program (DAQ) records the system transient response of applied force (F_X, F_Y), displacement (Z_X, Z_Y) and BC acceleration (a_X, a_Y) at a rate of 16,384 samples/s during a time span of 0.25 s. The displacements (Z_X, Z_Y) are relative to the journal.

The following results present the measured peak BC displacement (Z_{MAX}) that includes both the static and dynamic displacements, i.e.

$$Z_{MAX} = Z_S + Z_{MAX}^{dyn} \tag{21}$$

where the BC static eccentricity (e_s) has components along the X and Y directions as shown in Figure 47, $Z_{s_{X,Y}} = e_s \cos\left(\frac{1}{4}\pi\right)$.

6.2. Experimental Results

Figure 49 depicts the trace of an impact load delivered to the BC along the X direction and the ensuing BC displacement (Z_X) for tests conducted with both open and sealed ends SFDs, respectively. The test data correspond to impacts with an increase in peak load amplitude $F_{MAX}/(LD)$=1.6 – 6.2 bar. The impact load, resembling a half-sine wave, lasts ~ Δt_{IMP}= 1.3 ms. The response of the BC is characterized as oscillatory with an exponentially decaying envolope. For brevity, only the results for test along the X direction are shown (typically, the BC motions for both X and Y directions show similar

results). Expectedly, the transient response of the BC for the sealed ends SFD shows a smaller maximum BC amplitude and decays faster than that of an open ends SFD.

Figure 50 depicts the maximum BC displacement $\bar{Z}_{MAX}/c = \left[\bar{Z}_{MAX}^{dyn} + Z_s\right]/c$ versus the peak amplitude of the impact load ($\bar{F}_{MAX}$ / LD) applied along the X or Y directions for motions initiating from static eccentricity e_s/c_A=0.0, 0.25, and 0.5. Let

$$\frac{\bar{Z}_{MAX}^{dyn}}{c} = \frac{1}{c}\left\{\frac{1}{n}\sum_{i=1}^{n}\left[Z_{MAX}^{dyn}\right]_i\right\},\ \frac{\bar{F}_{MAX}}{LD} = \frac{1}{LD}\left\{\frac{1}{n}\sum_{i=1}^{n}\left[F_{MAX}\right]_i\right\} \tag{22}$$

Each symbol in the graphs represents the average of transient responses collected from n=15 separate impacts.

The dashed lines show a linear regression fit, which for most conditions, evidences a proportional relationship between the maximum BC displacement $\left(\bar{Z}_{MAX}^{dyn}\right)$ and the peak impact load, that is, $\dfrac{\bar{Z}_{MAX}^{dyn}/c}{\bar{F}_{MAX}/(LD)} \to \beta$ is nearly constant. A large load forces the BC towards a large (dynamic) amplitude. Z_{MAX}/F_{MAX} appears to be smaller with sealed ends damper compared to open ends. Again, this indicates that with same amount of applied unit load, the peak displacement is smaller for sealed ends damper. Most notably, for both open and sealed ends dampers, increasing the static eccentricity (e_s) of the SFD causes no significant difference in the slope (β).

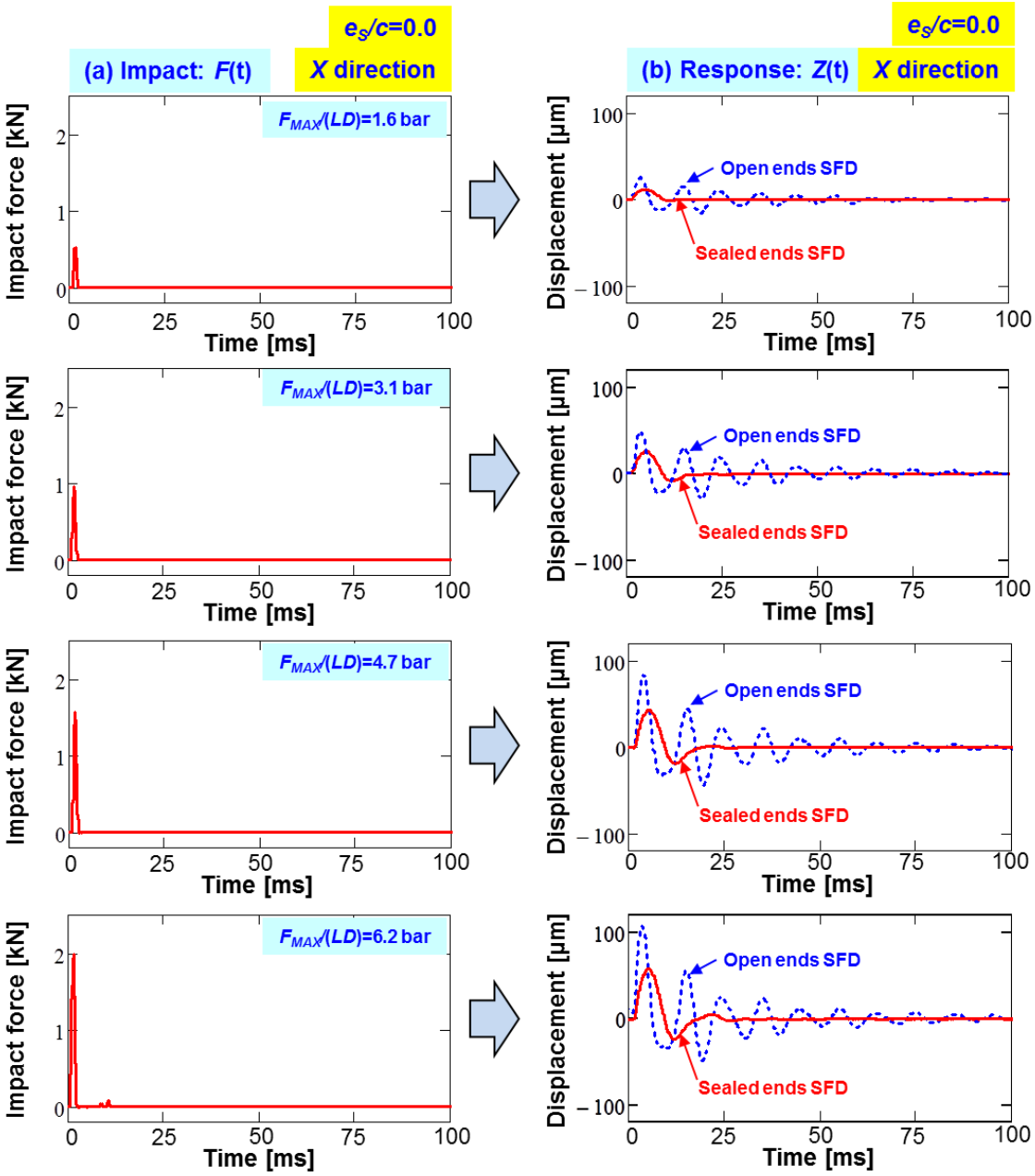

Figure 49. Impact load along *X* direction and BC dynamic displacement Z_X versus time. Test at centered condition (e_S=0.0*c*). Single impact load $F_{MAX\text{-}X}/(LD)$=1.6 – 6.2 bar. Open ends and sealed ends SFDs with clearance c_A=0.254 mm.

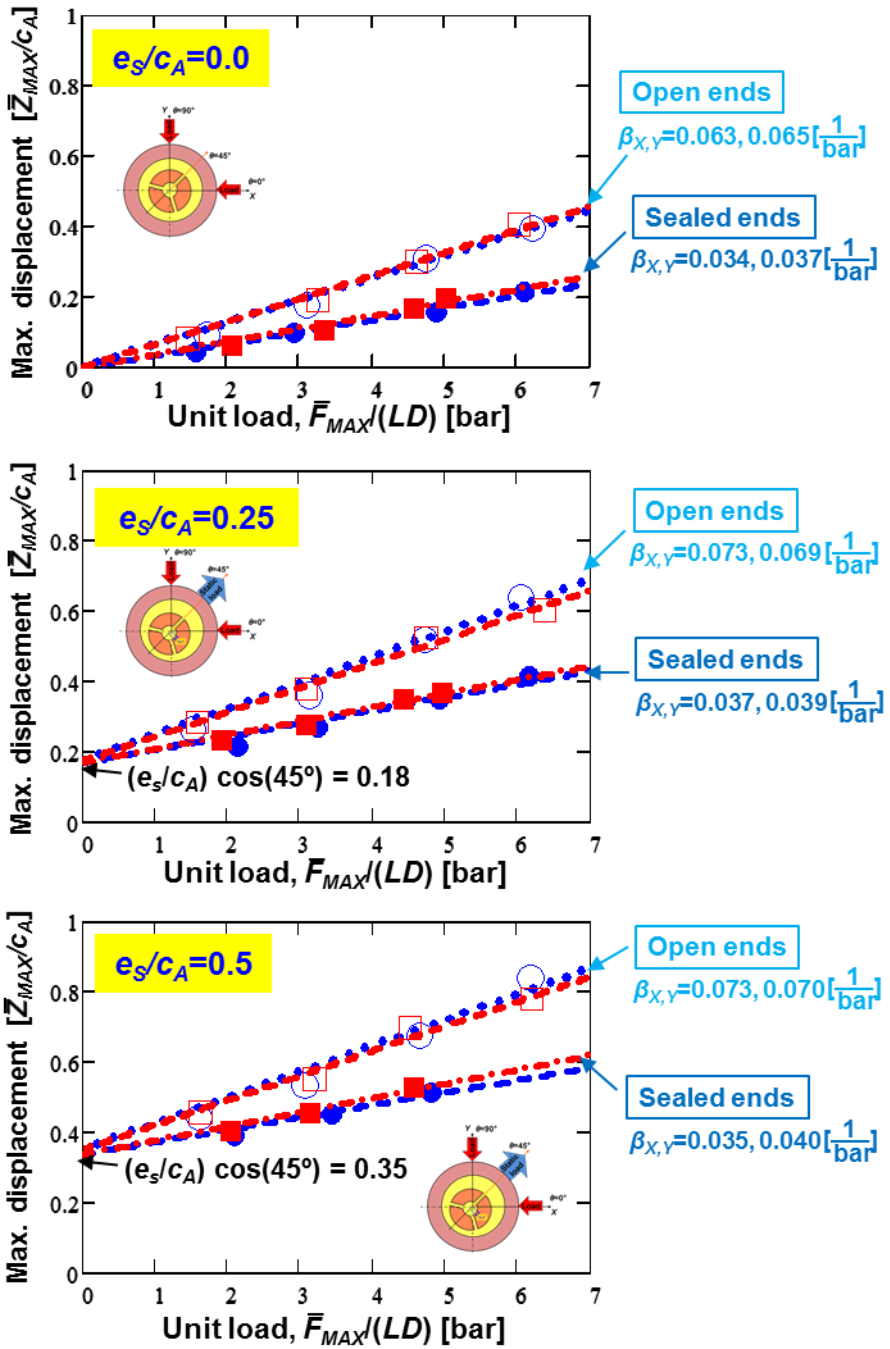

Figure 50. Maximum displacement Z_{MAX}/c_A vs. peak amplitude of applied single impact load $F_{MAX}/(LD)$ for motions initiating from static eccentricity e_s/c=0.0, 0.25, and 0.5. Open ends and sealed ends SFDs with clearance c_A=0.254 mm. β[1/bar] = slope of line fit to data.

Figure 51 shows β, the peak BC amplitude $(\left(\bar{Z}_{MAX}^{dyn}\right)/c)_{X,Y}$ over unit load ($\bar{F}_{MAX} / LD$), versus static eccentricity (e_s/c_A). The data correspond to results from a single impact load for both open and sealed ends SFDs for motions initiating from static eccentricity e_s/c_A=0.0, 0.25, and 0.5. β appears to be constant with increasing static eccentricity albeit the open ends damper shows twice larger β than that for the sealed ends. Ref.[10] details the estimation of variability V~±14%.

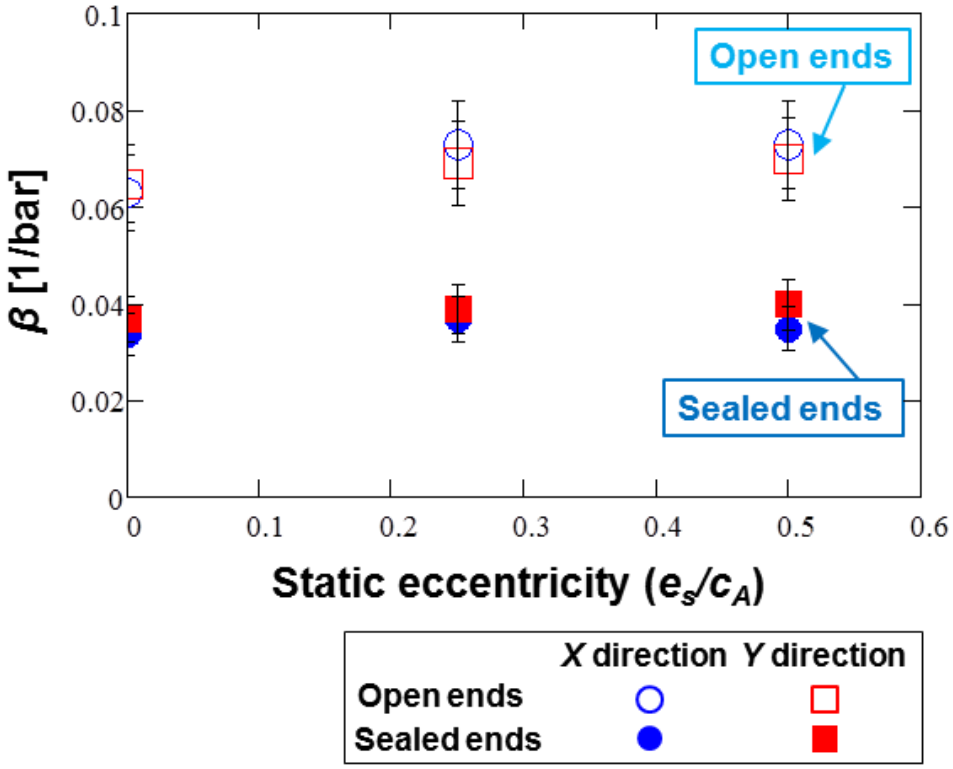

Figure 51. $\beta=\frac{Z_{MAX}/c_A}{F_{MAX}/(LD)}$: Peak displacement Z_{MAX}/c_A over peak amplitude of unit load $F_{MAX}/(LD)$ vs. static eccentricity e_s/c_A=0.0, 0.25, and 0.5. Open ends SFD and sealed ends SFD with clearance c_A=0.254 mm.

As shown in Figure 49, the BC response to a delivered impact load decays exponentially, which is typical of a viscous under-damped system. From this BC response, a well-known equation for the logarithmic decrement (δ) identifies the system log dec (δ) or subsequently the system damping ratio ξ. Deriving log dec δ from the ratio of two peak displacement amplitudes separated by N periods of motion [57] follows

$$\delta = \frac{1}{N}\ln\left(\frac{Z_k}{Z_{k+N}}\right) = \frac{2\pi\xi}{\sqrt{1-\xi^2}} = \xi\omega_n\tau_d \tag{23}$$

Eqn. (24) is based on the transient free-response of an underdamped (ξ<1) one degree of freedom mechanical system, where $\xi = \frac{C}{2\sqrt{K_S M}}$ is the damping ratio and $\omega_n = \sqrt{\frac{K_S}{M}}$ is the system natural frequency. Above, $M = M_{BC} + M_{SFD}$, where M_{BC}=15.15 kg and M_{SFD} is the SFD added mass, and K_S = 12.0 MN/m is the support structural stiffness.

Figure 52 shows the displacement transient response overlaid with the damping envelope curve ($e^{-\xi\omega_n t}$). The data corresponds to unidirectional impact loads with $F_{MAX}/(LD)$=1.6 bar on open ends and sealed ends SFD for motions initiating from the centered condition (e_s=0). For a better comparison of all the presented test results, the BC displacements are normalized with respect to the BC maximum peak amplitude, (Z/Z_{MAX}). Hence, the maximum normalized displacement is equal to one. Expectedly, the BC transient response for the sealed ends SFD decays faster than that of open ends SFD. A curve fit on the six peaks for open ends and three peaks for sealed ends in the recorded transient response estimates the logarithmic decrement (δ). The majority of the line fits ($e^{-\xi\omega_n t}$) show a high correlation factor (R^2>0.9) indicating the physical viscous damping

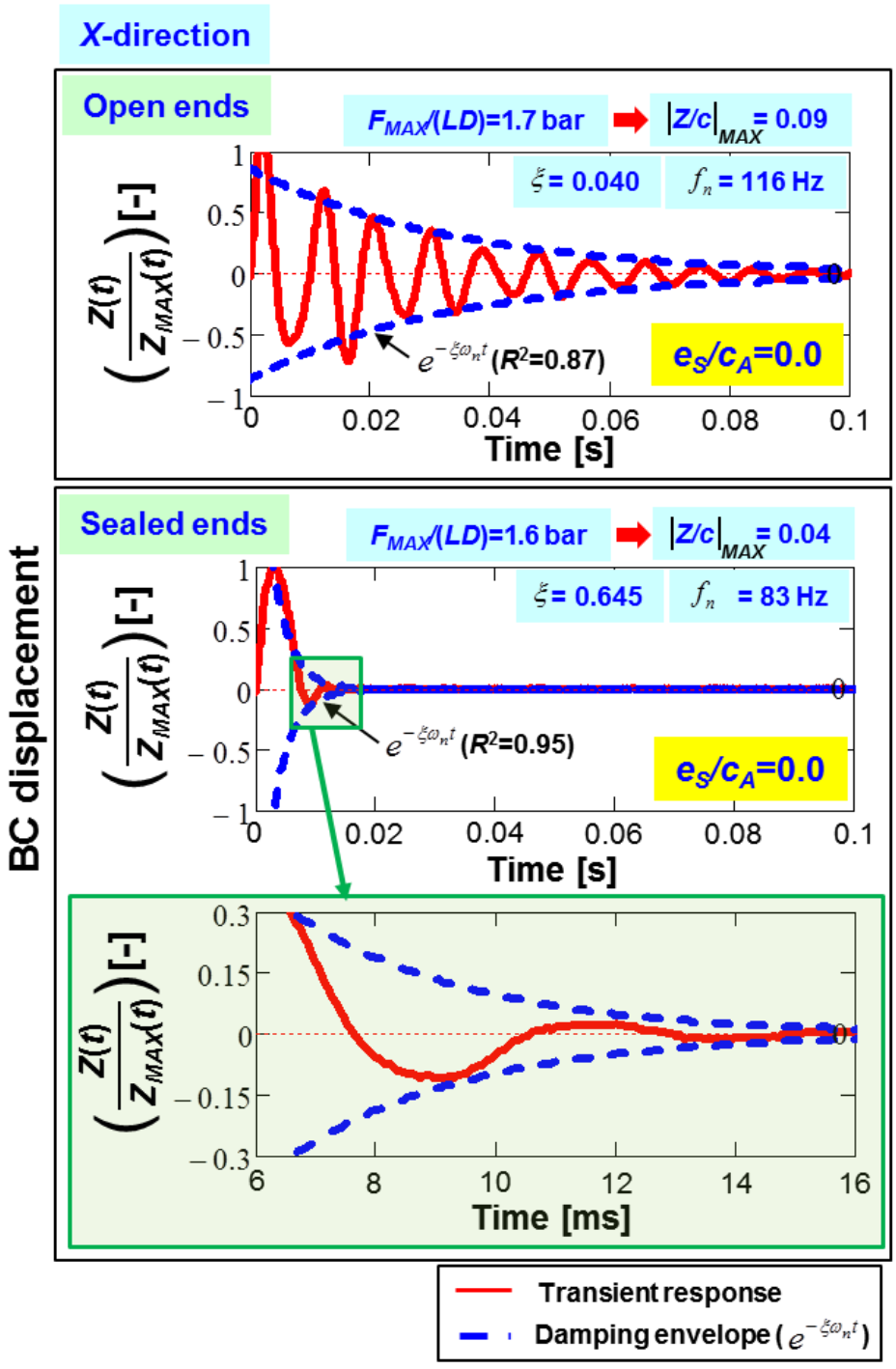

Figure 52. Dimensionless BC displacement $Z/Z_{MAX\text{-}X}$ and damping envelope ($e^{-\xi\omega_n t}$) versus time (t). Measurements for $F_{MAX\text{-}X}/(LD)$=1.6 bar for motions from e_s/c_A=0. Open ends SFD and sealed ends SFD with clearance c_A=0.254 mm.

model is adequate to represent the transient response of the test SFD subject to a single impact load.

Figure 53 (note the logarithmic scale) shows the estimated test system damping ratio (ξ) obtained for the sealed ends SFD and the open ends SFD versus the maximum dynamic displacement (Z_{MAX}/c_A). The test data correspond to a single impact on the SFD and motion departing from static eccentricity e_s=0.0c_A, 0.25c_A, and 0.5c_A. Recall that Z_{MAX} includes the static displacement $Z_S=e_s\cdot\cos(\pi/4)$, see Eqn. (22), depicted with dashed (vertical) lines on the Figure.

Both sealed ends and open ends dampers show an increase in damping ratio (ξ) with an increase in peak displacement ($\bar{Z}_{MAX}^{dyn}$) and the static eccentricity (e_s). The sealed ends SFD provides ten to fifteen more damping ratio (ξ) than the open ends configuration, i.e., the end seals enable the BC response to decay faster when subject to an impact load. Appendix F further presents the comparison of damping ratios between the open ends dampers A and B. In brief, the estimated SFD damping ratio for the small film clearance (c_A) damper is ~1.6 times larger than the damping ratio (ξ) obtained with a larger clearance (c_B) damper.

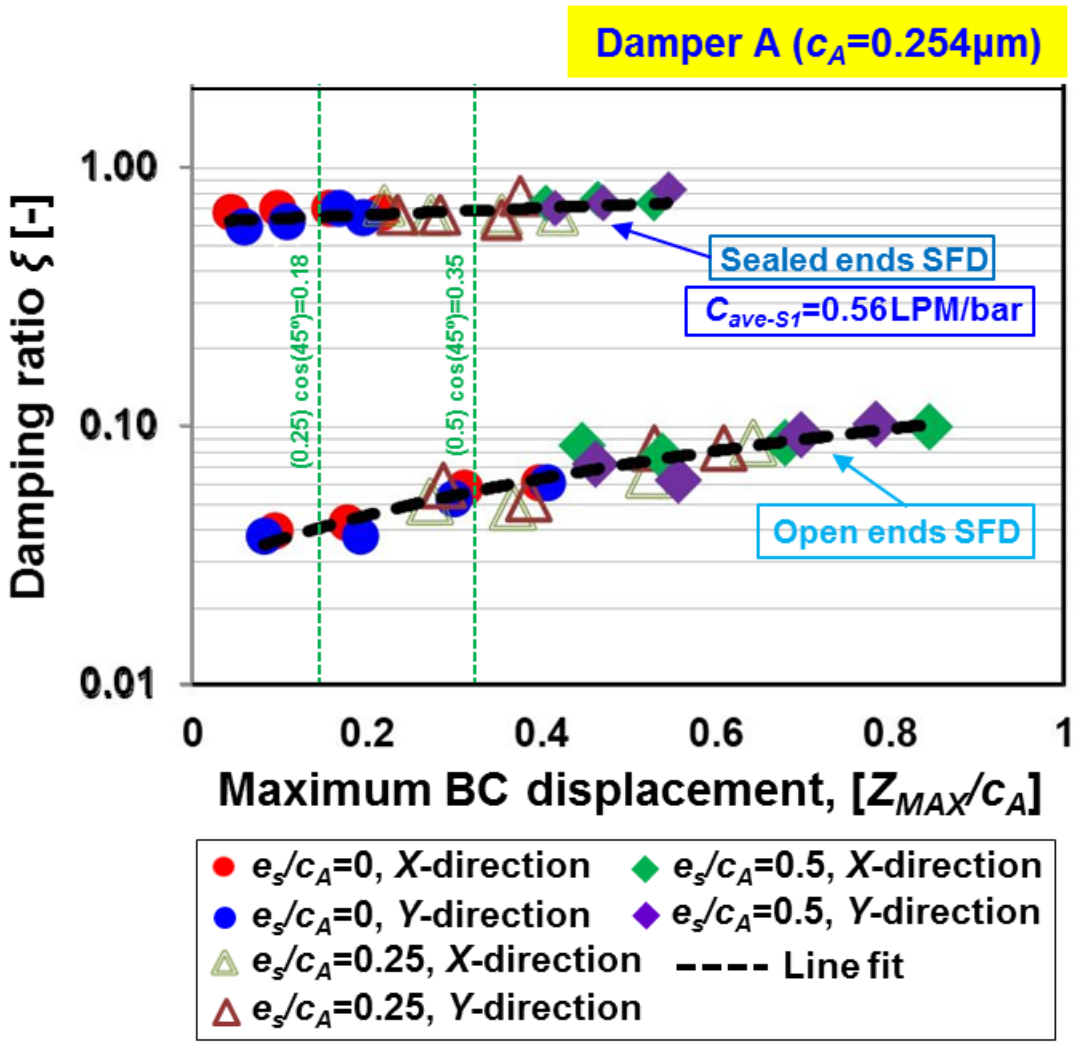

Figure 53. System damping ratio (*ξ*) and logarithmic decrement (*δ*) versus peak BC (Z_{MAX}/c) displacement. Data for one impact load and motions departing from various static eccentricity. Open ends SFD and sealed ends SFD with c_A=0.254 mm (*L*/*D*=0.2). End seal flow conductance C_{ave-S1}=0.56 LPM/bar.

6.3. Conclusion

This section presented the experimental results due to a sudden impulsive (impact) load that produce transient BC displacements extend prior work in Ref.[10] on the same SFD test rig with an open ends SFD and a sealed ends SFD. Both SFDs have same geometry except for the end seals. These experiments serve to characterize a sealed ends SFD experiencing stringent operating conditions such as a shock load.

The SFD transient response decays faster with the sealed ends damper, i.e., it has a larger logarithmic decrement. The damping ratio (ζ) derived from a single impact load shows an increases with the peak displacement $Z_{MAX}= Z_{MAX}^{dyn} + Z_s$. Interestingly enough, $\bar{Z}_{MAX}^{dyn}$ appears linear with respect to the maximum dynamic impact load $\bar{F}_{MAX}$ for both open and sealed ends dampers. $\bar{Z}_{MAX}^{dyn} / \bar{F}_{MAX}$ decreases by just ~46% with the sealed end damper configuration whereas the sealed ends SFD provides ten to fifteen times larger damping ratio than the open ends configuration.

7. SUMMARY AND CONCLUSIONS

The dissertation, consolidating measurements and analyses of the dynamic forced performance obtained with an open ends and a sealed ends SFDs, delivers quantitative and qualitative assessments of the two damper configurations.

As SFDs are not an off-the-shelf mechanical element, a damper should be designed with the rotor-bearing system into consideration. Hence, a firm understanding of SFD performance with respect to its geometry, sealing devices, and operating conditions is important to achieve efficient designs that lower cost and save space and weight. These considerations are critical in the aircraft industry.

The dissertation presents comprehensive dynamic load tests for the open and sealed ends SFDs that allow characterizing the SFD due to single frequency, sine-sweep frequency dynamic loads and to an impact load. This work complements a multiple year research work on SFDs published in Refs.[3,5,6,7,8,9,10,11]. The experimentally identified force coefficients from either single or sine-sweep frequency dynamic loads allow performing a rotordynamic analysis. Furthermore, the test results for impact loads on a sealed ends SFD provide engineers credence to determine the performance of a SFD during transient events such as an aircraft hard landing and takeoff.

The major conclusions drawn in this work are:

(i) Measurements of single frequency dynamic load tests for open and sealed ends SFDs

a. <u>Effect of lubricant supply pressure on PR sealed ends SFD force coefficients</u>:

For the sealed ends SFD, upon increasing the lubricant supply pressure by four times ($P_{in\text{-}1}$~0.69→$P_{in\text{-}2}$~2.76 barg), both the damping and added mass coefficients increase by ~26%. This is attributed to the large supply pressure $P_{in\text{-}2}$ preventing the onset of oil cavitation in the film land and thus generating a larger peak-peak dynamic pressure.

b. Effect of flow conductance on PR sealed ends SFD Force coefficients:

At a fixed lubricant supply pressure $P_{in\text{-}1}$~0.69 barg, two PR sealed ends SFDs, whose seal conductances are C_{ave-S1} and C_{ave-S2} (C_{ave-S2} =1.6 C_{ave-S1}), show nearly identical damping and added mass coefficients. This is because both PRs fit tightly (C_{ave-s} < 1 LPM/bar).

c. Comparison between open and sealed ends dampers A:

SFD direct damping coefficients are 11-13 times greater for the sealed end damper than those for the open ends SFD. For the ends sealed damper, direct added masses are ~two times greater (~38 kg) than the bearing cartridge actual mass (M_{BC}=15.2 kg) and ~11 times greater than the fluid added mass estimated for the open-ends damper. Disregarding the influence of SFD added mass coefficient (~38 kg) may lead to a large discrepancy in the placement of critical speeds in a typical rotor-bearing system.

d. Comparison between predictions and experimental results

Numerical predictions from a computational program [7] agree well with the experimental damping while under predicting the inertia coefficients by ~30% for motions at small whirl amplitude r/c_A=0.15. The discrepancy may due to the physical model representing the PR as a local end seal that ignores the pressure distortions created by the local exit flow through the PR slit.

(ii) Measurements of sine-sweep frequency dynamic load tests for sealed ends SFDs

e. Experiments with a sine-sweep frequency dynamic load confirmed the findings made in Ref.[9]; namely the SFD force coefficients obtained with a low rate of change in excitation frequency (α) agree with the force coefficients obtained from multiple single-frequency dynamic loads spanning the same frequency range.

f. Most importantly, the sine-sweep technique substantially saves time to identify force coefficients compared to multiple single frequency dynamic load tests.

(iii) Measurements of single impact load tests for open and sealed ends SFDs

g. The SFD transient response decays faster with both large amplitude applied impact load (F) and when departing from a high static eccentricity (e_s).

h. Similarly, the damping ratio (ξ) derived from a single impact load increases linearly with the peak displacement $Z_{MAX}= \bar{Z}_{MAX}^{dyn} + Z_s$.

i. The sealed ends SFD provides ten to fifteen more damping ratio than the open ends configuration. $\bar{Z}_{MAX}^{dyn} / \bar{F}_{MAX}$ decreases ~46% with the sealed end damper configuration compared to open ends damper.

REFERENCES

[1] San Andrés, L., 2012, "Squeeze Film Dampers: Operation, Models and Technical Issues," *Modern Lubrication Theory*, Notes 13, Texas A&M University Digital Libraries, http://oaktrust.library.tamu.edu/handle/1969.1/93253 [06/27/2016]

[2] Vance, J., Zeidan, F., Murphy, B., 2010, *Machinery Vibration and Rotordynamics*, "Bearings and Their Effect on Rotordynamics", Chapter 5, John Wiley & Sons, Inc., New York, pp. 216-238.

[3] San Andrés, L., Jeung, S.-H., Den, S., and Savela, G., 2016, "Squeeze Film Dampers: An Experimental Appraisal of Their Dynamic Performance," *Proceedings of the 2016 Asia Turbomachinery & Pump Symposium*, Marina Bay Sands, Singapore. (http://atps.tamu.edu/proceedings/2016-atps-proceedings)

[4] Zeidan, F. Y., Vance, J. M., and San Andrés, L., 1996 ''Design and Application of Squeeze Film Dampers in Rotating Machinery,'' *Proceedings of the* 25th *Turbomachinery Symposium*, Texas A&M University, Houston, TX, pp. 169–188.

[5] Jeung, S.-H., San Andrés, L., and Bradley, G., 2016, "Forced Coefficients for a Short Length, Open-Ends Squeeze Film Damper with End Grooves: Experiments and Predictions," ASME J. Gas Turb. Pwr., **138**(2), p. 032502.

[6] San Andrés, L., and Jeung, S.-H., 2015, "Response of a Squeeze Film Damper to Large Amplitude Impact Loads," 2015 STLE Annual Meeting & Exhibition, May 18-21, Dallas, TX, USA.

[7] San Andrés, L., and Jeung, S.-H., 2016, "Orbit-Model Force Coefficients for Fluid Film Bearings: A Step Beyond Linearization," ASME J. Gas Turb. Pwr., **138**(2), p. 022502.

[8] San Andrés, L., and Jeung, S.-H., 2015, "Experimental Performance of an Open Ends, Centrally Grooved Squeeze Film Damper Operating with Large Amplitude Orbital Motions," ASME J. Gas Turb. Pwr., **137**(3), p. 032508.

[9] San Andrés, L., Den, S., and Jeung, S.-H., 2016, "Transient Response of a Short-Length (*L/D*=0.2) Open-Ends Elastically Supported Squeeze Film Damper: Centered and Largely Off-Centered Whirl Motions," ASME J. Gas Turb. Pwr., **138**(12), p.122503.

[10] San Andrés, L., and Jeung, S.-H., 2016, "Response of a Squeeze Film Damper-Elastic Structure System to Multiple and Consecutive Impact Loads," ASME J. Gas Turb. Pwr., **138**(12), p.122504.

[11] San Andrés, L., Den, S., and Jeung, S.-H., 2017, "On The Force Coefficients of A Flooded, Open End Short Length Squeeze Film Damper: From Theory To Practice (And Back)," *Proceedings of the 2017 ASME Turbo Expo*, Charlotte, NC, ASME Paper No. GT2017-63152.

[12] Childs, D., 2013, *Turbomachinery Rotordynamics with Case Studies*, Minter Spring Pubs., TX, Chapter 6.

[13] Cooper, S., 1963, "Preliminary Investigation of Oil Films for Control of Vibration," *Proceedings of Lubrication and Wear Convention*, IMechE, pp. 305-315.

[14] Della Pietra, L., and Adiletta, G., 2002, "The Squeeze Film Damper Over Four Decades of Investigations. Part I: Characteristics and Operating Features," Shock Vib. Dig., **34**(1), pp. 3–26.

[15] Adiletta, G., and Della Pietra, L., 2002, "The Squeeze Film Damper Over Four Decades of Investigations. Part II: Rotordynamics Analysis with Rigid and Flexible Rotors," Shock Vib. Dig, **34**(2), pp. 97–126.

[16] Smith, D. M., 1964, "Journal Bearing Dynamic Characteristics—Effect of Inertia of Lubricant," Proc. Inst. Mech. Eng., **179**(10), pp. 37–44.

[17] Reinhardt, F., and Lund, J. W., 1975, "The Influence of Fluid Inertia on the Dynamic Properties of Journal Bearings," ASME J. Lubr. Technol., **97**(1), pp. 154-167.

[18] San Andrés, L., 1985, "Effects of Fluid Inertia Effect on Squeeze Film Damper Force Response," Ph.D. Dissertation, Texas A&M University, College Station, TX.

[19] Tichy, J.A., 1984, "Measurements of Squeeze-Film Bearing Forces and Pressures, Including the Effect of Fluid Inertia," ASLE Trans., **28**(1), pp. 520-526.

[20] Tichy, J.A., 1987, "A Study of the Effect of Fluid Inertia and End Leakage in the Finite Squeeze Film Damper," ASME J. Tribol., **109**(1), pp. 54-59.

[21] Tichy, J., and Bou-Said, B., 1991, "Hydrodynamic Lubrication and Bearing Behavior with Impulsive Loads", STLE Tribol. Trans., **34**(4), pp.505-512.

[22] Zhang, J., and Roberts, J. B., 1996, "Force Coefficients for a Centrally Grooved Short Squeeze Film Damper," ASME J. Tribol., **118**(3), pp. 608–616.

[23] Gehannin, J., Arghir, M., and Bonneau, O., 2010, “Complete Squeeze-Film Damper Analysis Based on the “Bulk Flow” Equations,” STLE Tribol. Trans., **53**(1), pp. 84–96.

[24] Diaz, S., and San Andrés, L., 2001, "Air Entrainment Versus Lubricant Vaporization in Squeeze Film Dampers: An Experimental Assessment of Their Fundamental Differences," ASME J Gas Turb Pwr, **123**(4), pp. 871-877.

[25] Levesley, M., and Holmes, R., 1996, “The Effect of Oil Supply and Sealing Arrangements on the Performance of Squeeze-Film Dampers: An Experimental Study,” Proc. Inst. Mech. Eng., Part J: J. Eng. Tribol., **210**(4), pp. 221–232.

[26] Kim, K., and Lee, C., 2005, “Dynamic Characteristics of Sealed Squeeze Film Damper with a Central Feeding Groove,” ASME J. Tribol., **127**(1), pp. 103–111.

[27] Miyachi, T., Hoshiya, S., Sofue, Y., Matsuki, M., and Torisaki, T., 1979, “Oil Squeeze Film Dampers for Reducing Vibration of Aircraft Gas Turbine Engines,” ASME Paper No. 79-GT-133.

[28] De Santiago, O., and San Andrés, L., 1999, “Imbalance Response and Damping Force Coefficients of a Rotor Supported on End Sealed Integral Squeeze Film Dampers,” ASME Paper No. 99-GT-203.

[29] Meng, G., San Andrés, L., and Vance, J., 1991, “Experimental Measurement of the Dynamic Pressure and Force Response of a Partially Sealed Squeeze Film Damper,” Proceedings of the 13th Biennial Conference on Mechanical Vibration and Noise, Miami, FL, September 22–25, Rotating Machinery and Vehicle Dynamics, ASME, **35**, pp. 251–256.

[30] Defaye, C., Arghir, M., and Bonneau, O., 2006, "Experimental Study of the Radial and Tangential Forces in a Whirling Squeeze Film Damper," STLE Tribol. Trans., **49**(2) pp. 271-278.

[31] San Andrés, L., and Seshagiri, S., 2013, "Damping and Inertia Coefficients for Two End Sealed Squeeze Film Dampers with a Central Groove: Measurements and Predictions," ASME J. Gas Turb. Pwr., **135**(12), p. 112503.

[32] San Andrés, L., 2012, "Damping and Inertia Coefficients for Two Open Ends Squeeze Film Dampers With a Central Groove: Measurements and Predictions," ASME J. Gas Turb. Pwr., **134**, p. 102506.

[33] Delgado, A., and San Andrés, L., 2010, "A Model for Improved Prediction of Force Coefficients in Grooved Squeeze Film Dampers and Oil Seal Rings," ASME J. Tribol., **132**(3), p. 032202.

[34] San Andrés, L., and Delgado, A., 2012, "A Novel Bulk-Flow Model for Improved Predictions of Force Coefficients in Grooved Oil Seals Operating Eccentrically," ASME J. Gas Turb. Pwr., **134**, p. 052509.

[35] Stallone, M.J., Gallardo, V., Storace, A.F., Bach, L.J. and Black, G., 1983, "Blade Loss for Transient Dynamic Analysis of Turbomachinery", AIAA J. **21**(8), pp. 1134–1138.

[36] Zhang, S. P., Yan, L. T., and Li, Q. H., 1991, "Development of Porous Squeeze Film Damper Bearings for Improving the Blade Loss Dynamics of Rotor-Support Systems," ASME J. Vib., Acoust., **114**, pp. 347–353.

[37] Walton, J. F., and Heshmat, H., 1993, "Rotordynamic Evaluation of an Advanced Multi-Squeeze Film Damper-Imbalance Response and Blade-Loss Simulation," ASME J. Gas Turb. Pwr., **115**, pp. 347-352.

[38] Sun, G., Palazzolo, A., Provenza, A., Lawrence, C., and Carney, K., 2008, "Long Duration Blade Loss Simulations Including Thermal Growths for Dual-Rotor Gas Turbine Engine," J. Sound Vib., **316**, pp. 147–163.

[39] Hori, Y, Kato, T., 1990, "Earthquake-Induced Instability of a Rotor Supported by Oil Film Bearings," ASME J. Vibr. Acoust., **112**, pp.160–165.

[40] Roberts, J. B., Holmes, R., and Mason, P. J., 1986 "Estimation of Squeeze-Film Damping and Inertial Coefficients from Experimental Free-Decay Data," Proceedings of the Institution of Mechanical Engineers, Engineering Sciences Division, **200**(2C), pp. 123-133.

[41] Ramli, M. D., Roberts, J. B., and Ellis, J., 1987, ″Determination of Squeeze Film Dynamic Coefficients from Experimental Transient Data,″ ASME J. Tribol., **109**, pp. 155–163.

[42] Lee, A., Kim, B., and Kim, Y., 2006, "A Finite Element Transient Response Analysis Method of a Rotor-Bearing System to Base Shock Excitations Using the State-Space Newmark Scheme and Comparisons With Experiments," J. Sound Vib., **297**(3–5), pp. 595–615.

[43] Tiwari, R., Lees, A.W., Friswell, M.I., 2004, "Identification of Dynamic Bearing Parameters: A Review," Shock Vib. Dig., **36**(2), pp. 99-124.

[44] Fritzen, C. P., 1985, “Identification of Mass, Damping, and stiffness Matrices of Mechanical System,” ASME J. Vib., Acoust., **108**, pp. 9-16.

[45] Rouch, K., 1990, “Experimental Evaluation of Squeeze Film Damper Coefficients with Frequency Domain Techniques,” STLE Tribol. Trans., **33**(1), pp. 67-75.

[46] Lund, J. W., Myllerup, C. M., and Hartmann, H., 2003, “Inertia Effects in Squeeze-Film Damper Bearings Generated by Circumferential Oil Supply Groove,” ASME J. Vib. Acoust., **125**(4), pp. 495–499.

[47] Hassini, M. A., and Arghir, M., 2014, “A New Approach for the Stability Analysis of Rotors Supported by Gas Bearings,” ASME J. Gas Turb. Pwr., 136, p. 022504.

[48] Hassini, M. A., and Arghir, M., 2015, “A Simplified and Consistent Nonlinear Transient Analysis Method for Gas Bearing: Extension to Flexible Rotors,” ASME J. Gas Turb. Pwr., **137**, p. 092502.

[49] Den, S., 2015, “Analysis of Force Coefficients and Dynamic Pressures for Short-Length (L/D=0.2) Open-Ends Squeeze Film Dampers,” M.S. Thesis, Texas A&M University, College Station.

[50] San Andrés, L., 2014, “Force Coefficients for a Large Clearance Open Ends Squeeze Film Damper With a Central Groove: Experiments and Predictions,” Tribol. Int., **71**, pp. 17–25.

[51] San Andrés, L., 2012, "Liquid Cavitation in Fluid Film Bearings" *Modern Lubrication Theory,* Notes 6, Texas A & M University Digital Libraries, http://oaktrust.library.tamu.edu/handle/1969.1/93246 [06/27/2016]

[52] Xing, C., and Braun, M., 2010, "Experimental Investigation of the Development of Cavitation in a Squeeze Film Damper," Proceedings of the STLD/ASME 2010 International Joint Tribology Conference, San Francisco, CA, October 17-20, IJTC2010-41144, pp. 1-3.

[53] Diaz, S.E., and San Andrés, L., 2001, "Air Entrainment Versus Lubricant Vaporization in Squeeze Film Dampers: An Experimental Assessment of Their Fundamental Differences," ASME J. Gas Turb. Pwr., **123**(4), pp. 871-877.

[54] Marmol, R. A., and Vance J. M., 1978, "Squeeze Film Damper Characteristics for Gas Turbine Engine", ASME J. Tribol., **100**, pp. 139–146.

[55] Lang, G., F., 1997, "Electrodynamic Shaker Fundamentals," J. Sound and Vibration, April.

[56] Lang, G., F., and Snyder, D., 2001, "Understanding the Physics of Electrodynamic Shakers," J. Sound and Vibration, October.

[57] Ginsberg, J. H., 2001, *Mechanical and Structural Vibration – Theory and Application*, John Wiley & Sons, New York, pp. 79–85.

[58] "Mobil Velocite™ No 3 (ISO VG 2) Manufacturer specification sheet", Hydraulic oils Typical Properties, Mobil, Accessed October 2013, http://www.mobil.com/USAEnglish/Lubes/PDS/GLXXENINDMOMobil_Velocite_Oil_Numbered.aspx

[59] "NI cDAQ – 917x User Manual," User manual for NI CompactDAQ9171/9174/9178 USB Chassis, National Instruments, July 2011, Appendix A. Specifications.

[60] Beckwith, T., Marangoni, R., and Lienhard, J. 1993, *Mechanical Measurements*, Prentice Hall, New York.

[61] Coleman, H.W., and Steele, G.W., 1998, *Experimentation and Uncertainty Analysis for Engineers*, John Wiley & Sons, New York.

[62] Booker, J. F., 1965, "A Table of the Journal-Bearing Integral," ASME J. Basic Eng., **87**(2), pp. 533–535.

[63] San Andrés, L. A., and Vance, J. M., 1987, "Effects of Fluid Inertia on Finite Length Squeeze-Film Dampers," ASLE Transactions, **30**(3), pp. 384-393.

APPENDIX A

DESCRIPTION OF TEST SYSTEM AND COMPONENTS

This section provides a description of the journal, the bearing cartridge (BC) and the test rig components.

a) Journal

Figure A.1 shows a photograph of a feed orifice of diameter ϕ = 2.5 mm machined into a hexagonal socket bolt inserted in the journal. The design minimizes the discontinuity in the film land area around the lubricant inlet. The small socket holds ~0.13 cm^3 in volume. Hence, the three orifices contain about ~15% of the lubricant volume in the film land, πDLc_A=2.57 cm^3 for damper A [5]. Note that the journal has a central through hole that acts as a lubricant flow path.

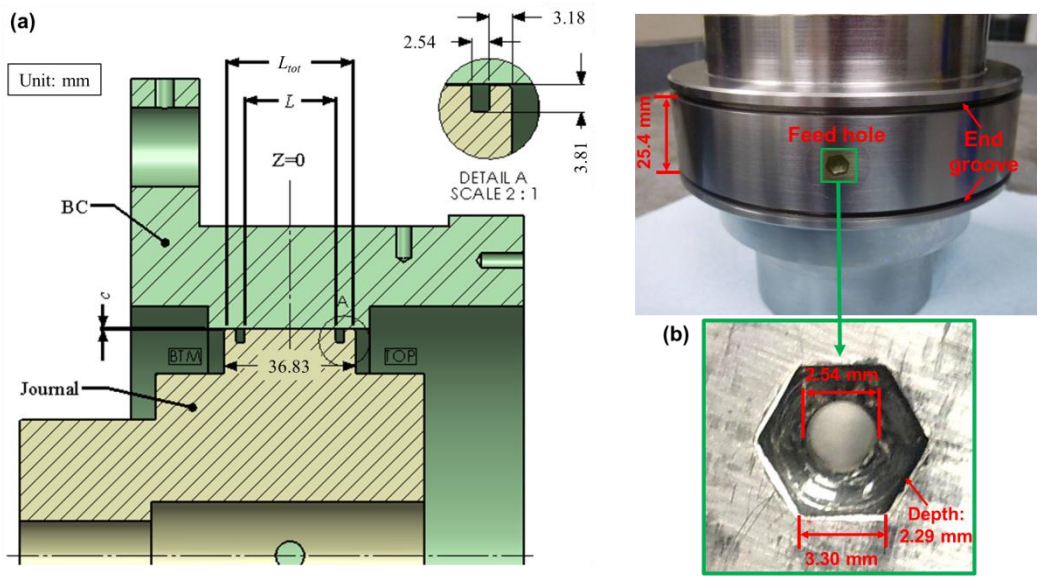

Figure A.1. (a) Cross-section of SFD journal and BC showing the film land length *(L)* and side end grooves and lip sections. Total wetted length L_{tot} noted. Photograph of (b) test journal (Material: AISI 1018 carbon steel) and (c) its feed orifice with hex socket [5].

b) Bearing Cartridge

Figure A.2 depicts views of the bearing cartridge (BC). The BC does not have a central groove and the inner surface of the BC creates the outer surface of the squeeze film land with uniform thickness axially. The BC interfaces with four support rods and accommodates instrumentation including REBAM® sensors, load cells, accelerometers and pressure sensors.

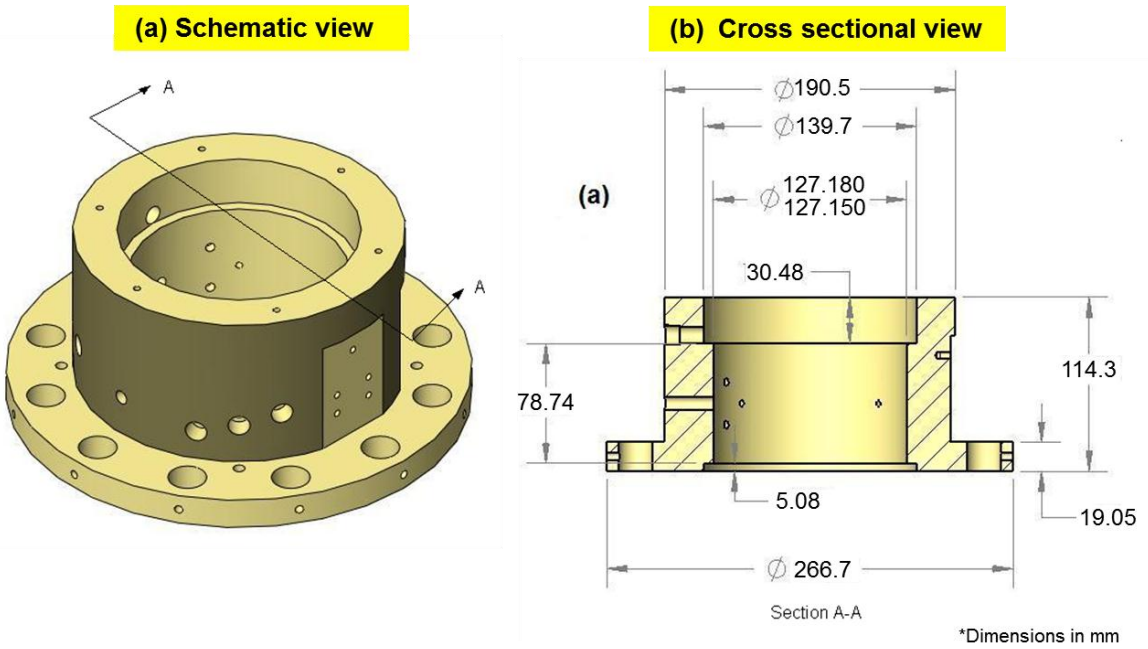

Figure A.2. Bearing cartridge (a) isometric view, and (b) cross sectional view. (Material: AISI 1018 carbon steel)

c) Measurement of journal outer diameter

The radial clearance of the squeeze film damper is a critical design value. Half of the difference between the journal outer diameter and the BC inner diameter is the nominal clearance. A micrometer (uncertainty ±2.54 μm (0.1 mil) measures the specified axial

planes and angles of the journal and BC as shown in the Figure A.3. Table A.1 lists the measured outer diameter of the journal at each plane and measurements of the BC inner diameter. Note that the micrometer and bore gauge are based on the English unit. The average SFD radial clearance is

$$\boldsymbol{c_A = \tfrac{1}{2}(D_{BC\_ID} - D_{J\_OD}) = 254\ \mu m\ (10\ mil) +/-\ 10\ \mu m}$$

The average clearance agrees with the design value 10.0 mil. However, note that the journal OD at the axial mid plane (A2) has a bulge ~1.2 mil (0.03 mm) larger than the OD top plane (A1) and ~2.4 mil (0.06 mm) larger than the bottom plane (A3). Hence, the clearance axial profile is not as uniform as expected. That is, the average radial clearance at the top, mid and bottom planes equal 10.0 mil (0.254 mm), 9.4 mil (0.239 mm) and 10.6 mil (0.269 mm), respectively.

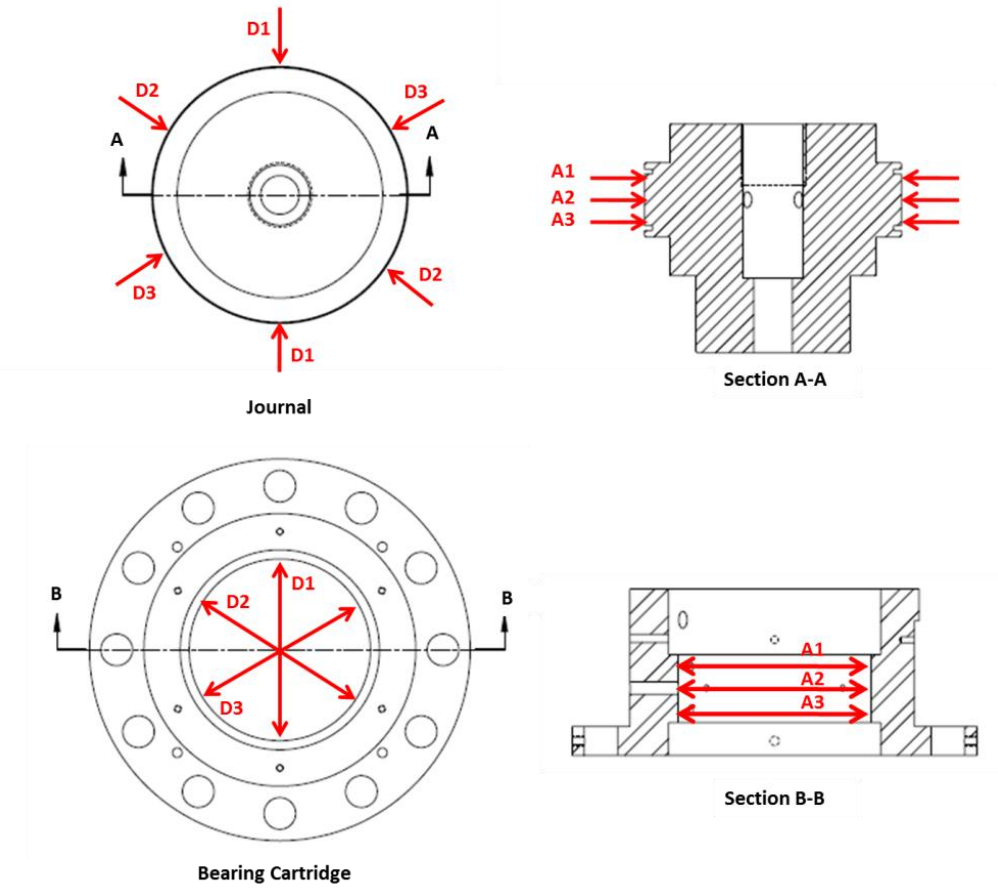

Figure A.3. Measurement planes for journal outer diameter and BC inner diameter (D planes are radial lines with constant spacing of 45º apart)

Table A.1. Journal outer diameter measured at three axial planes and three radial lines.

Measurement Plane	A-1 (Top) [mm (in)]	A-2 (Mid) [mm (in)]	A-3 (Btm) [mm (in)]
D1 (0-deg)	126.659 (4.9866)	126.695 (4.9880)	126.629 (4.9854)
D2 (60-deg)	126.665 (4.9868)	126.695 (4.9880)	126.634 (4.9856)
D3 (120-deg)	126.647 (4.9861)	126.675 (4.9872)	126.619 (4.9850)
Average	126.657 (4.9865)	126.686 (4.9877)	126.627 (4.9853)
Total Grand Average:		126.657 (4.9865)	mm (in)
Total Uncertainty: +/-		0.010 (0.0004)	mm (in)

Bearing cartridge ID (average) = 127.165 mm (5.0065 in)

Measurement Plane	Radial Clearance [mm (in)]
A-1 (Top)	0.254 (0.0100)
A-2 (Mid)	0.239 (0.0094)
A-3 (Btm)	0.269 (0.0106)
Average Clearance	0.254 (0.0100)

APPENDIX B

MEASUREMENT OF LUBRICANT PHYSICAL PROPERTIES

The SFD test rig uses ISO VG 2 grade oil as its lubricant. A Brookfield DV-E rotary viscometer measures the viscosity of a lubricant by measuring the shear (drag) stress on a rotating spindle fully submerged in a lubricant bath. In the apparatus, a water jacket heated the vessel holding the lubricant. The ASTM standard viscosity-temperature relation is

$$\mu = \mu_R e^{-\alpha_v (T - T_R)} \tag{B.1}$$

where μ_R = 2.60 cPoise (0.377 micro-Reyn) is the measured viscosity at room temperature (T_R = 23ºC). The oil viscosity coefficient, α_v, is given as

$$\alpha_v = \frac{-\ln(\mu_2 / \mu_R)}{(T_2 - T_R)} = 0.016 \frac{1}{^\circ C} \tag{B.2}$$

where μ_2 and T_2 are the last viscosity and temperature measurements, respectively.

Figure B.1 shows the current and previous measurements of lubricant viscosity along with the ASTM standard curve fit. The ASTM standard viscosity-temperature relation for the current measurements shows high correlation (R^2=0.997). The viscosity measurements throughout 2014 to 2016 show the similar results. Routine inspection of lubricant density and viscosity ensure no significant changes in lubricant properties have occurred.

The measurements give 2.4 cSt (1.90 cPoise) at 40°C whereas the lubricant manufacturer specifies 2.0 cSt (1.60 cPoise) at the same temperature (see Table B.1).

The difference, amounting to ~16%, is most likely due to entrapped air in the lubricant from numerous tests performed using the identical oil tank during the past research programs. Note that a 10% of entrained air (volume) can increases viscosity by up to 15%. In addition, the blend of multiple batches of the same lubricant brand purchased at various times could also explain the difference in viscosity.

At ambient condition of 23°C, the lubricant density was also determined, by weighing a known volume of lubricant oil. The oil density obtained is ρ=800 kg/m^3.

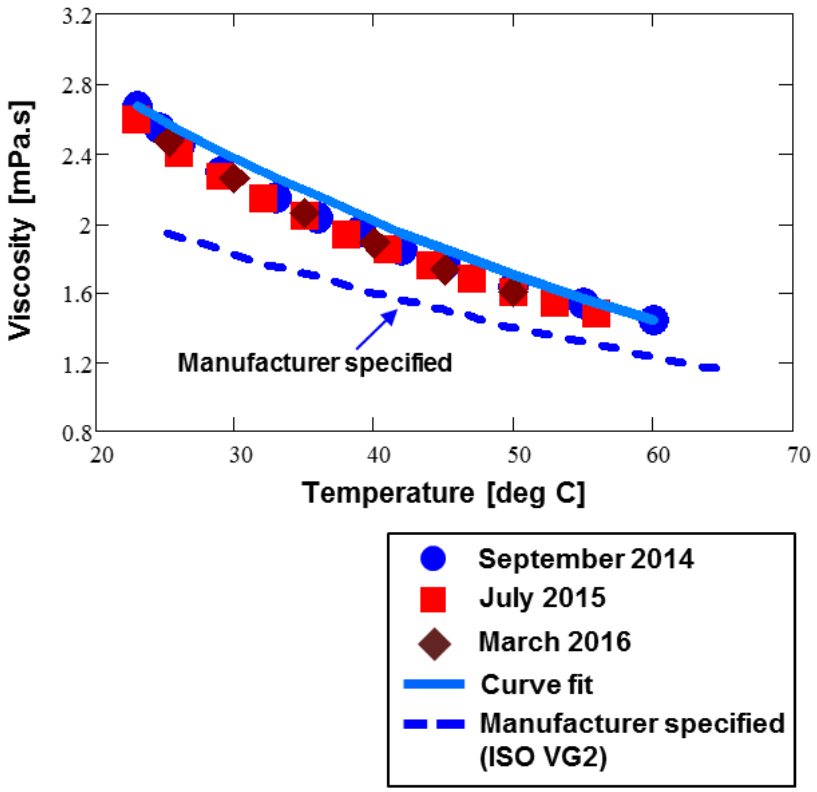

Figure B.1. ISO VG 2 measured viscosity versus temperature for three separate measurements.

Table B.1. Mobil Velocite™ No 3 (ISO VG 2) Manufacturer specification [58]

Mobil Velocite Oil Numbered Series No 3 (ISO VG 2)	
cSt @ 40ºC	2.1
cSt @ 100ºC	0.95
Pour Point, ºC	-36
Flash Point, ºC	84
Density @ 15º C, kg/L	0.802

APPENDIX C

EXAMPLES OF PREDICTED OPEN ENDS SQUEEZE FILM STATIC PRESSURE PROFILES

For open ends SFD with a supply condition $P_{in\text{-}3}$~0.35 barg ($Q_{in\text{-}3}$=5.03 LPM), Figure C.1 displays the predicted static pressure field in the film land. The journal is centered (e_s=0) and without external excitation (r/c=0, ω=0 Hz). The damper axial length and circumferential extent are modeled by 6 and 121 elements, respectively. The static pressure at the oil feed holes is P_{in}, and the pressure drops towards the open ends (0 barg) and circumferentially in between the holes. Unlike dampers with a deep circumferential groove, the film static pressure is near ambient (~0 barg) almost everywhere in the film because the damper clearance is large. Note that the land region at a low static pressure is more susceptible to lubricant gaseous cavitation, particularly for large amplitude journal motions r and at high whirl frequencies ω (high squeeze velocity = $r\omega$).

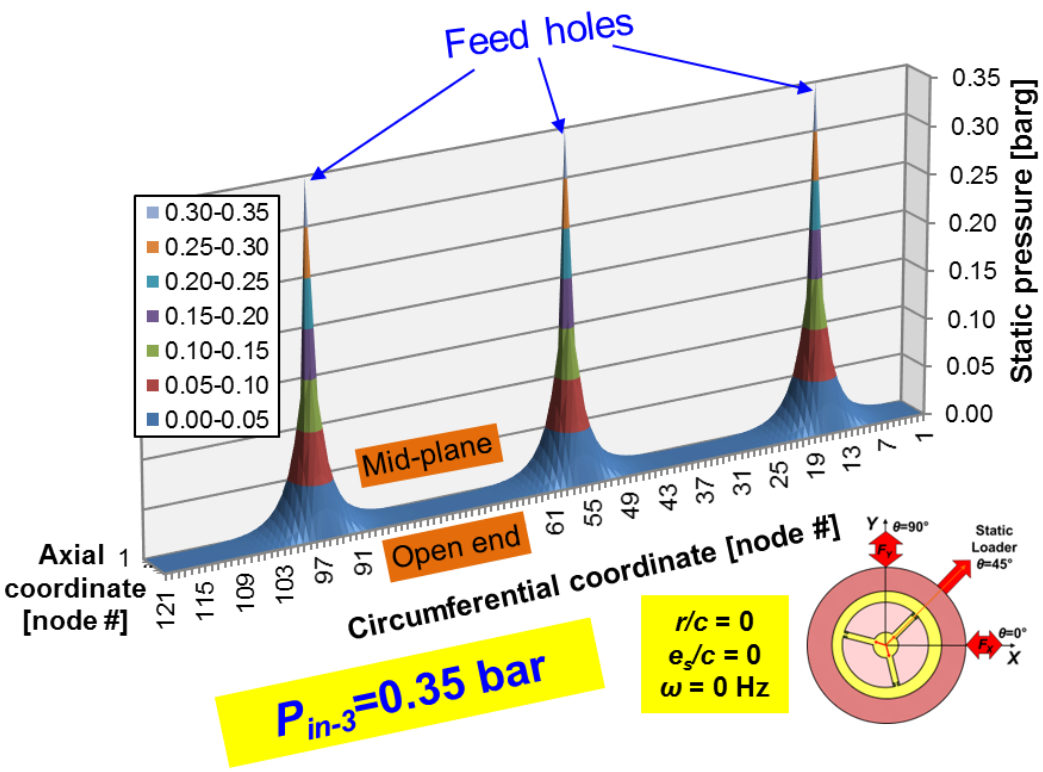

Figure C.1. Predicted static pressure field in open ends SFD with c_A=254 μm. Centered static position (e_s=0). Lubricant supply pressure $P_{in\text{-}3}$=0.35 bar.

APPENDIX D

IDENTIFICATION OF (DRY) TEST SYSTEM STRUCTURE PARAMETERS

Circular orbit load tests are performed with a dry system (without lubricant) to identify the test system structural parameters [structural stiffness (K_s), system remnant mass (M_s), and structural damping (C_s)]. Two electromagnetic shakers deliver single frequency loads, 90º out of phase, over a designated frequency range of 10 – 100 Hz. The amplitude of journal motion is set to r/c_A=0.05.

The Instrumental Variable Filter (IVF) method [44] estimates the force coefficients for the dry system (K_s, C_s, M_s) from the mechanical impedances

$$H_{XX,YY} = [K_s - \omega^2 M_s + i\omega C_s]_{XX,YY} \tag{C.1}$$

where ω is the excitation frequency. Note that the real and imaginary parts of an impedance (H),

$$\mathrm{Re}(H) = K_s - \omega^2 M_s \quad \text{and} \quad \mathrm{Im}(H) = C_s \omega \tag{C.2}$$

reveal the structural stiffness (K_s) and system remnant mass (M_s) and an (assumed) viscous damping coefficient (C_s).

Table D.1 lists the identified test system structural parameters (K_s, C_s, M_s) over a excitation frequency range from f_{start}=10 to f_{end}=100 Hz. The results show the test system is orthotropic with little structural cross-coupling. The structure stiffnesses are K_{SX}=12.0 MN/m and K_{SY}=11.9 MN/m along the X and Y directions..

The damping ratios are < ~4%, which are typical of steel structures. However, note that the damping is most likely not viscous in nature, as Fig. D.1 depicting the imaginary part of the test impedances, Im(H), most vividly demonstrates.

Note that an accurate measurement of the structural stiffness is required to distinguish the SFD reaction forces from the reaction forces arising from the support structure; albeit the SFD dynamic force coefficients are independent of the structural stiffness of the BC [3].

Figure D.1 shows the experimental data and physical model fits in real and imaginary parts of H. The goodness of physical model fits shows $R^2 > 0.9$ for the real part of H implying the model represent well the test structural system. On the other hand, the correlation for the imaginary part of H are relatively low indicating the structural damping (C_s) is not of viscous type.

Table D.1. System structural parameters obtained from circular orbit tests under a dry condition (no lubricant). Parameters identified in frequency range 10 – 100 Hz. Orbit amplitude r/c_A=0.05 and static eccentricity e_s/c_A=0.0.

Structural parameter			Direct		Cross-coupled	
			XX	*YY*	*XY*	*YX*
Stiffness	K_s	[MN/m]	12.0	11.9	-0.31	-0.25
Damping	C_s	[kN.s/m]	0.6	0.5	-0.05	-0.02
Mass	M_s	[kg]	3.4	3.7	0.17	0.27
System Mass	M_{BC}	[kg]	15.15			
Natural Frequency	f_n	[Hz]	128	126		
Damping Ratio	ξ_n		0.020	0.018		

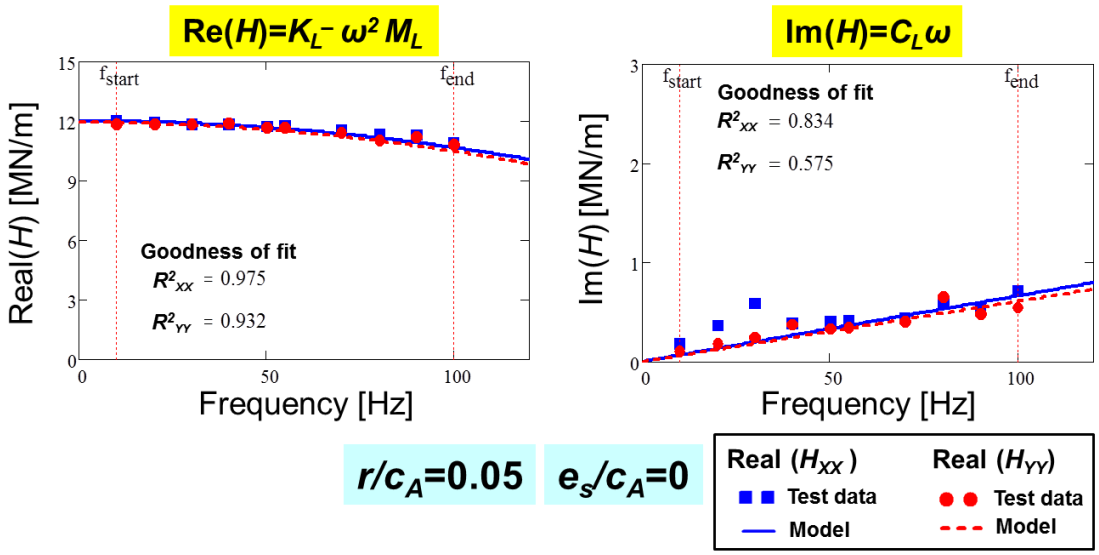

Figure D.1. Real and imaginary parts of direct impedances (*H*) obtained from circular orbit test on a dry (without lubricant) system.

APPENDIX E

UNCERTAINTY OF IDENTIFIED FORCE COEFFICIENTS*

This section outlines the calculation of uncertainty in identified SFD force coefficients. The total uncertainty consists of a bias (instrument) uncertainty, a precision (curve fit) uncertainty and measurement variability. These types of uncertainty are outlined, along with the combination of bias, precision and variability into total uncertainty for each force coefficient $(K, C, M)_{SFD}$. Bias, precision, variability and total uncertainty denoted as B, P, V and U, respectively.

a) Bias uncertainty

The data acquisition (DAQ) board has a rated resolution of B_{DAQ} = 0.1% in the recording of voltage [59]. The DAQ board samples 16,384 samples/second, stores 4096 samples and giving an uncertainty in the output frequency of B_ω = 1Hz for the entire frequency range [59]. This is equivalent to B_ω = 10% at the lowest frequency of 10 Hz, $B_\omega = 1\%$ at the largest frequency of 100 Hz, and an average of $B_\omega = 2.9\%$ across the entire frequency range. Note, the following analysis considers the average B_ω=2.9%, because the force coefficients are best fit over the entire range. Note that actual uncertainty may be less than 2.9% since a Fourier series is used to express the recorded data in the frequency domain.

* Reprinted with permission from "Analysis of Force Coefficients and Dynamic Pressures for Short-Length (L/D=0.2) Open-Ends Squeeze Film Dampers," Den, S., 2015, M.S. Thesis, Texas A&M University, College Station, Copyright 2015 by Sean Den.

The uncertainty of X and Y – REBAM® (displacement) sensors are $B_X = 0.04\%$ and $B_Y = 0.04\%$, respectively. The load cell uncertainty is B_{LOAD} = 0.01%. With these individual uncertainties, the propagation of uncertainty into the measurements of displacement and force, respectively, are

$$B_{DISP} = \sqrt{(B_{REBAM})^2 + (B_{DAQ})^2} = 0.11\% \tag{E.1}$$

$$B_{FORCE} = \sqrt{(B_{LOAD})^2 + (B_{DAQ})^2} = 0.1\% \tag{E.2}$$

Knowledge of frequency domain relations $K \sim F/D$, $C \sim (F/D)\omega$, and $M \sim (F/D)\omega^2$ aids to determine the total bias uncertainty in force coefficients as

$$B_K = \sqrt{(B_{DISP})^2 + (B_{FORCE})^2} = 0.15\% \tag{E.3}$$

$$B_C = \sqrt{(B_{DISP})^2 + (B_{FORCE})^2 + (B_\omega)^2} = 2.9\% \tag{E.4}$$

$$B_M = \sqrt{(B_{DISP})^2 + (B_{FORCE})^2 + (2 \cdot B_\omega)^2} = 5.8\% \tag{E.5}$$

Recall, determination of the SFD force coefficient requires subtraction of dry system coefficients from lubricated system coefficients, i.e.

$$(\mathbf{K}, \mathbf{C}, \mathbf{M})_{\text{SFD}} = (\mathbf{K}, \mathbf{C}, \mathbf{M}) - (\mathbf{K}, \mathbf{C}, \mathbf{M})_{\text{S}} \tag{E.6}$$

Therefore, propagation of the bias uncertainty from two measurements into the SFD coefficient's bias is

$$B_{K_{SFD}} = \sqrt{(B_{K_S})^2 + (B_K)^2} = 0.21\% \tag{E.7}$$

$$B_{C_{SFD}} = \sqrt{(B_{C_S})^2 + (B_C)^2} = 4.1\% \tag{E.8}$$

$$B_{M_{SFD}} = \sqrt{(B_{M_S})^2 + (B_M)^2} = 8.2\% \tag{E.9}$$

b) Bias uncertainty Precision uncertainty

Precision uncertainty deals with the repeatability of measurements. However, only one set of tests were conducted at each test condition (r, e_S). This set of tests consisted of individual tests at several pre-selected frequencies (ω). Plotting the real and imaginary part of the measured impedance versus frequency and using an IVFM curve fit (variation of least squares) gives plots as those shown in Figure E.1. The stiffness coefficient (K) is estimated as the Y-intercept and the mass coefficient (M) are estimated as the curvature of the real part of the measured mechanical impedance. The slope of the imaginary part of the measured mechanical impedance is the estimated damping coefficient (C).

For the estimation of precision uncertainty in a single measurement, Ref. [60] gives

$$P = 1.96 \cdot S \tag{E.10}$$

where S is the estimated standard deviation based upon engineering knowledge. Ref. [61] gives relations for estimated standard deviation of the intercept and slope of a least squares fit line as

$$S_{Intercept} = \sqrt{\frac{1}{N(N-2)}\frac{1-r^2}{r^2}} \tag{E.11}$$

$$S_{Slope} = \sqrt{\frac{1}{(N-2)}\frac{1-r^2}{r^2}} \tag{E.12}$$

where N is the number of points used for the curve fit and r^2 is the curve fit correlation. Using the relations given in Eq. (E.11) and (E.12) with N=10 and r^2=0.95, the propagation into the uncertainty of SFD coefficients gives

$$P_{K_{SFD}} = 1.6\% \tag{E.13}$$

$$P_{C_{SFD}} = 5.3\% \tag{E.14}$$

$$P_{M_{SFD}} = 9.9\% \tag{E.15}$$

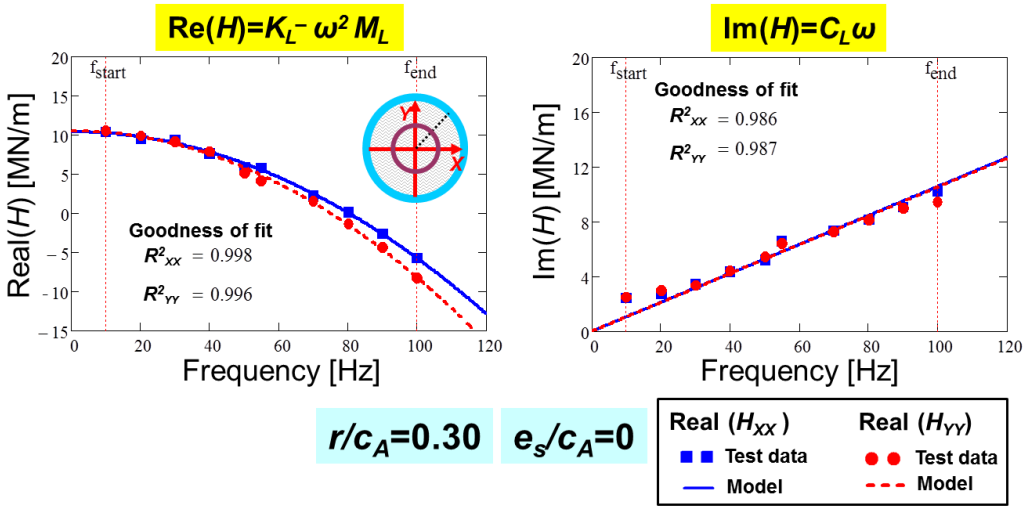

Figure E.1. Plots real (a) and imaginary (b) parts of mechanical impedance versus frequency (ω). Curve fit and measured data shown.

c) Uncertainty due to variability

Uncertainty from variability deals with the repeatability of measurements. In an effort assess the repeatability of the identified *K*, *C*, *M* coefficients, several of the operating conditions included three sets of experiments to calculate the standard deviation of the force coefficient among the three experiments. Note that a weighted average (a function of r/c and e_s/c) of the measured standard deviations delivered those for the operating conditions without three experiments.

The estimation of uncertainty pertaining to the variability of the force coefficients from the averaging of multiple test results is [60]:

$$\varphi_{var} = t \cdot S \tag{E.16}$$

where t is the student's t-distribution value 1.96 corresponding to a 95% confidence interval [60], and S is the precision index of the averaged result and follows given by Ref. [60]:

$$V_{K_{SFD}} = \frac{\varphi_{K\ XX\ SFD}}{K_{XX\ SFD}} = 0.4\% \tag{E.17}$$

$$V_{C_{SFD}} = \frac{\varphi_{C\ XX\ SFD}}{C_{XX\ SFD}} = 3.3\% \tag{E.18}$$

$$V_{M_{SFD}} = \frac{\varphi_{M\ XX\ SFD}}{M_{XX\ SFD}} = 6.1\% \tag{E.19}$$

d) Total uncertainty

The total uncertainty in each SFD force coefficients are

$$U_{K_{SFD}} = \sqrt{(B_{K_{SFD}})^2 + (P_{K_{SFD}})^2} = 2.3\% \tag{E.20}$$

$$U_{C_{SFD}} = \sqrt{(B_{C_{SFD}})^2 + (P_{C_{SFD}})^2} = 9.2\% \tag{E.21}$$

$$U_{M_{SFD}} = \sqrt{(B_{M_{SFD}})^2 + (P_{M_{SFD}})^2} = 17.4\% \tag{E.22}$$

e) Uncertainty of *p*-*p* dynamic pressure

The bias uncertainty of pressure transducers is mainly due to the deviation output of the instrumentation. An uncertainty in the output pressure is ±7 kPa (±1 psi) for the entire operating condition. This is equivalent to B_P = 0.9% at the largest pressure of 8 bar. The temporal fluctuation of the *p*-*p* pressure increases with increase in whirl

frequency (ω) and amplitude motion (r) due to air ingestion and oil cavitation. At high whirl ω=100 Hz, the temporal fluctuation is amount to ~10%. Therefore, propagation of the uncertainty of *p-p* dynamic pressure is

$$U_P = \sqrt{(B_P)^2 + (V_P)^2} = 11.8\% \quad \text{(E.23)}$$

APPENDIX F

TEST SYSTEM RESPONSE DUE TO IMPACT LOADS: COMPARISON BETWEEN TWO OPEN ENDS SFDS

For an open ends test damper with a radial clearance of c_B=267 μm, Ref. [10] reports measurements of system transient response due to a single impact load of increasing magnitude and motions starting at the centered position (e=0). Table F.1 lists the distinct operating conditions for the two test SFDs with identical film land length L=25.4 mm and diameter, as well as lubricant inlet and temperature. However, the damper A has end grooves and chamfered lips that add up to total wetted length L_{tot}=36.83mm (see Fig. 48) where the dynamic pressure generation at the end grooves are significant (see Fig. 27).

Table F.1. Open ends SFD configurations and operating conditions for two film clearances

Parameter	Damper A	Damper B [10]
Radial clearance	254 μm	267 μm
Land length	L_{eff}=2.97*	L=2.54
Static inlet pressure, P_{in}	0.35 bar(g)	0.34 bar(g)
Inlet flow rate, Q_{in}	5.03 LPM	5.21 LPM

*Denotes the effective film land length (L_{eff})

Figure F.1 shows comparisons of the damping ratio (ξ) estimated from both damper A and B differing in clearance and land length. The estimated SFD damping ratio for the small film clearance (c_A) damper is ~1.6 times larger than the damping ratio (ξ) obtained with a larger clearance (c_B) damper. That is, (ξ_B/ξ_A) ~1.6 to ~1.7, which appears to scale with the square of the film clearances, i.e.

$$\frac{\xi_A}{\xi_B} = \left(\frac{c_B}{c_A}\right)^2 \left(\frac{L_{eff}}{L_B}\right)^2 = \left(\frac{0.267}{0.213}\right)^2 \left(\frac{2.97}{2.54}\right)^2 = 1.76 \qquad \text{(F.1)}$$

As detailed in Ref.[5] the simple formulas use an effective film length L_{eff} =1.17 L =29.7 mm that is larger than the design film land length L= 25.4 mm and shorter than the actual wetted length, L_{tot} = 36.8 mm > L_{eff} > L. The effective film land length (L_{eff}) is estimated by curve fitting the recorded pressure profile as a parabolic function of the axial coordinate. Furthermore, Ref. [49] details the comparisons for single frequency dynamic load experimental results with open ends damper A and B.

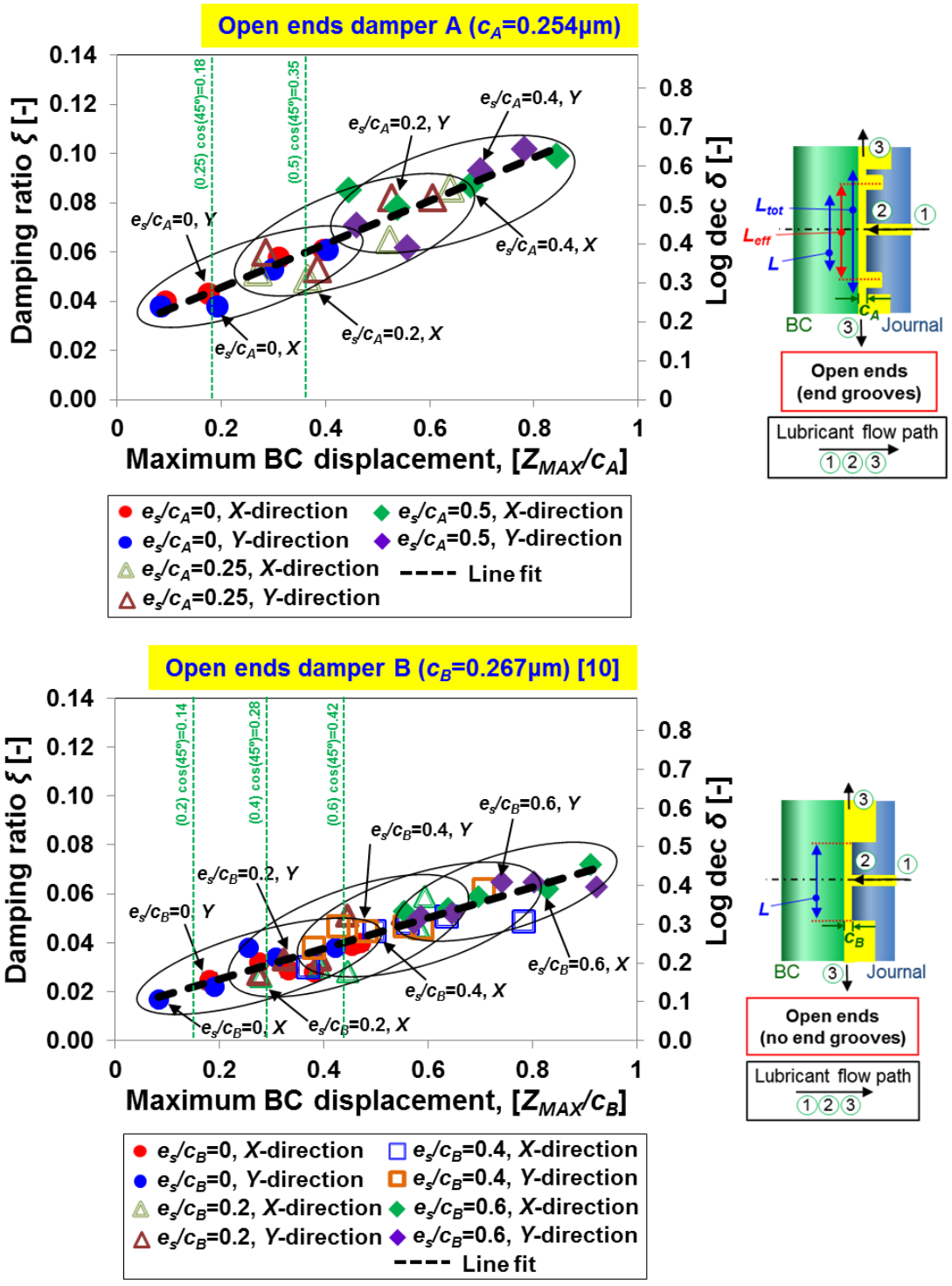

Figure F.1. SFD damping ratio (ξ) versus peak BC (Z_{MAX}/c) displacement. Open-ends SFDs with c_A=0.254 mm and c_B=0.267 mm [10]. Data for one impact load and motions departing from various static eccentricity e_s. Test data for damper B taken from Ref.[10].